

Nanoparticle Imprinted Matrices: Assembling Interfaces with High Selectivity towards Functionalized Nanoparticles

(Nanopartikelär geprägte Matrizen: Aufbau von Grenzflächen mit
hoher Selektivität für funktionalisierte Nanopartikel)

Von der Fakultät für Mathematik und Naturwissenschaften
der Carl von Ossietzky Universität Oldenburg
zur Erlangung des Grades und Titels eines

Doktors der Naturwissenschaften (Dr. rer. nat.)
angenommene Dissertation

von Frau **Julia Witt**, MSc.
geboren am 07. Januar 1984 in Belyje Wody, Kasachstan

Oldenburg, Dezember 2015

Die experimentelle Arbeit für diese Dissertation erfolgte im Zeitraum April 2011 bis Juli 2015 in der Arbeitsgruppe Prof. Dr. Gunther Wittstock, Institut für Chemie, Fakultät für Mathematik und Naturwissenschaften der Universität Oldenburg. Das Kooperationsprojekt mit der Arbeitsgruppe Prof. Dr. Daniel Mandler, Institut für Chemie, Hebrew University of Jerusalem, wurde von der German-Israeli Foundation (GIF) for Scientific Research and Development (research grant no. 1074-49.10/2009) gefördert. Aus dem Projekt resultierten gemeinsame Publikationen, aus denen meine Beiträge in diese Dissertationsschrift einfloßen. Außerdem enthält die Arbeit Resultate einer Kooperaion mit Maria Bosserdts und Prof. Dr. Frieder Scheller, Fraunhofer Institut IZI-BB in Potsdam. Zusätzlich arbeitete ich mit Saustin Dongmo aus der Arbeitsgruppe Wittstock zusammen. Die eigenen Beiträge und die der Kooperations-partner sind in den jeweiligen Abschnitten dieser Arbeit klar ausgewiesen. Während des Promotionsstudiums leitete ich MSc./MEd.-Abschlussarbeiten von Antje-Gabriele Wessel und Anne Staggenborg und BSc.-Abschlussarbeiten von Claudia Kolb und Björn Janßen an. Die im Rahmen dieser Arbeit getesteten Konzepte zu Polyphenol-basierten NIP-Systemen auf Indiumzinnoxid und Glaskohlenstoff wurden bei der weiteren Konzeption der eigenen Arbeiten berücksichtigt.

Gutachter: Prof. Dr. Gunther Wittstock
Zweitgutachter: Prof. Dr. Rüdiger Beckhaus
Tag der Disputation: 26.02.2016

Abstract

This thesis describes the development of nanoparticle (NP) imprinted matrices for investigating the interaction of NPs with interfaces. With the increased use of artificial NPs, there is a need to monitor their occurrence in the environment as well as to estimate the associated effects on biological systems using in vitro systems. It is already known that the toxicity of NPs does not only depend on the elements of the core material but also size and chemical nature of the shell. This calls for a speciation analysis of NPs. To this end, materials were imprinted with different NPs in analogy to the well-known concept of molecular imprinted polymers. The new materials are termed nanoparticle imprinted polymers (NIPs). The removal of the NP template forms complementary cavities capable of selectively recognizing the analyte. While monomer-based matrices were formed by the Langmuir-Blodgett (LB) method, polymeric films were formed by spin coating and by electropolymerization. Citrate protected gold nanoparticles and oleic acid protected iron oxide nanoparticles were used as templates. The dissolution of gold NPs was achieved by a chemical or electrochemical oxidation supported by a chemical complexation. The removal of iron oxide NPs was assisted by magnetic forces or chemical reduction of Fe^{III} followed by complexation. In addition to the measurement of electrolytic currents from NP dissolution, the complete removal of the imprinted NPs was verified by scanning force microscopy, scanning electron microscopy, X-ray photoelectron spectroscopy, polarization modulation infrared reflection adsorption spectroscopy and voltammetry. It was shown that the formation of thin NIPs is a key requirement for efficient detection of NPs after reuptake. These complementary techniques were used to verify each individual step of NIP formation. The concept is discussed and compared to an example of protein imprinted polymers.

Zusammenfassung

Diese Arbeit beschreibt die Entwicklung von Nanopartikel (NP) geprägten Matrizen zur Untersuchung der Wechselwirkung von NP mit Grenzflächen. Mit der zunehmenden Verwendung von künstlichen NP besteht die Notwendigkeit, ihr Vorkommen in der Umwelt zu überwachen, sowie die damit verbundenen Auswirkungen auf biologische Systeme unter Zuhilfenahme von in-vitro Systemen abzuschätzen. Es ist bereits bekannt, dass die Toxizität von NP nicht nur von den Elementen des Kernmaterials, sondern auch von der Größe des NP und chemischer Beschaffenheit der Schale abhängt. Dies erfordert eine Speziationsanalyse von NP. Dazu wurden Materialien mit NP geprägt, in Analogie zu den bekannten Konzepten der molekular geprägten Polymere. Die neuen Materialien werden kollektiv als nanopartikulär geprägte Polymere (NIP, nanoparticle imprinted polymer) bezeichnet. Durch das Entfernen der Templat-NP bilden sich komplementäre Hohlräume, die imstande sind, Analyt-NP selektiv zu erkennen. Während monomerbasierte Matrizen mittels des Langmuir-Blodgett (LB)-Verfahren gebildet wurden, entstanden Polymerfilme durch Schleuderbeschichtung und durch Elektropolymerisation. Citrat-geschützt Goldnanopartikel und Ölsäure-geschützt Eisenoxidnanopartikel kamen als Template zum Einsatz. Die Auflösung von Goldnanopartikeln erfolgte durch eine chemische oder elektrochemische Oxidation unterstützt durch chemischen Komplexierung. Die schonende Entfernung von Eisenoxidnanopartikeln gelang durch magnetische Kräfte oder chemische Reduktion von Fe^{III} gefolgt von einer Komplexierung. Zusätzlich zu der Messung der elektrolytischen Ströme während der Auflösung der NP, konnte die vollständige Entfernung der NP aus den NIPs durch Rasterkraftmikroskopie, Rasterelektronenmikroskopie, Röntgenphotoelektronenspektroskopie und Polarisationsmodulierten Infrarotreflexionsabsorptionsspektroskopie verifiziert werden. Diese komplementären Techniken fanden Verwendung, um jeden einzelnen Schritt der NIP-Bildung zu überprüfen. Das Konzept wird im Vergleich zu einem Beispiel mit Protein-geprägten Polymeren diskutiert.

Danksagung

Mein besonderer Dank gilt Herrn Prof. Dr. Gunther Wittstock für die Überlassung des Themas und die Betreuung der Arbeit. Mit seiner fortwährenden Bereitschaft Forschungsergebnisse ausführlich und kritisch zu diskutieren sowie seinen wertvollen Ratschlägen und Anmerkungen hat er zum erfolgreichen Gelingen der Arbeit beigetragen und mich immer motiviert.

Des Weiteren danke ich Herrn Dr. Rüdiger Beckhaus für die freundliche Übernahme des Zweitgutachtens.

Für die finanzielle Unterstützung dieser Arbeit möchte ich mich bei der German-Israeli Foundation (GIF) for Scientific Research and Development bedanken.

Bei Herrn Prof. Dr. Daniel Mandler von der Hebrew University in Jerusalem (Israel) möchte ich mich für die gute Zusammenarbeit, den reichhaltigen Austausch von Erfahrungen und neuen Ideen zu weiterführenden Versuchen bedanken.

Spezieller Dank geht an Frau Prof. Dr. Monika Fritz von der Universität Bremen, die mir zu Anfang meiner Promotion ein besseres Verständnis beim Umgang mit dem Rasterkraftmikroskop vermitteln hat und mit wertvollen Hinweisen und Anregungen zu einer erfolgreichen Durchführung der mikroskopischen Untersuchungen beigetragen hat.

Meinen herzlichen Dank für das freundschaftliche Arbeitsklima und die vielseitigen Hilfestellungen möchte ich allen ehemaligen und aktuellen Mitarbeitern des Arbeitskreises Wittstock aussprechen. Ich danke Herrn Dr. habil. Carsten Dosche für die Einweisung in die Bedienung des XPS Spektrometers und die Hilfe bei der Interpretation der Spektren. Frau Dr. habil. Izabella Brand danke ich für die Unterstützung bei den Durchführungen der PM IRRAS Messungen. Ich danke Herrn Frank Meiners für die Unterstützung am AFM und viele ideenbringende Diskussionen. Herrn Saustin Dongmo danke ich für die anregende Zusammenarbeit im Labor und seine außerordentliche Hilfsbereitschaft. Für den Einsatz und Interesse an meiner Arbeit möchte ich mich bei meinen Bachelorstudenten Herrn Björn Janßen und Frau Claudia Kolb und meinen Masterstudenten Frau Anne Staggenborg und Frau Antje-Gabriele Wessel bedanken. Zudem danke ich Herrn Gerd Gertjegerdes für die technischen Hilfestellungen und Herrn

Patrick Mösgen für die Hilfe bei präparativen Aufgaben im Labor. Des Weiteren gilt mein Dank Frau Heike Hillmer, an die ich mich immer bei administrativen Fragestellungen wenden konnte.

Außerdem bedanke ich mich bei meinen Eltern Lilia und Willi und meinem Bruder Alexander, die mir in vielen Bereichen ein positives Vorbild waren und meine Arbeit mit großer Anteilnahme verfolgt haben.

Abschließend möchte ich mich bei meinen Freunden Rebecca, Patrick, Eva, Daniel, Florian und Ben bedanken, die mich in den richtigen Momenten aufbauten und für die erforderliche Abwechslung sorgten. Vor allem danke ich Luis für seine uneingeschränkte und liebevolle Unterstützung während des Schreibens meiner Doktorarbeit.

Table of Contents

1.	Introduction	1
2.	Applied characterization techniques for supported nanomaterials.....	5
2.1	Material-dependent working modes of scanning force microscopy	5
2.1.1	Operation principles and probe requirements	6
2.1.2	Operation modes	11
2.2	Material-dependent working modes of scanning electron microscopy	18
2.3	Electrochemistry of metal nanoparticles and complex formation	21
3.	Assembly of nanoobjects in rigid matrices	25
3.1	Assembling two-dimensional NP arrays	25
3.1.1	Electrostatic attachment	26
3.1.2	Langmuir-Blodgett with nanoobjects	26
3.2	Specific and non-specific interaction of nanoobjects with surfaces	27
3.3	Molecular imprinting	28
3.3.1	Preparation and application of MIPs.....	28
3.3.2	Surface imprinting	30
3.4	Nanoparticle imprinted matrices.....	32
4.	Experimental details	35
4.1	Chemicals	35
4.2	Instrumentation used for preparation and characterization of samples	36
4.3	General cleaning procedure	41
4.4	Preparation of gold surfaces	41
4.5	Preparation of template stripped gold surfaces.....	41
4.6	Immobilization of nanoparticles	42
4.6.1	Langmuir-Blodgett assembly of iron oxide NPs on TSG substrates	42
4.6.2	Attachment of gold NPs to APTES-functionalized ITO substrates.....	44
4.7	Formation of thin matrices by electropolymerization of phenol	45

4.8	Preparation of thin iron oxide NP imprinted PDMS composites.....	46
4.9	Nanoparticle removal.....	47
4.9.1	Electrochemical removal of gold and silver NPs.....	47
4.9.2	Chemical removal of gold NPs	48
4.9.3	Chemical removal of iron oxide NPs.....	48
4.9.4	Magnetical removal of iron oxide NPs	48
4.10	Reuptake experiments.....	49
4.11	Permeability test	49
5.	One step deposition of composites of polymer matrix and nanoobjects.....	50
5.1	Deposition and selective dissolution of protein-polymer composites	50
5.2	Spin coating of composites of iron oxide NPs and PDMS	54
5.3	System with iron oxide nanoparticles and oleic acid.....	66
5.4	System with gold NPs and poly(aniline)	72
6.	NIP system realized by sequential deposition of matrix and nanoobjects....	77
6.1	Immobilization of template gold NP on APTES-modified ITO samples	78
6.2	Electropolymerization of conformal films.....	85
6.3	Polyphenol-based NIP systems.....	89
7.	Summary.....	119
7.1	Investigated systems and conclusion	119
7.2	Conclusion and outlook	121
8.	Appendix.....	125
8.1	Abbreviation	132
8.2	Symbols	133
9.	References.....	137
10.	Own publications and conference contributions.....	147
10.1	Publications.....	147

10.2	Oral presentations in national and international conferences	147
10.3	Posters in national and international conferences.....	148
11.	Curriculum vitae.....	149

1. Introduction

Nanoparticles are defined by the National Nanoscience Initiative as particles having at least one dimension between 1-100 nm.^[1] Nanoparticles (NPs) and more general nanoobjects have caught the imagination of scientist and engineers due to the fascinating properties of these materials. Although the core of NPs can be described as a very small crystal, the properties may be very different from macroscopic solids of the same crystal structure. For instance, surface-volume ratio,^[2] band gaps,^[3] plasmonic properties^[4] are quite different from macroscopic counterparts, which enables new applications. Small metal particles have found widespread use in heterogeneous catalysis for several decades. However, many new applications in light conversion,^[5] medical health care products,^[6] ferro fluids,^[7] analytical chemistry^[8] or medical diagnostics^[9] have only been enabled by tremendous progress in synthesis methods yielding NPs of small size dispersion,^[10, 11] shape-control^[12, 13] or efficient stabilization by a ligand shell or even by complex core-shell architecture^[14, 15].

Nowadays, already now NPs are used in more than 1800 consumer products. The largest product category comprises health care and fitness products followed by home/garden, food and beverage, automotive and electronics/computers areas.^[16] The widespread use ultimately also leads to a release of NP into the ecosphere. This consequence calls for a detailed consideration of their specific toxicological effects and monitoring of their release. This research direction has recently been termed ‘nanotoxicology’.^[17, 18] The potential toxicity of NPs can be expected to be different from macroscopic solids and from dissolved ions of the constituting elements. The difference in toxicity between the elemental state of metals and different ions of the same metal is well known from classical toxicology (e.g. Cr⁽⁰⁾, Cr³⁺, CrO₄⁻) and speciation analysis^[19, 20] is typically carried out in environmental samples. For NPs the situation is even more complex. Even when neglecting specific actions of biomacromolecules and other submicrometer-sized biological objects that could be regarded as organic NPs, NPs may contain a wide range of materials such as metals, elemental and compound semiconductors or polymers.^[21, 22] Specific toxicological effects of NPs are often associated with their ability to cross biological cell membranes, a situation not found in macroscopic solids. However, not only the uptake may be different from macroscopic

materials, also the chemical action may be different. One example is the toxicity of silver NPs (AgNPs). Compton and co-workers^[23] ascribe their enhanced toxicological potential against bacteria to the changed mechanism of oxygen reduction. Silver electrodes develop a mixed potential in ambient biological fluids controlled by silver dissolution, silver deposition and irreversible oxygen reduction. During oxygen reduction reactive oxygen species (e.g. H₂O₂) are formed. At macroscopic Ag surfaces they quickly enter follow-up reactions to water. The efficient mass transport at the NP makes it however unlikely that a soluble intermediate will react again at the same surface and therefore the release of reactive species will be enhanced compared to macroscopic silver.

The toxicological properties of NPs and their prospective widespread use (associated with corresponding regulative procedures^[24, 25]) require facile tools to determine in vitro the concentration of NPs and further toxicologically important properties of them like core material, size and chemical nature of the shell. One attractive approach followed in this thesis is nanoparticle imprinted polymers (NIPs) that are analogous to the concept of the well-known molecularly imprinted polymers (MIPs).^[26-28] Briefly, MIPs are obtained by performing a polymerization in the presence of a template molecule that will be embedded in the polymer in a way that allows a subsequent removal. After the removal, cavities or binding sites are formed in the polymer that can reversibly reuptake the same molecule. Specific cavities in NIPs or MIPs are denoted in this thesis as {}. For instance, {} stands for an empty cavity and {AuNP} stands for a binding site occupied by a gold nanoparticle. When this work was started, only one example of NIP had been described by Koenig and Checkig.^[29] They produced a bulk NP-polymer composite from which the NP had been dissolved. Due to the size of the NP, a reuptake was not possible. This thesis therefore focuses on formation and characterization of *thin* NIP films that typically only partially enclose a monolayer of NPs. Such film architecture seems also very suitable for electrochemical detection schemes that also require an electronic contact of the NP within the film to a conducting support. As mechanisms of NIP formation, NP detection within NIP, NP reuptake in NIP are unknown, the research work in this thesis sets a specific focus on characterizing NP in NIP systems by a combination of microscopic, electrochemical and spectroscopic techniques. With the help of those techniques, several NIP systems have been developed, evaluated and improved in an iterative manner.

This thesis provides first an overview about the used microscopic techniques and their applicability towards NIP systems (Chapter 1). Chapter 1 summarizes the existing NIP systems from which some have emerged after the first demonstration of the thin film NIP concept in which this author participated. Chapter 1 contains the experimental details. Chapter 5 describes the developed NIP systems in which template NPs and matrix are deposited in one step, while Chapter 6 contains those experiments in which the matrix is assembled around preadsorbed NPs on surfaces. The thesis is concluded by a summary and outlook in Chapter 1.

2. Applied characterization techniques for supported nanomaterials

Direct imaging of nanomaterials cannot be done by optical inspection due to the low spatial resolution of optical methods. This chapter covers commonly used high-resolution techniques to characterize nanostructured materials. This includes surface sensitive methods, such as scanning force microscopy (SFM) in Chapter 2.1 and scanning electron microscopy (SEM) in Chapter 2.2. Furthermore, selected approaches for the electrochemical detection of metal NPs are summarized in Chapter 2.3.

2.1 Material-dependent working modes of scanning force microscopy

The scanning force microscopy (SFM), also called atomic force microscopy (AFM), is the most common technique of scanning probe microscopies (SPM). It was invented by Binnig et al.^[30] in 1986 following the development of scanning tunneling microscopy (STM).^[31] STM provides atomic-resolution images of conductive surfaces, while an extremely fine (single atom) conducting probe is held about a few atomic diameters from the sample surface.^[32] When a small voltage is applied during scanning, a tunneling current flows which strongly depends on the distance between the tip of the probe and the surface. By keeping either the height of the tip or the tunneling current constant, a three-dimensional image of the surface can be generated providing valuable information on the electronic properties of the material. The STM has found broad applicability in the fields of physics,^[33, 34] chemistry^[35, 36] and materials science.^[37-39] However, one limitation is that STM can only be used for imaging conductive materials. SFM extended the microscopic capabilities to insulating materials.^[40, 41] The measuring principle is based on force interactions between the surface and the tip at a very close distance. These forces range from pN to μN .^[40, 42] Due to instrumental developments and further adaptations of the tip, the scanning force microscope can be operated in a range of environments (ultra-high vacuum [UHV], air, liquids). Various new modes allow distinguishing between mechanical surface properties such as friction,^[43] stiffness and adhesion^[44] as well as electrostatic,^[45] steric^[46] and magnetic^[47] forces. Chapter 2.1.2 covers all operation modes

relevant to this work. Apart from simple topographic imaging and measurement of surface properties, this technique is routinely used to determine the thickness of thin films which are relatively deformable compared to the underlying substrate.^[48-52] In this procedure, known from the SFM-based nanoshaving lithography,^[53-55] the probe is scanned several times across a small selected region of the film, with a higher mechanical force applied to the SFM tip. Under these conditions, the tip penetrates and abrades the soft material until the bare area of the substrate is exposed. Afterwards the height difference between scratched part and the intact film area is used for thickness determination. A detailed description of SFM thickness measurements is given in the Chapter 4.2. Over two decades, SFM became a standard microscopic technique utilized to obtain topographical images and other information from a wide variety of materials including solid samples^[56, 57] as well as soft and delicate ones like biomolecules^[58, 59] and polymers.^[60, 61] It is possible to yield topography images with a resolution of approximately 0.001 nm in the vertical and 0.2 nm in the lateral direction.^[40] A more detailed general description of SFM techniques can be found in Ref.^[40].

2.1.1 Operation principles and probe requirements

SFM means scanning across the sample surface in a raster pattern with a very sharp tip attached to a flexible cantilever, carefully maintaining a close distance between the probe and the sample at a set value using a feedback control system (Fig. 1). Changes in the deflection of the cantilever caused by topographical surface features and tip-sample interactions, are measured by a laser beam which is reflected off the back of the cantilever slightly behind the tip. The beam position is received by a position sensitive photodetector.^[40] Usually, the detector is split into four segments labeled A, B, C, D and is capable of sensing the vertical and lateral (torsional) cantilever deflection simultaneously and separately. The height feedback signal from the photodetector is taken to be proportional to the sample topography and gives the distance the scanner had to move vertically to achieve the pre-set setpoint. In a conventional large-sample scanning force microscope, the cantilever is mounted to a piezoceramic tube scanner, which is used for high-precision movements of the probe in the x - y plane and the vertical direction (z) by expanding or retracting proportionally to an applied voltage.^[62] Small-

sample instruments operate with a stationary probe and a scanning sample mounted onto a three-dimensional piezo scanner. It allows very high resolution, low noise measurements, but limits the range of modes accessible for imaging and inherently requires samples of small size and weight.^[63]

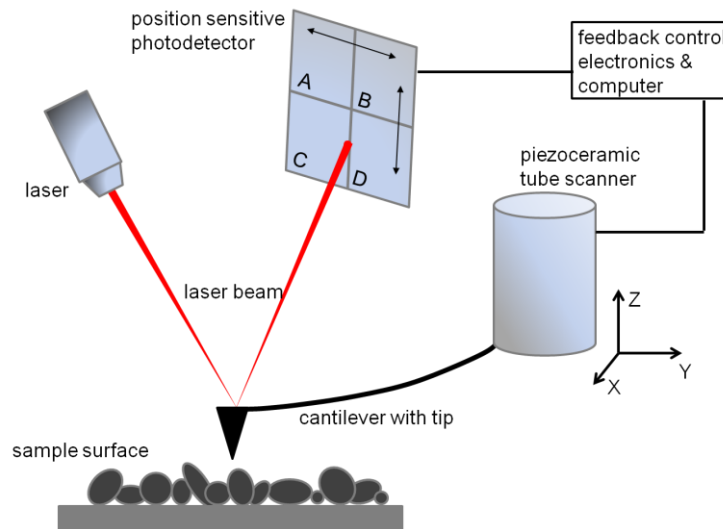


Figure 1. Schematic setup of a scanning force microscope with scanning cantilever probe and beam deflection detection system. Tip position in x , y and z direction is controlled by the piezoelectric tube scanner.

A wide variety of forces can be detected as the tip approaches the sample. However, when operating in air in the absence of external fields, the main normal forces contributing to cantilever deflection are attractive long-range (van der Waals) and repulsive short-range (electrostatic Coulomb) forces.^[64] Induced by fluctuating dipole moments among atoms of the tip and the specimen, these forces can be approximated by the Lennard-Jones potential as the function of the probe-sample distance, and be associated with the operating SFM modes (Fig. 2). Two basic modes can be applied, the static (contact mode) and the dynamic mode (intermittent mode and non-contact mode). Contact mode operations are restricted to the repulsive force regimes, where the force gradient is high. In the intermittent mode, also known as Tapping ModeTM, an oscillating cantilever remains in both the attractive and the repulsive part of the curve, while the non-contact mode applies to the attractive part only. Furthermore, operating at a higher atmospheric humidity causes a thin layer of water vapor to be adsorbed on the sample surface which is accompanied by strong adhesion forces due to the capillary effect.^[40, 65]

This problem can be easily eliminated by conducting experiments in an aqueous medium or under ultrahigh vacuum conditions. Weisenhorn et al.^[66] showed that the force applied to the surface by the tip can be reduced by a factor of 10-100 while measuring in water instead of air.

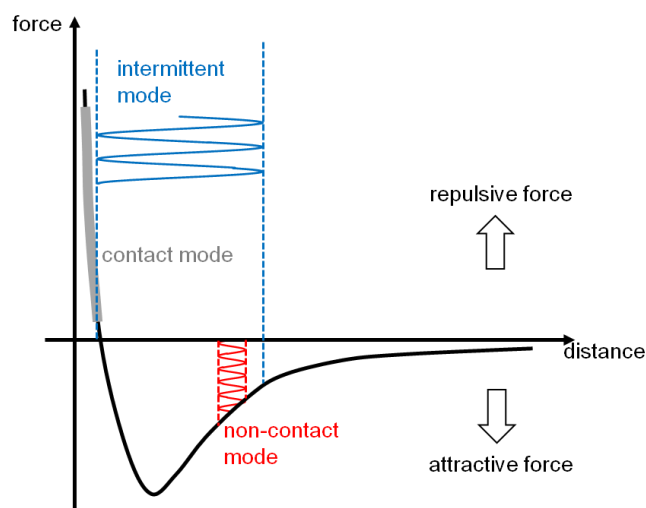


Figure 2. Schematic illustration of the Lennard-Jones potential shows the interatomic forces between the tip and the sample in dependence of their distance. Three SFM operating modes are differentiated by implied interaction forces: the contact mode, the intermittent mode and the non-contact mode.

The resolution of SFM depends on many factors, e.g. the nature of the sample surface to be studied; the sensitivities of the optical lever, which measures the local height of the probe; the piezo scanner, which regulates the height combined with a careful control of probe-sample forces; and particularly the geometry and mechanical requirements of the tip and the cantilever. Commercially available SFM cantilevers are typically fabricated from silicon or silicon nitride with an integrated sharp tip (radii range from 10 nm for etched Si tips to 20-60 nm for standard Si_3N_4 tips) and usually appear pyramidal, tetrahedral or conical in shape.^[40, 67] In general, the smaller the tip radius, the smaller the structures that can be resolved. Broadening of features is one of the well-known convolution effects and occurs when the tip curvature radius is comparable or greater than the structure size. This is illustrated in Fig. 3. The SFM topography image shows well dispersed iron oxide NPs (~ 10 nm, Fig. 3a) with an average distance of 100 nm on the surface of a template stripped gold (TSG) sample after a LB transfer. The

original oleic acid stabilizing ligand shell of the NPs was partially replaced by 1-mercaptoundecanoic acid. Changing NP properties led to a covalent interaction between particle and Au surface by the presence of a thiol terminated ligand shell. These measurements were prepared within the project regarding the formation of two dimensional nanocomposites (Chapter 5.3), but not further traced as the ligand exchange reactions were difficult to reproduce and to characterize. Based on the cross section obtained from SFM images (Fig. 3a), the broadening effect can be clearly seen as the particles have a larger lateral dimension as expected. When the same particles are scanned by a tip with a smaller radius than that used for experiments, the SFM images would show particles having a smaller lateral dimension (Fig. 3b). The lateral dimension of the particles obtained from SFM images cannot be used to characterize their size due to tip convolution, but the height can be.

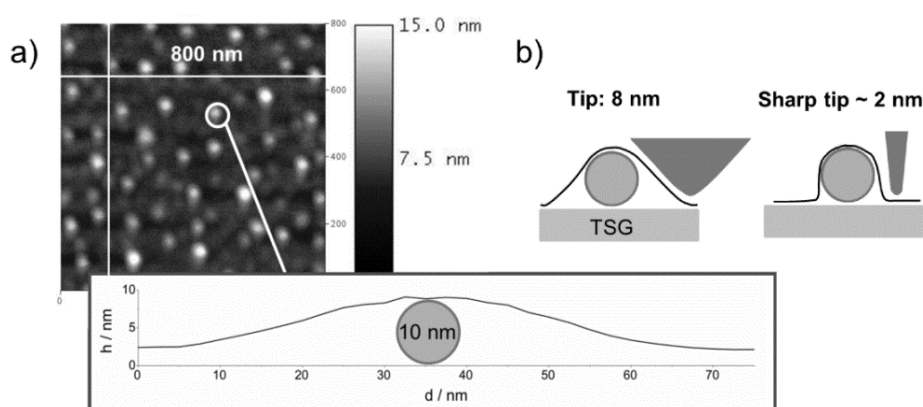


Figure 3. a) SFM topography image recorded in the intermittent mode and the corresponding cross section of marked NP (approximately 10 nm in diameter) indicating the convolution effect. b) The schematic cross section represents the path of the tip as it scans over the sample, while the finite size of the imaging tip may cause raised features such as the NPs to be broadened.

To overcome the limitation of silicon tips and to minimize convolution effects during the observation of small features, carbon nanotube (CNT) tips have been successfully used. Carbon nanotubes acting as SFM probes provide a new class of high performance sensing systems, achieving molecular resolution due to their high aspect ratio and reversible buckle ability.^[68-70] In form of flex single-walled nanotubes (SWCNT, 1-3 nm in diameter) and multi-walled nanotubes (MWCNT, 5-100 nm in diameter), they are either attached or directly grown on standard microfabricated SFM

tips and may have several micrometers of length.^[71, 72] As a reference to minimize tip convolution, Martinez et al.^[73] used the carbon nanotube technology to image biomolecules such as DNA. The conventional cantilever shape for intermittent mode is a rectangular bar, whereas triangular (V-shaped) cantilevers are often used in the contact mode. They are available with different coatings (i.e. gold or aluminium) either on the back side, in order to increase the reflectivity for the optical detection or completely covered, e.g. with a conductive material, allowing the probe to act as an electrode.

When choosing the cantilever different criteria should be met depending on the application it is used for. According to Hook's law:

$$\Delta z = \frac{\Delta F}{k} \quad (1)$$

where Δz , the deflection of the cantilever, is determined by the acting force ΔF and the spring constant k . If a cantilever with a low spring constant is used, maximum force sensitivity can be achieved. The spring constant (typically ranging between 0.001 to 100 N m⁻¹^[74]) is related to the stiffness of the cantilever, which is described for a rectangular cantilever by its thickness d , average width w , length l and the Young's modulus Y (coefficient of elasticity):^[75]

$$k = \frac{Yd^3w}{4l^3} \quad (2)$$

Another important property of the cantilever is the resonant frequency f_0 , which is strongly influenced by the spring constant and the effective mass m of the lever as follows:

$$f_0 = \sqrt{\frac{k}{m}} \quad (3)$$

High frequency cantilevers minimize the sensitivity to external vibrations of the instrument and allow scanning at a higher speed.^[76-78] While maintaining a low spring constant, which characterizes a soft cantilever, the mass needs to be quite low to keep the k/m ratio large. Due to a significantly reduced tip-sample interaction, soft cantilevers are ideally suited to investigate soft fragile samples nondestructively in contact mode. Larger, relatively thick cantilevers with a high spring constant are recommended for dynamic

SFM modes since they are sufficiently rigid to prevent an oscillating tip to get pulled into the sample, which can easily happen with soft cantilevers.^[76, 79] The technical data of cantilevers used in this thesis are listed in Table 1 to give a comparison for typical contact mode and intermittent mode requirements.

Table 1. Specification of soft and rigid cantilever and tip used in this thesis for SFM measurements in contact mode or intermittent mode.

Cantilever specification	Contact mode (soft)	Intermittent mode (rigid)
shape:	triangular	rectangular
back side coating:	reflective gold	reflective aluminium
resonant frequency [kHz]:	90-160	230-410
spring constant [N m^{-1}]:	0.3-1.2	20-80
length [μm]:	80-90	110-140
width [μm]:	13-23	30-50
thickness [μm]:	0.5-0.6	3.25-4.75
Tip specification		
height [μm]:	2.5-8.0	10-15
radius [nm]:	10-40	10

2.1.2 Operation modes

Static mode. The static mode, also called contact mode, operates either in the constant height mode, where the z -height remains constant and the deflection of the cantilever in z -direction provides the image contrast during the x - y scanning (Fig. 4b), or in the more commonly used constant force mode, where the force between tip and sample is kept constant by a feedback system and the topography is created from the height needed by the cantilever to be displaced in order to regain the initial z -deflection of the cantilever (Fig. 4a). Both modes allow high resolution imaging as the tip scans in a very close distance (a few Ångstrom) to the sample, thus being affected by strong repulsive forces. The constant height mode works with a high scanning speed since the scanner does not have to move up and down. However, high resolutions can only be achieved on relatively flat and smooth surfaces. Rough surfaces with extreme changes in the vertical topography provide a higher probability of tip-sample collisions and can be probed more easily in the constant force mode. This mode operates with a lower scan speed to keep the feedback

signal and gives a good control on the tip position. By using cantilevers of a low spring constant, the strong forces between tip and sample can be better balanced, which is substantial to avoid sample damages in constant force applications on soft matter. Under these premises, Leit et. al.^[80] investigated the morphology of conductive polymers in different adsorption stages and interpreted the observations by different parameters such as roughness, relative surface coverage and fractal dimension.

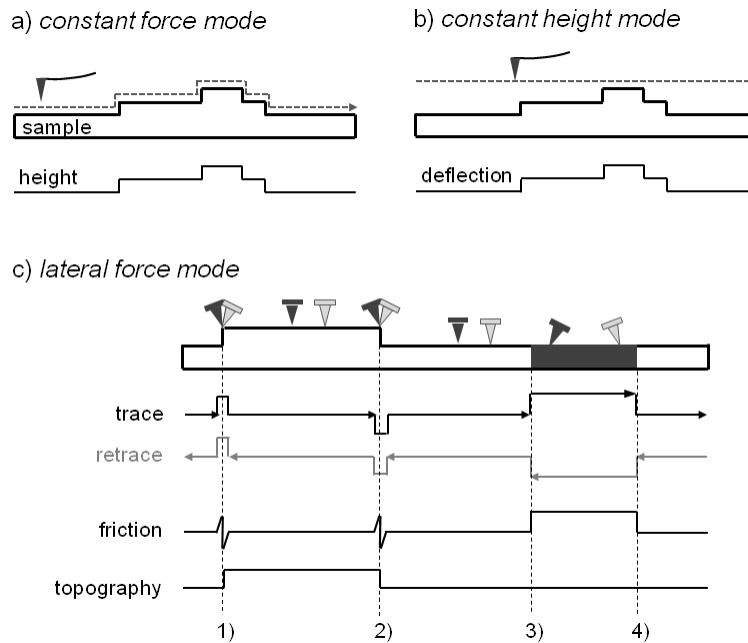


Figure 4. Schematic representation of a) the constant force mode, b) constant height mode and c) lateral force mode: In the lateral force mode the friction loop is measured by tracking the lateral deflection signal in two opposite directions (trace and retrace). Most topographic components are removed by subtracting the data for trace and retrace (1 and 2). The black part in the sample indicates a domain with a relatively large friction (3 and 4). Signals originating from vertical deflections (1 and 2) are reflected in the topography trace.

One challenging issue of the constant force mode is the lateral friction force between tip and sample, which can be considered as the force that resists the relative lateral motions between two contacting bodies. Friction forces increase proportional to the total tip load exerted on the sample, and cause the cantilever to bend sideways. This effect may damage weakly bound molecules or blunt the tip during scanning, resulting in a lower spatial resolution. In order to quantify and map frictional forces the lateral force microscopy (LFM) is used. In the lateral force mode, the tip scans back and forth, in most cases perpendicular to the long axis of the cantilever causing a torsional motion of the

cantilever along the same axis with respect to the horizontal plane (Fig. 4c). In addition to the normal forces detected by the vertical bending of the cantilever, the lateral force can be calculated from the twisting angle of the cantilever using known parameters (e.g. dimensions, stiffness). Generally, the higher the torsional stiffness of the cantilever, the greater the sensitivity of lateral forces. Changes in local friction originate from a number of physical phenomena, such as electrostatic interaction, surface elasticity and chemical interaction or capillary forces, but may also be influenced by the topography (surface roughness, slope variations of surface features). LFM provides quantitative data on interfacial interactions and material-sensitive contrasts due to variations in surface composition,^[81, 82] molecular organization^[83, 84] or mechanical properties.^[85, 86]

Dynamic mode. The dynamic mode, including for example the intermittent mode and the non-contact mode, can be employed to overcome high lateral forces between the SFM tip and the sample surface. Different to the static mode, the tip is only intermittently touching the sample surface. Thus, intermittent mode prevents the tip from being trapped by adhesive forces and causing damage to soft matter during scanning.^[87] It is also useful in the study of weakly attached deposits on substrate surfaces. This phenomenon was experienced, when trying to image AuNPs which were electrostatically attached to an 1-aminopropyltriethoxysilane (APTES)-modified indium tin oxide (ITO) surface by SFM (Chapter 6.1). Contact-mode imaging turned out to be not useful since the particles were easily displaced due to the strong lateral forces between the tip and the sample. Figure 5 show images acquired in the intermittent mode and in the contact mode. After a few scans in the contact mode the amount of particles in the scanned area (Fig. 5a, b) is clearly lower than in the area outside the scanning window (larger scan area Fig. 5c). In contrast, intermittent mode permits imaging of AuNPs with a well-defined outline (Fig. 5d).

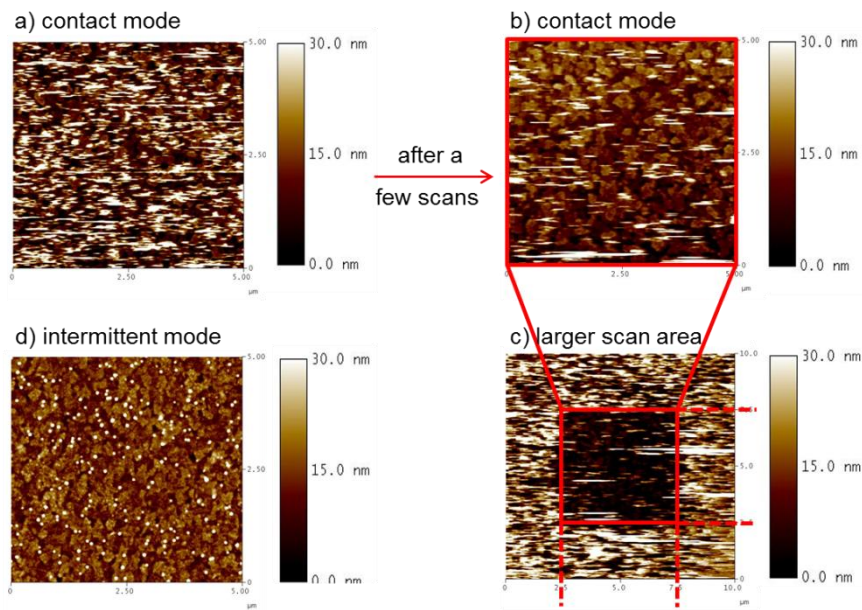


Figure 5. SFM images of AuNPs electrostatically attached to APTES-modified ITO samples recorded in the a), b) contact mode and d) intermittent mode of a scan area of $5\ \mu\text{m} \times 5\ \mu\text{m}$. c) Imaging in the contact mode causes a displacement of AuNPs after a few scans (clearly indicated by the image with a larger scan area of $10\ \mu\text{m} \times 10\ \mu\text{m}$).

In intermittent mode the cantilever is excited to oscillate close to its resonant frequency with a free amplitude ranging between 5 and 100 nm in air (Fig. 6a).^[88] Compared to the free cantilever oscillation, the oscillation amplitude is necessarily reduced by several tens of nm due to the energy loss when the tip is in contact with the surface (Fig. 6b).^[40] The reduction in oscillation amplitude is used to identify and measure the topography. During scanning, the cantilever oscillation amplitude is maintained as close as possible to the pre-defined amplitude setpoint by adjusting the probe to sample distance accordingly (feedback loop, Fig. 6c, d). Furthermore, the phase shift of the oscillating cantilever relative to the driving signal as reference allows mapping material characteristics of a heterogeneous sample surface (Fig. 6e). The phase signal can be influenced for example by variations in composition, hardness, adhesion, friction, viscoelasticity, electrical and magnetical properties of the studied sample.^[89] Typical response curves of a cantilever are shown in Fig. 6.

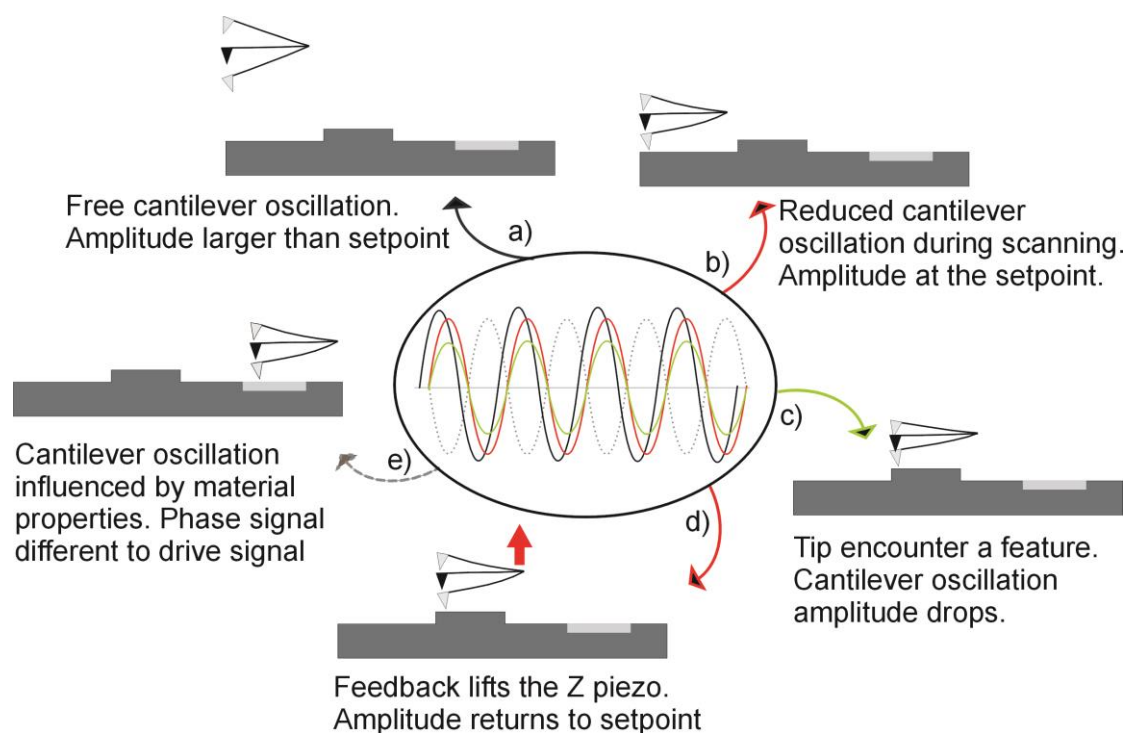


Figure 6. Scheme illustrates the principles of intermittent mode and phase imaging.

The non-contact mode relies on a similar principle like the intermittent contact mode. It is characterized by small probe oscillations with an amplitude of usually 1 nm, while the tip is lifted 50-100 Å above the surface. This mode operates in the attractive regime of the intermolecular force curve in Fig. 2.^[40] The large distance and weak attractive forces between tip and sample may lead to a poorer resolution than obtained with contact and intermittent contact modes. However, several studies^[90-92] raise hopes that the non-contact mode may obtain true atomic resolution images under a number of environmental conditions.

Force spectroscopy. Force spectroscopy using a scanning force microscope, in both the static or dynamic modes, is a powerful tool to obtain a deep insight in the properties of the sample surfaces besides the topography as it allows the quantification of forces on the nN scale. Monitoring interaction forces is realized by the measurement of force-distance curves (Fig. 7). Force-distance curves show the cantilever deflection u as a function of the height z during tip approach (trace, Fig. 7 dashed black curve) and retraction (retrace, Fig. 7 solid grey curve). By using Hook's law [Eq. (1)], the tip-sample force can be calculated

from the deflection for each vertical displacement distance z . The static SFM configuration is used as the standard approach to obtain force-distance curves. When the tip is far away from the sample surface, no interaction can be measured (Fig. 7, point 1). As the tip is at an interatomic distance, it snaps into contact with the surface due to attractive van der Waals forces (Fig. 7, point 2). This results in a small downward deflection. The adhesion is also often caused by capillary forces, which may appear when imaging under ambient conditions, i.e. in the presence of an adsorbed water layer or organic contaminants on the sample surface.^[93] During a further approach, repulsive forces bend the tip away from the sample causing the deflection signal to increase proportionally to the force acting on the cantilever [according to Hooke's law in Eq. (1)] until the setpoint of deflection is reached (Fig. 7, point 3).

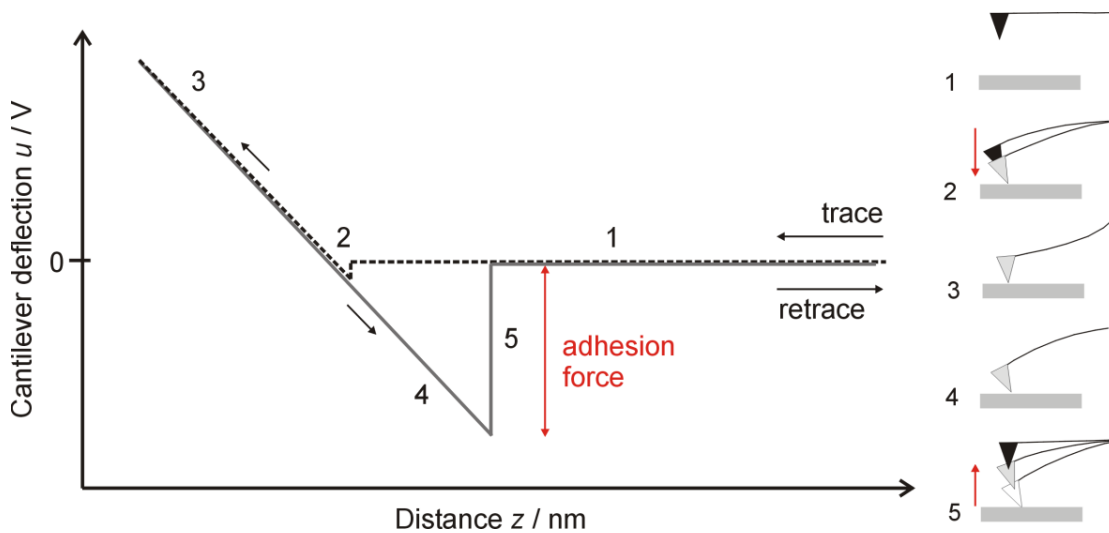


Figure 7. A force-distance curve represents the approach (dashed, black curve) and the retraction (solid, grey curve) part. No interaction can be measured when the tip is far away from the sample (1). Point 2 describes the jump into contact of the SFM tip to the sample. After that, the tip-sample separation decreases, causing a deflection of the cantilever (3). Due to adhesion forces, the tip remains in contact during retraction and the deflection signal decreases (4). In point 5, the tip loses the contact to the surface upon overcoming of the adhesive forces.

When the tip is retracted beyond the contact point, it remains attracted to the surface by adhesion causing the cantilever to bend towards the sample (Fig. 7, point 4), until the loss of contact (snap-off) where no deflection signal is measured (Fig. 7, point 5). The finite force necessary to pull the tip off the sample surface is often used to quantify adhesion forces. Dissipative processes and interfacial interaction (e.g. adhesion

force) in the contact of the tip and the sample cause the hysteresis between the approach and the retraction.^[93, 94] This hysteretic effect can be eliminated using stiffer cantilevers.^[93, 95] However, the use of dynamic SFM has become an interesting subject to obtain quantitative information on material properties. This was supported by numerical simulations as well as experimental data.^[96-98]

In a more sophisticated version of this technique, called single-molecule force spectroscopy (SMFS), only one interacting molecule is attached with one end to a surface and with its free end to the probe. Mechanical stretching of this molecule by a piezoelectric controller produces restoring forces as function of extension. This offers a unique opportunity to detect binding forces of macromolecules to various surfaces^[99-101] as well as protein folding and unfolding processes^[102-104] via high-resolution force-extension curve measurements. Typical approach (grey curve) and retraction (black curves) traces for mechanical stretching of a protein are shown in Fig 8.

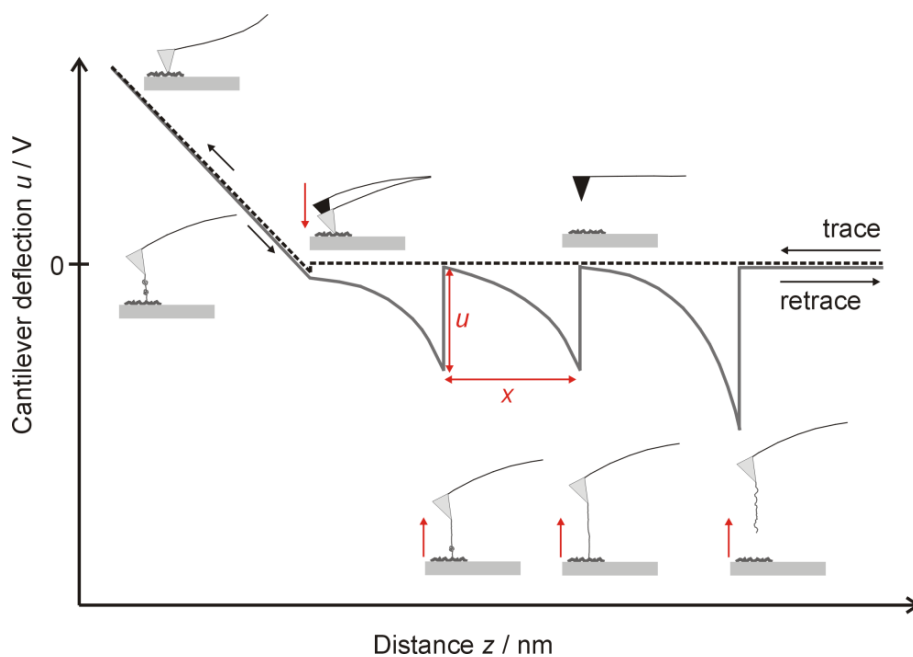


Figure 8. A typical force-extension curve represents the protein folding and unfolding process during mechanical stretching.

In the approach part of the force curve, a single protein is picked up from a dense layer by the SFM tip because of an applied contact force. An array of peaks in the retraction trace is caused by unfolding processes of individual protein domains. The

height u of these peaks is used to calculate the unfolding force and the distance z between peaks is used to measure the length of the unfolded protein regions.^[105] Single-molecule force spectroscopy using SFM has gained tremendous importance in the study of protein misfolding phenomena and provides quantitative insights into the nature of molecular interaction of different receptor-ligand systems.^[106-108]

2.2 Material-dependent working modes of scanning electron microscopy

Scanning electron microscopy (SEM) provides information about the surface topography and composition by scanning a sample with high-energy electrons that are focused into a small beam by a series of electromagnetic lenses in the column of an SEM instrument. The electrons are generated by a thermal emission source (e.g. a heated tungsten filament) or by a field emission cathode and then accelerated towards a grounded anode plate, which is maintained at a positive voltage relative to the cathode in order to create an electrostatic field. A grid cap (Wehnelt cylinder) located between the electron emitter and the grounded anode is maintained at a slightly more negative potential compared to the filament, and thus, it allows a first rough focusing of the electrons on accelerating towards the anode. Depending on the evaluation objectives and the specimen under study, accelerating voltage may vary between 0.2 kV and 30 kV. The interaction or signal generation volume has a teardrop shape and a penetration depth of about 3 μm (Fig. 9). The penetration depth is affected by the specimen density and accelerating voltage.^[109] A higher accelerating voltage will give the electrons a higher speed and penetrating power. Moreover, working at higher acceleration voltages requires conductive and properly grounded samples. Incident electrons accumulate on the surface in case there is no conductive path available which would allow them to escape. This effect is evident by excessively bright areas of the sample, especially along edges. Localized melting and damage, especially of organic surface materials, can also be caused by beam-sample interaction. In order to prevent surface charging artefacts and damage, insulating specimens (e.g. polymers and biological materials) can be coated with a thin conductive layer of either metal or carbon.

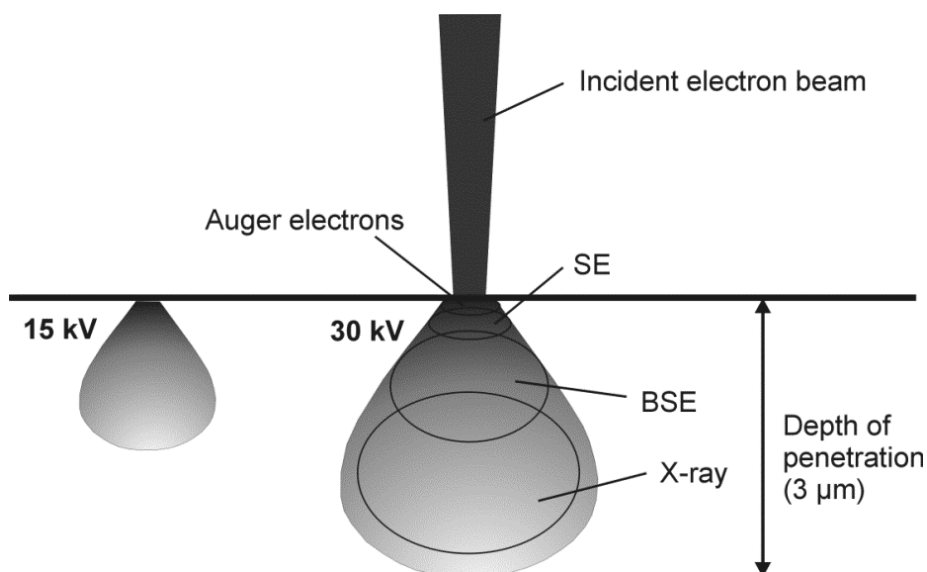


Figure 9. Schematic representation of processes resulting from electron-sample interaction. A variety of signals (e.g. backscattered electrons (BSE), secondary electrons (SE), characteristic X-rays and Auger electrons) is produced when electrons interact with atoms of the sample. The depth of penetration increases with increasing accelerating voltages (comparison 15 kV and 30 kV).

The interaction of the incident electron beam with atoms of the sample surface produces a variety signals, such as backscattered electrons, secondary electrons, characteristic X-rays (Fig. 9) and Auger electrons.^[109] While characteristic X-rays permit an elemental analysis of the specimen, secondary electrons (SE) and backscattered electrons (BSE) are commonly used for imaging. The latter are basically primary incident electrons that turn back from deeper sample layers without an energy loss (elastic collisions between beam electrons and specimen nuclei). The intensity of the detected electron signal is directly related to the atomic number of the specimen. For example, materials with a high atomic number would provide a brighter contrast than materials with a lower atomic number. Due to their high energy (> 50 eV), it is difficult to deflect them to the detector. Therefore, the intensity of BSE is very low and the surface topography cannot be as accurately resolved. Low-energy (< 50 eV) electrons emitted from an outer shell of a specimen atom upon impact of the incident electron beam are called secondary electrons (inelastic collisions between beam electrons and specimen electrons). Different to the high-energy BSE, they are generated close to the sample surface and can leave the sample with a high probability to be collected at the detector.

Due to the small interaction volume (between 5 and 50 nm) compared to that of BSE, much smaller surface feature can be resolved using the SE imaging mode. This mode provides a more surface-driven and less composition-influenced image contrast. The amount of emitted electrons at edges and curvatures is higher than on flat surface regions. However, holes where only a small fraction of SE can escape appear darker. By changing the tilt angle of the sample stage relative to the detector, the SE contrast can be increased. In this thesis, the SE imaging mode was useful for the study of thin nanostructured layers including for example two-dimensional AuNPs arrays on APTES-modified ITO samples (Chapter 6.1), as well as polymeric matrices with nanocavities formed upon an extraction of template AuNPs from NIPs (Chapter 6.3). Although, the detection of emitted X-rays would provide an elemental analysis of specimen using energy dispersive X-ray spectroscopy (EDX) inside the SEM chamber, it is not applicable to such thin layers (approximately 30 nm), because the sensitivity is insufficient for such thin layers considering the other X-rays originating from a surface layer of approximately 2-3 μm . A single X-ray is produced when the incident electron beam ejects a tightly bound inner shell electron (means the SE) of the specimen atom and a weakly bound outer shell electron relaxes to the vacancy under emission of X-rays. Detecting the emitted X-ray photon and measuring its energy allows the determination of element from which it was emitted, i.e. a constituent of the sample material.

In a conventional SEM, the sample chamber and the electron column are at a high vacuum (between 10^{-6} and 10^{-7} mbar) in order to avoid interaction between the electron beam and residual gas molecules. However, this technique has been further developed so that operation under environmental (typically a few tens of mbar) and wet conditions is also possible. This improvement prevents charge accumulation from bombardment by the electron beam at non-conductive samples by the presence of positively charged gas ions (usually water vapor), which compensates the negative charge of the electrons. Thus, environmental scanning electron microscopy (ESEM) has proved to be a successful method for the study of insulating and/or moist specimens without conductive surface-coatings, which means that native and hydrated surfaces can be explored.^[110-114]

2.3 Electrochemistry of metal nanoparticles and complex formation

The electrochemistry of NPs in general has received attention from various perspectives. Initial work used electrochemistry to prove quantized charging of very small, monodisperse nanoparticles.^[115, 116] Bard et al.^[117] used differential pulse voltammetry to determine oxidation and reduction potentials of semiconducting NPs in order to estimate the size-dependent positions of valence band and conduction band edges.

More recently the groups of Bard and Compton advanced the methodology of single NP collision experiments.^[118-120] Typically, the working electrode is an amperometric microelectrode of micrometer size. When using diluted NP solutions individual collisions of NPs are clearly separated in time. There are several versions of this experiment. When a sufficiently high potential is applied, all colliding NPs are immediately oxidized. Integrating the $I(t)$ peak provides the faradaic charge for each NP, which can be converted to obtain the size of the NP. Statistical analysis of such data can provide a size distribution (from the histogram of individual oxidation charges) and a concentration (from the collision frequency). A related approach uses the NP as catalyst. While the NP is attached to a catalytically non-active microelectrode it can temporarily catalyze a reaction such as hydrazine oxidation, that would not proceed on the bare microelectrode.^[121] More recently, Ahn and Bard^[122] enabled for the first time the observation of NP collisions events on an isolated large electrode area by tunneling electron transfer across a dielectric surface layer made of a thin film of titanium dioxide. For these experiments it is very important to control a complete oxidation (for NP sizing) or the absence of surface oxidation when electrocatalytic detection is the aim.

In this thesis, linear sweep voltammetry (LSV) is used for a complete oxidation of an assembly of NPs. This reaction (similar to complete oxidation in single NP collision experiments) is strongly influenced by complexing ligands in the working solution. In this work, it contains 3 M KCl as electrolyte and as complexing agent to facilitate the electrochemical dissolution of AuNPs. Gold ions Au^{3+} form a tetrachloroaurate(III) complex $[\text{AuCl}_4]^-$ with 4 chloride ions. This causes the redox reaction of gold to occur at a less positive potential than in the ligand free solution. The equilibria in Eq. (4-5) will be established.



If only equilibrium (4) is relevant, i.e. in the absence of chloride or any other complexing agent, the potential E is given by Eq. (6):

$$E = E_{(\text{Au}/\text{Au}^{3+})}^{\circ'} + \frac{RT}{n_z F} \lg \frac{c(\text{Au}^{3+})}{c^\circ} = E_{(\text{Au}/\text{Au}^{3+})}^{\circ'} + \frac{RT}{nF} \lg \frac{c_t}{c^\circ} \quad (6)$$

where $E_{(\text{Au}/\text{Au}^{3+})}^{\circ'} = 1.19 \text{ V}^{[123]}$ (vs. Ag/AgCl) is the formal potential of gold in aqueous solution, R the gas constant, T the temperature, F the Faraday constant, $n_z = 3$ the number of transferred electrons, $c(\text{Au}^{3+})$ the dissolved concentration of $\text{Au}(\text{H}_2\text{O})_4^{3+}$ (equal to the total dissolved metal ion concentration c_t) and $c^\circ = 1 \text{ mol L}^{-1}$ the standard concentration. The shift of the formal potential of the gold electrode $\Delta E^{\circ'}$ can be calculated by rewriting the Nernst-Equation (6) using the logarithm of the conditional brutto stability constant $\lg(\beta'/c^{\circ 4}) = 21.30^{[124]}$ of the complex [Eq. (7)].

$$\beta' = \frac{c(\text{AuCl}_4^-)}{c(\text{Au}^{3+}) \cdot c(\text{Cl}^-)^4} \quad (7)$$

$$E = E_{(\text{Au}/\text{Au}^{3+})}^{\circ'} + \frac{RT}{3F} \lg \frac{(c^\circ)^4}{\beta'} + \frac{RT}{3F} \lg \left(\frac{c^\circ}{c(\text{Cl}^-)} \right)^4 + \frac{RT}{3F} \lg c(\text{AuCl}_4^-) \quad (8)$$

In case of a large excess of ligand $c(\text{Cl}^-) \gg c(\text{Au}^{3+}) + c(\text{AuCl}_4^-)$, the concentration of the complex can be equated to the total concentration c_t of metal ions, i.e. $c_t = c(\text{Au}^{3+})$ in Eq. (6) and $c_t \approx c(\text{AuCl}_4^-)$ in Eq. (7).

$$E \approx E_{(\text{Au}/\text{Au}^{3+})}^{\circ'} + \frac{RT}{3F} \lg \frac{(c^\circ)^4}{\beta'} + \frac{RT}{3F} \lg \left(\frac{c^\circ}{c(\text{Cl}^-)} \right)^4 + \frac{RT}{3F} \lg \frac{c_t}{c^\circ} \quad (9)$$

When rewriting Eq. (9) as a formal potential $E_{(\text{Au}/[\text{AuCl}_4^-])}^{\circ'}$ in the presence of a fixed ligand excess as

$$E = E_{(\text{Au}/[\text{AuCl}_4^-])}^{\circ'} + \frac{RT}{3F} \lg \frac{c_t}{c^\circ} \quad (10)$$

it follows for $E_{(\text{Au}/[\text{AuCl}_4^-])}^{\circ'}$

$$E_{(\text{Au}/[\text{AuCl}_4]^-)}^{\circ'} \approx E_{(\text{Au}/\text{Au}^{3+})}^{\circ'} + \frac{RT}{3F} \lg \frac{(c^\circ)^4}{\beta'} + \frac{RT}{3F} \lg \left(\frac{c^\circ}{c(\text{Cl}^-)} \right)^4 \quad (11)$$

Consequently, the difference of the formal potentials $E^{\circ'}$ at 298 K is

$$\Delta E^{\circ'} = E_{(\text{Au}/\text{Au}^{3+})}^{\circ'} - E_{(\text{Au}/[\text{AuCl}_4]^-)}^{\circ'} \quad (12)$$

$$= -\frac{R \ 298\text{K}}{3F} \lg \frac{(c^\circ)^4}{\beta'} - \frac{R \ 298\text{K}}{3F} \lg \left(\frac{c^\circ}{c(\text{Cl}^-)} \right)^4 \quad (13)$$

$$= -\frac{0.059\text{V}}{3} (-21.30) - \frac{4 \cdot 0.059\text{V}}{3} \lg \frac{1}{3} \quad (14)$$

$$= 0.46 \text{ V} \quad (15)$$

In other words, the oxidation of gold occurs above 1.19 V vs. Ag/AgCl without a complexing agent, whereas in the presence of 3 M KCl it is expected already at 0.73 V (shifted by 0.46 V).

It should be noted that single particle collision experiments implicitly assume a complete oxidation upon each collision or a 100 % sticking coefficient. There is some discussion to which extent such an assumption is realistic in particular considering the variety of different ligand shells, their possibilities of interactions as well as their passivating properties.^[125] In this thesis it was the aim to detect NP depending on their ligand shell. This requires a selective recognition that has not yet been demonstrated with single particle collision experiments. Enriching the NP at the interface has the important advantage that it opens the way for using complementary detection methods such as electrochemical conversion, imaging by SEM, SFM or analysis by XPS. The use of such complementary techniques is heavily exploited in this thesis

3. Assembly of nanoobjects in rigid matrices

This chapter provides a brief introduction to nanoparticle self-assembly and gives a better understanding of specific and non-specific interactions between NPs and NIP systems (Chapter 3.1 and 3.2). In Chapter 3.3 a NIP-related model is discussed, which is well known as a molecularly imprinted polymer (MIP) for selective recognition of molecules and larger structures (e.g. peptide, protein and cells). Chapter 3.4 summarizes the existing NIP systems and describes two different strategies for the preparation of NIPs used in this work.

3.1 Assembling two-dimensional NP arrays

The construction of two-dimensional (2D) and three-dimensional (3D) NP arrays with tunable interparticle distances is of utmost importance for the development of novel electronic devices and biosensing applications.^[126] Precise control over uniformity (size, shape, composition, surface chemistry) of nanoparticles permits quasicrystalline nanoparticle assemblies, which provide a new class of highly ordered close-packed solids with unique size-dependent properties.^[127-129] From the fundamental perspective, there is a great effort to understand the key parameters affecting the assembly of colloidal films. This often includes the NP nature and surface functionality, the substrate properties and their interaction with the environment. To date, a variety of approaches exist for the controlled assembly of NP arrays, involving for example the self-assembly (no force applied) or the guided self-assembly (requires an external force).^[130] Self-assembly of NPs describes the process in which building blocks spontaneously organize into ordered aggregates or networks by controllable thermodynamic conditions.^[131] These assemblies are for example caused by the electrostatic, covalent or metal-ligand interactions between NP and interfaces. The Langmuir-Blodgett (LB) technique combines both the self-assembly and the guided self-assembly technique.

As the focus of this project rests on the design of thin-layered NIPs as the recognition element for efficient sensing devices, the following two chapters represent general approaches used for the 2D assembly of NP arrays including closely packed and randomly packed systems. Since a larger interparticle distance would provide a more

stable architecture of the polymeric matrix after removal of NPs, the construction of closely-packed NP arrays is not a necessary criterion for the realization of NIPs.

3.1.1 Electrostatic attachment

In order to achieve electrostatic interaction, the corresponding substrate surface and the surface of the NP must be opposite charges. The oppositely charged species are held together by strong ionic bonds resulting in an uniform and stable colloidal film. The ionic strength of colloidal solutions is a crucial parameter affecting the distribution and amount of immobilized NPs. A density-controlled adsorption of citrate-stabilized AuNPs with a random, but well-spaced distribution onto APTES-modified silicon surfaces was shown by William et al.^[132] to be easily attainable by varying the ionic strength of the NP solutions. With increasing ionic strength, the thickness of the electrical double layers at the substrate surface and the NP decreases (according to the Deyagin-Landau and Verwey-Overbeek (DLVO) theory).^[133-135] Consequently, the electrostatic repulsion between particles and hence the inter-particle distance decrease leading to the increase in NP density at the substrate surface.

In this work, the attempt was made to immobilize citrate-capped AuNPs by electrostatic attraction on APTES-modified ITO samples (Chapter 6.1). The self-assembly of NPs was carried out at pH 5 where the carboxylic groups of the NPs surface and the amino groups at the sample surface are oppositely charged. As made evident by many studies, the amount of NPs strongly depends on the pH and the exposure time the APTES-modified ample to AuNP solution.^[136-138]

3.1.2 Langmuir-Blodgett with nanoobjects

One of the most widely used methods for the assembly of 2D nanoparticle arrays is the Langmuir-Blodgett (LB) technique,^[139-142] which has been long used to assemble molecular mono- or multilayers.^[143, 144] With this technique, the NPs are allowed to self-assemble on a liquid-air interface guided by a mechanical force, which result from decreasing the surface area of a single NP. At a chosen surface pressure, the layer can be transferred from the liquid-air interface to the surfaces of a solid sample. Consequently,

this technique offers the possibility of preparing reproducible NP arrays with the control of interparticle distance.

The ability to realize NPs-matrix systems in one assembly step is the major advantage of the LB technique for the preparation of NIPs. Two-dimensional nanocomposites composed of an organic LB film and NPs have been assembled by formation of the NPs directly at the water-air interface,^[145, 146] by codispersion of the two components,^[147, 148] and by electrostatic extraction of the NPs from the subphase into the LB film.^[149, 150] The latter one was used for the realization of the poly(aniline)-based NIP system discussed in Chapter 5.4. Chapter 5.3 shows another appealing approach for the realization of NP-matrix systems, in which the attempt was made to incorporate Fe₃O₄-NPs into LB-layers made of amphiphilic oleic acid molecules.

3.2 Specific and non-specific interaction of nanoobjects with surfaces

In the case of proteins, nanoobjects or cells, the surfaces of these objects may expose a large diversity of functional groups. When contacting to a solid surface, some weak interaction is typically observed for each combination of solid surfaces and cells or nanoobjects. Such interaction is called non-specific. In fact, specific measures are required to suppress adsorption of proteins, for instance by coating surfaces with layers containing oligoethylene glycol (OEG) groups.^[151] According to Herrwert et al.^[152] the suppression of non-specific protein adsorption (and consequently cell adhesion) by OEG-terminated surfaces is based on the combination of three factors, namely the internal hydrophilicity of the OEG layer, the hydrophobicity of the terminal groups of a packed arrangement of OEG chains and the lateral packing density for instance within a SAM. Surfaces equipped with SAM preventing non-specific adsorption can be manipulated chemically. This typically lifts the restrictions for non-specific adsorptions. This has been used for surface patterning adherent cells on surfaces.^[153]

In contrast, a specific interaction refers to a pair of receptor and analyte, such as antigen-antibody, complementary single-stranded desoxyribonucleic acids (ssDNA) or hormones-hormone receptors. This requires complementary arrangement of functional

groups able to generate a tight binding by multiple weak interactions by H-bridges, coulomb interaction or dispersion forces. Due to the strong distance dependence of dispersion interaction, a close geometric fit is required between the binding partners. When transferring the concept to MIPs and NIPs, specific interaction refers to the interaction of the template or analyte to the binding pocket of the MIP and NIP. Since the matrix usually exposes the interacting functional groups at its surface, but outside the binding pocket, there will always be a tendency to bind nanoobjects at the surface outside the binding pocket or cavity. This interaction is therefore called non-specific.

In the context of molecular imprinted polymers (MIP, Chapter 3.3) the imprinting factor (IF) describes the ratio between the amount of target molecules bound to the MIP and the amount of target molecule bound to the non-imprinted polymer. If binding of molecules is favored by non-specific interaction, a low IF is expected as the target molecule interacts to the same extent with imprinted and non-imprinted polymers. The IF can be increased by reducing the non-specific interaction *and* incorporating specific binding sites during the imprinting process.

3.3 Molecular imprinting

Molecularly imprinted polymers (MIPs) are produced by imprinting technology and provide robust materials with predictable molecular selectivity. The idea of molecular imprinting was proposed and introduced by Wulff and coworkers to mimic natural systems where biomolecules are recognized by receptors.^[154] The methodology and concepts of MIPs can be applied to nanoobjects where the aim is to develop the basis of nanoobjects imprinting systems, which will selectively recognize NPs based on their size, shape and interactions with a thin film.

3.3.1 Preparation and application of MIPs

MIPs are polymers that are formed in the presence of a template (imprinted) molecule. This process involves crosslinking functional monomers around the selected molecular template to create a polymer matrix offering recognition sites based on the interactions between template molecule and functional monomers. After polymerization the template

is removed from the polymer leaving a complementary well-defined cavity, which can selectively reuptake the template. A schematic illustration of the imprinting process is presented in Fig. 10.

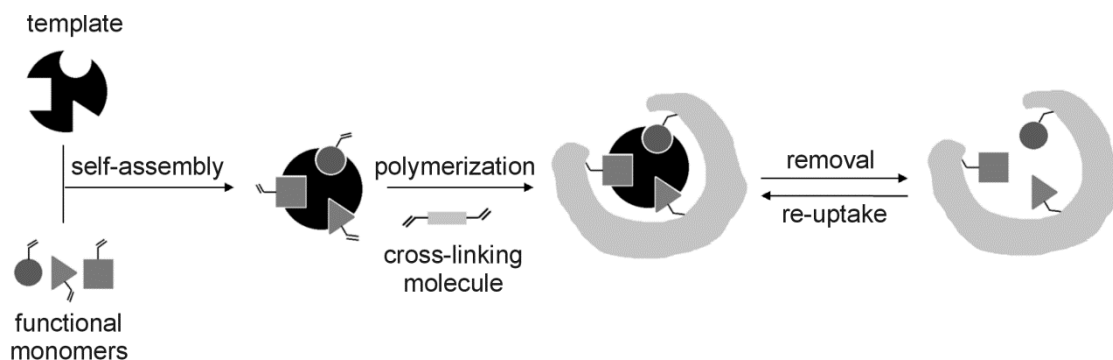


Figure 10. Schematic of the MIP principle including the self-assembly process of template and functional monomers, polymerization in the presence of a cross-linking molecule, the removal and selective reuptake of the template.

The most common methods for introduction of functionality into the recognition sites of imprinted sites are covalent, noncovalent and semi-covalent approaches. Wulff and coworkers^[154] introduced the MIP concept more than three decades ago based on the covalent imprinting approach, which involves a chemical reaction between the template and the functional monomer. However, rebinding to the polymer by the formation of covalent bonds is too slow for many potential applications including chromatography.^[155] Noncovalent imprinting is one of the most commonly used methods for the preparation of MIPs and was mainly devised by Mosbach et al..^[156-159] The advantages of the noncovalent approach are the coexistence of various intermolecular interactions, which enables a quick self-assembly of the monomer-template complex. Typical noncovalent interactions are hydrogen bonding, ion-pairing and dipol-dipol interactions. The main disadvantage compared to the covalent imprinting process is an unpredictable stability of the complex during the polymerization process. Combining the advantages of both attachment strategies is referred to semi-covalent imprinting, where the template is covalently attached to the monomer during polymerization, whereas the rebinding step is based only on non-covalent interaction.^[160]

The standard method for the construction of MIPs involves bulk polymerization of template, functional monomer, and the cross-linking reagent in the presence of a solvent,

which acts as porogen. Porogenic solvents are necessary for the creation of large pores, in order to assure good flow-through properties of the resulting polymer. After completion of the polymerization process, the resulting monolithic block is grinded and sieved into particles with sizes in the micron range depending on their final application. This method is simple, but also time consuming and yields only moderate amounts of useful imprinted polymers. The polymer particles obtained are often irregular in size and shape. Moreover, the grinding steps can destroy some recognition sites, which reduce the binding capacity of MIPs.^[161-163] In order to overcome these limitations, a number of alternative methods to prepare novel MIP formats have been developed, such as producing MIP beads via suspension,^[164, 165] and precipitation polymerization,^[166, 167] producing molecularly imprinted thin films or membranes,^[168, 169] and surface imprinting,^[170, 171] especially for imprinting large molecules (e.g. biomacromolecules and proteins). The latter is detailed in Chapter 3.3.2.

MIPs can be employed in a variety of applications, such as chromatographic separation, sensors, catalysis, and drug delivery systems. Using MIPs as chiral stationary phase (CSP) in chromatographic applications enables for example the separation of enantiomers containing one or more stereogenic centers. In this manner nonspecific interaction, which affects both enantiomers equally, are eliminated.^[155]

3.3.2 Surface imprinting

Imprinting of small, organic molecules like pharmaceuticals, pesticides, amino acids and peptides, steroids, and sugars is now a well-established and almost routinely used technique. Although, MIPs have also been prepared for target macromolecules, imprinting of large structures (e.g., proteins,^[172, 173] cells,^[174] mineral crystals^[175]) is still a challenging task in terms of selective macromolecular recognition.^[176] This can be attributed to the fact that most macromolecular templates are less rigid, which does not facilitate the formation of well-defined binding cavities during the imprinting process. Furthermore, rebinding is also difficult, since the ability of large structures to penetrate the polymer network is limited.

Only a small number of studies exist on the imprinting of macromolecules, whereas surface imprinting in this area seems to be promising. Surface imprinting

techniques overcome the limitations imposed by the small diffusivity of proteins in the highly cross-linked MIP structures by generating binding sites exclusively on the surface of the imprinted polymers and simultaneously providing high surface area/volume MIPs.^[171, 177] Gyurcsányi and coworkers^[178] proposed a versatile approach based on nanosphere lithography to generate surface-imprinted polymers for selective recognition of the avidin (Av) protein. This concept is shown schematically in Fig. 11a. A layer of 750 nm diameter Av-modified latex beads were deposited onto the surface of gold-coated quartz crystals followed by the electropolymerization of poly(3,4-ethylenedioxythiophene)/poly(styrenesulfonate) (PEDOT/PSS) film with thicknesses of the order of the bead radius. The removal of the polymer bead-protein conjugates is facilitated by using a cleavable protein-nanosphere linkage (NHS-S-S-biotin). The surface-imprinted polymer films show remarkable selectivity toward Av and analogues (i.e. extravidin, streptavidin, neutravidin) and the binding capacity is ca. 6.5 higher than of polymers imprinted with unmodified beads. The investigation of the binding process was performed via the nanogravimetric method using an electrochemical quartz crystal microbalance. Surface plasmon resonance (SPR) imaging offers another opportunity for simultaneous label-free determination of MIP binding sites by measuring changes in the reflective index of a media near a thin metal layer.^[179]

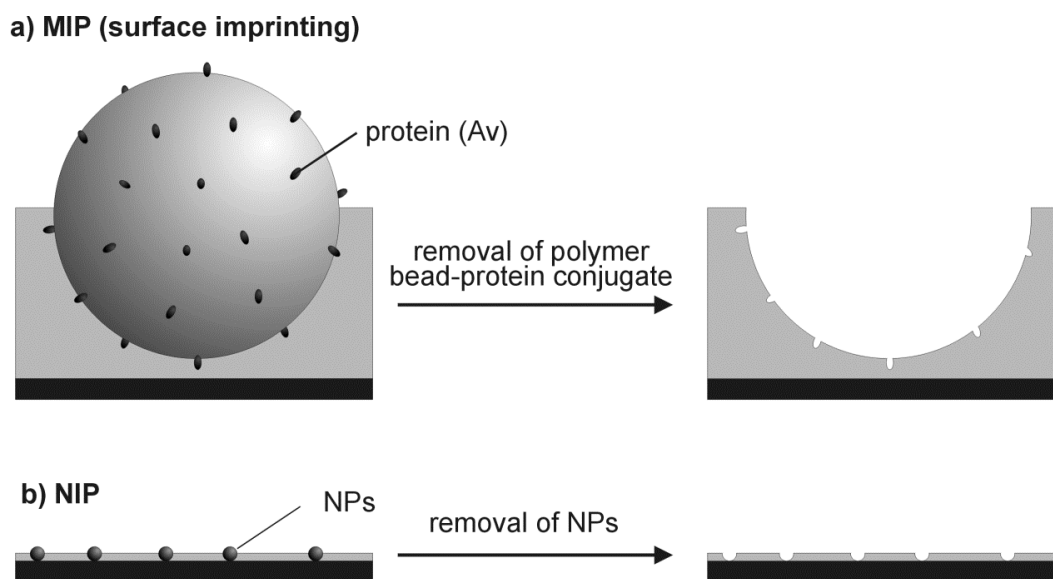


Figure 11. Electrosynthesis of a) molecularly surface-imprinted polymer films by nanosphere lithography for selective recognition of proteins and b) NP imprinted matrices for selective recognition of NPs.

The NIP systems developed in this thesis use the NP as the analyte itself rather than as a platform for surface anchoring a macromolecular target (Av) in the surface imprinting approach (Fig. 11b).

3.4 Nanoparticle imprinted matrices

Nanoparticle imprinted polymers as bulk material were introduced by Koenig and Chechik,^[29] who used polymerizable ligands to stabilize AuNPs. After cross-linking of ligands, the Au core was chemically etched. The resulting NIP showed selective sorption of small AuNPs. But, there was no attempt to form thinner NIP films or to use the brittle material as sensing tool. Another related approach termed nanosphere lithography (NSL), is an inexpensive nanofabrication technique capable of producing a large variety of nanoparticle structures and well-ordered 2D nanoparticle arrays.^[180, 181] Yet, this approach does not attempt to reuptake the spheres and therefore to introduce selectivity.

After the first demonstration of thin film NIP concepts, in which the author was participating (Chapter 5.4), a further NIP system was developed by Bruchier-Spanier and Mandler.^[182] In this study, monolayers of cellulose acetate (CA) and AuNPs stabilized

with dodecanethiol are simultaneously transferred onto ITO by the LB technique. After electrochemical removal of AuNPs, the matrix is capable of recognizing NPs based on their shell. The matrix system shows the ability to re-capture the original dodecanethiol-stabilized AuNPs. However, AuNPs with the same size but different ligand shell were almost not recognized by the matrix.

For the preparation of NIPs in this thesis two different routes were followed. The first one comprises the deposition of thin film NIP composites in one step (Chapter 5). In the second one, NIP systems are realized by a sequential deposition of template NPs and followed by the matrix (Chapter 6).

4. Experimental details

4.1 Chemicals

Table 2 lists chemicals which were used in this thesis for surface preparation as well as for sample treatment and characterization. The main constituents used for NIP formation are separately listed in Table 3 and 4. If not stated otherwise, all chemicals were of analytical grade and were used without further purification. Aqueous solutions were prepared using deionized water (ELGA LabWater, Celle) with a resistance of 18.2 MΩ cm at room temperature.

Table 2. Chemicals used for surface preparation as well as for sample treatment and characterization.

Product	Formular	Supplier	Grade
chloroform (anhydrous)	CHCl ₃	Sigma Aldrich	≥ 99.0 %
ethanol (absolute ethanol)	C ₂ H ₅ OH	Fisher VWR	99.5 %
isopropyl alcohol (normapur)	C ₃ H ₇ OH	VWR International	100.0 %
toluene (absolute, over molecular sieve)	C ₇ H ₈	Sigma Aldrich VWR	≥ 99.7 %
n-hexane (Normapur)	C ₆ H ₆	VWR International	98.2 %
ammonium hydroxide 25 %	NH ₄ OH	Merck	25.0 %
hydrogen peroxide 30 %	H ₂ O ₂	Fluka	≥ 30.0 %
hydrochloric acid 37 %	HCl	VWR International	35.9 %
sulfuric acid 96 %	H ₂ SO ₄	Merck	95.0 %
nitric acid 65 %	HNO ₃	Roth Sigma Aldrich	65.0%
arachidic acid	C ₂₀ H ₄₀ O ₂	Sigma Aldrich	≥ 99.0 %
L(+)-ascorbic acid	C ₆ H ₈ O ₆	Roth Sigma Aldrich	≥ 99.0 %
potassium cyanide	KCN	Sigma Aldrich	≥ 96.0 %
sodium dihydrogen phosphate dihydrate	NaH ₂ PO ₄ · 2H ₂ O	Merck	99.0 %
potassium chloride	KCl	Sigma Aldrich	≥ 97.0 %
hexaamineruthenium(III) chlorid	[Ru(NH ₃) ₆]Cl ₃	Sigma Aldrich	98.0 %

Experimental details

Table 3. Chemical compounds used for organic thin film fabrication.

Product	Formula	Supplier	Grade
oleic acid	$C_{18}H_{34}O_2$	Sigma Aldrich	$\geq 99.0\%$
3-(aminopropyl)triethoxysilane	$C_9H_{23}NO_3Si$	Fluka	99.0 %
phenol	C_6H_5OH	Sigma Aldrich	99.0 %
Sylgard® 184 Silicon Elastomer Kit	$[C_2H_6OSi]_n$	Dow Corning Corporation, Midland, MI, USA	-

Table 4. Nanoparticles used for imprinting processes and reuptake experiments.

Product	Abbreviation	Supplier	Concentration
oleic acid stabilized iron oxide NPs (\varnothing 10 nm) in toluene (> 1 % OA stabilizing agent)	Fe_3O_4 -NPs	Sigma Aldrich	5 mg/mL
gold NPs (\varnothing 30 nm), stabilized suspension in citrate buffer (< 12% variability in size/shape)	AuNPs	Sigma Aldrich	$\sim 1.8 \cdot 10^{11}$ NPs/mL
gold NPs (\varnothing 50 nm), stabilized suspension in citrate buffer (< 12% variability in size/shape)	AuNPs/50	Sigma Aldrich	$\sim 3.5 \cdot 10^{11}$ NPs/mL
gold NPs (\varnothing 10 nm), stabilized suspension in citrate buffer (< 12% variability in size/shape)	AuNPs/10	Sigma Aldrich	$\sim 6 \cdot 10^{12}$ NPs/mL
silver NPs (\varnothing 20 nm), stabilized suspension in citrate buffer (< 13% variability in size)	AgNPs/	Sigma Aldrich	0.02 mg/mL
alternatively: silver NPs (\varnothing 20 nm \pm 3 nm), citrate stabilized (< 15% variability in size)	AgNPs	Nano Composix	0.05 mg/mL

4.2 Instrumentation used for preparation and characterization of samples

Contact angle meter. The wettability of the surfaces was determined with the contact angle meter OCA 15plus (equipped with a CCD camera) from Data Physics (Filderstadt, Germany). The data were analyzed with the software SCA 20 (version 1.0.0).

Polarization modulation infrared reflection adsorption spectroscopy (PM IRRAS). This technique was used to characterize LB layer consisting of OA and OA-stabilized Fe_3O_4 -NPs and of the ligand shell of the iron oxide nanoparticles. PM IRRAS spectra were acquired by the utilization of a Vertex 70 spectrometer and an external reflection setup

(Bruker, Ettlingen, Germany) containing a photoelastic modulator (PEM) PMA 50 (Hinds Instruments, Hillsboro, OR, USA). The half wave retardation was set to 1600 cm^{-1} or to 3000 cm^{-1} . The resolution of the spectra was 4 cm^{-1} . The PM IRRA spectra were baseline (Bessel function) corrected using the OPUS software version 5.5 (Bruker, Germany). A detailed procedure is described in Ref.^[183].

Electrochemical experiments. Cyclic voltammograms (CVs) and Linear sweep voltammograms (LSVs) were recorded at room temperature using potentiostats CHI 620A and 660A (CH Instruments, Electrochemical Analyzer, Austin, TX, U.S.A.) in a three-electrode configuration. As the current response is strongly affected by the area of the working electrode, experiments were performed in a homebuilt cell specified by a working area of 0.502 cm^2 (Fig. 12). Bare and modified ITO-coated glass slides as well as Au/glass substrates were used as working electrode, pressed against an O-ring (8 mm internal diameter) and a Teflon block with the liquid reservoir (Fig. 12). A platinum wire (0.566 cm^2) and Ag/AgCl/3 M NaCl (alternative Ag/AgCl/0.1 M KCl) electrode served as counter and reference electrodes, respectively. All potentials are referred to the used reference electrode.

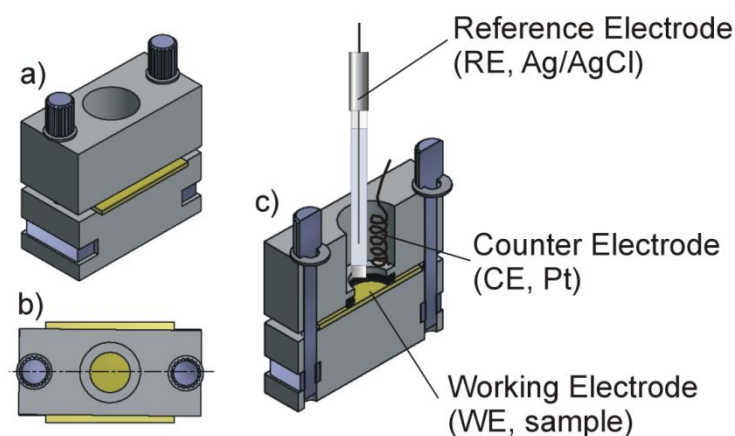


Figure 12. Electrochemical cell made from Teflon in three different views a) from the front, b) from the top and c) the vertical cross-section area showing the arrangement of the reference, counter and working electrode).

Scanning force microscopy. SFM was performed under ambient conditions with a Nanoscope IIIA controller and a Dimension 3100 or an Enviroscope stage (Veeco Instruments Inc., Santa Barbara, CA, USA) operating with a resolution of 256×256

pixels. The intermittent and the contact mode were used for topography imaging. Intermittent mode images were collected at a scan rate of 1.5-3.0 Hz using an Al-coated Si₃N₄-cantilever (NCHV-A tip, Bruker Corporation, Billerica, MA, USA) with a nominal spring constant of 42 N m⁻¹. Contact mode images were obtained at a scan rate of 1.5-7.1 Hz using an Au-coated Si₃N₄-cantilever (MSCT tip, Bruker) with a nominal spring constant of 0.6 N m⁻¹. The pulsed-force mode images for simultaneous acquisition of topographical information, stiffness and adhesion properties of the polymer matrix were obtained with Si₃N₄-cantilever (Al-coated NFESPA tip, Bruker) with a nominal spring constant of 3 N m⁻¹) at a scan rate of 0.7 Hz.

The determination of polymers film thicknesses were conducted similar to literature procedures^[48, 49] with triangular Au-coated Si₃N₄-cantilever of a nominal spring constant of 0.6 N m⁻¹ using the SFM contact mode. Before the measurement, the setup was allowed to equilibrate for 1-2 hours to minimize drift. First a 5 μm × 5 μm was imaged nondestructively with scan rate of 0.5-3.0 Hz and a set-point close to 0 V. From this image a region of 1 μm × 1 μm was selected and imaging was continued with a set-point of 10 V causing the tip to abrade the soft polymer layer until the typical structure of electrode became evident. Subsequently, a topographic image of the scratched region using low forces (set points between 0 and 1 V) was recorded at 1.5-7.1 Hz. The software Nanoscope Analysis 1.4 was used for offline analysis of the film thickness. It allows determination of two rectangular regions within a band in this region (Fig. 13a). One region was placed in the abraded part and one region on the undisturbed polymer. It is important to select those regions in such a way that they do not include polishing streaks or a high concentration of agglomerates. It is also required that they are located away from the rim of the abrasion crater because abraded polymer often accumulates close to the 1 μm × 1 μm abrasion region. The thickness was determined using the software tool "step height" that makes use of averaged height values of the undisturbed vs. the scratched region. An example is shown in Fig. 13. This greatly reduces the influence of surface roughness on the film thickness determination. Since the accuracy depends on the ability to place the two imaging frames away of any larger topographical features.

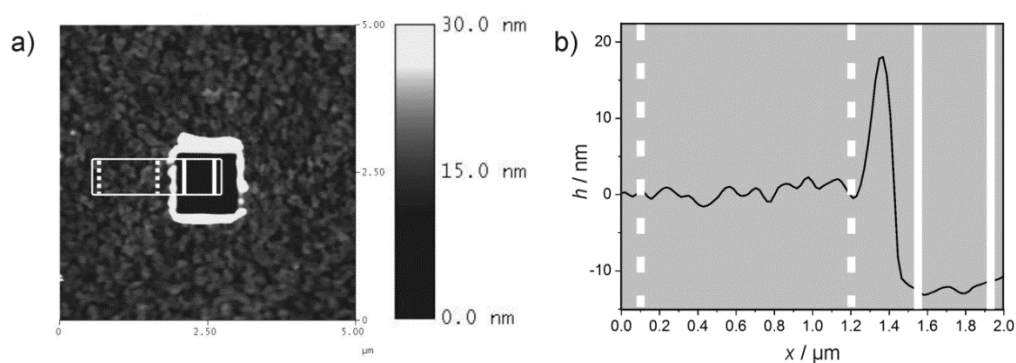


Figure 13. a) Example of SFM thickness determination after mechanical removal of the phenol-based polymer generated on ITO_{APTES} (2.5 Hz and at a set-point of 0 V); b) the corresponding cross section profile of the area marked by the white rectangle in a).

Friction signal images were recorded in the contact mode while scanning the probe over the surface at a scan angle of 90° at 1.5-7.1 Hz. Image flattening was performed with the first order, least-square polynomial function of the software Nanoscope V5.30r3sr3, which removes tilt and the vertical z -offset between line scans. The surface roughness is given in root mean square (RMS) values in a total area of $5 \mu\text{m} \times 5 \mu\text{m}$ (unless stated otherwise). If the impurities on the initial electrode surface influence the surface morphology, another, smaller area was chosen for measuring roughness. The height of different surface features was measured with the software tool "section analysis" as difference between the peak height and the average baseline.

Force vs. distance curves are used to measure the vertical force that the tip applies to the surface during scanning. Force-distance curves were recorded upon tip approach and retraction with a given value of spring constant $k = 0.6 \text{ N m}^{-1}$ (MSCT SFM tip) in the contact mode. The force F is obtained by multiplying the deflection of the cantilever with its spring constant k . The tip-sample separation (distance) can be calculated by adding the deflection to the position. However, in case of soft and deformable materials, such as polymers (Chapter 5.2), attractive forces and adhesion can cause an error of tip sample separation. In this work only the change of the adhesive force was of interest. Therefore the experimental points were shifted so that they had a common onset point of repulsive forces in the approach scan.

Scanning electron microscopy. Additional informations on surface morphology were obtained by SEM using a Helios Nanolab 600i system (FEI Company) with a through lens detector (TLD) at acceleration voltages of 1 to 30 kV. A conductive bridge of silver paste (Ferro GmbH, Hanau, Germany) was made between the sample holder and the upper conductive surface of the ITO samples. Images were recorded in the secondary electron mode with a TLD detector at working distances of 3-4 mm. Size distribution of template AuNPs and the diameter of remaining nanovoids in the polymer matrix after the removal of the NPs were determined with Image J software version 1.45s (Wayne Rasband, National Institute of Health, USA).

X-ray photoelectron spectroscopy (XPS). XPS was performed with an ESCALAB 250 iX (Thermo Fischer, East Grinstead, UK) using a monochromatized Al K α excitation (1486.6 eV). Data acquisition and spectra processing was performed with the Avantage Software v. 5.52. Si, O, Au, N, C were detected in the samples and high-resolution spectra were obtained. Measurements were performed of the NIPs before and after the release of AuNPs and of AuNPs before and after they were embedded into a PPh matrix. All spectra were corrected to the C 1s signal of ubiquitous hydrocarbon contaminations at 284.8 eV.^[184] Used parameters are listed in Table 5.

Table 5. Used parameters for XPS measurements.

Sample	Number of scans	Spot size [μm]	Pass energy [eV]	Step size [eV]
PANI/AuNP/ITO_before	50	650	20.0	0.1
PANI/AuNO/ITO_after	100	650	20.0	0.1
AuNP/ITO _{APTES}	5	500	20.0	0.1
PPh/AuNP/ITO _{APTES}	5	500	20.0	0.1
PPh/{ } _c /ITO _{APTES}	5	500	20.0	0.1

Fitted XPS spectra (Fig. 33 and 63) are given in the following way: solid symbols are measured points. Thick solid lines are background and sum of all components. If more than two components are present, individual components are indicated as thin lines.

4.3 General cleaning procedure

Glass slides were ordered from VWR International (Darmstadt, Germany) and ITO coated glass slides from Sigma Aldrich (Steinheim, Germany) specified by a surface resistivity of 8-12 Ω . In order to remove contaminations, glass and ITO substrates were cleaned in an ultrasonic bath (Bandelin Sonorex, Berlin) over 5 min in ethanol and then 5 min in water and dried in an argon stream. Subsequently, the surfaces were oxidized by UV/O₃ for 30 min using the UV TipCleaner (UV.TC.EU.003, Bioforce Nanoscience, Inc. Ames, IA, USA).

4.4 Preparation of gold surfaces

Gold surfaces were prepared onto cleaned glass slides as the support by depositing 0.5 nm of chromium and 200 nm of gold using an evaporation chamber (minicoater, Tectra GmbH, Frankfurt, Germany) while monitoring the thicknesses of deposited layers with a quartz crystal microbalance (Tectra GmbH, Frankfurt, Germany). The gold substrates were freshly prepared prior to each experiment and denoted as Au/glass.

4.5 Preparation of template stripped gold surfaces

The route to obtain ultra-flat TSG surfaces follows the strategy described in the diploma thesis of Röefzaad.^[185] Muscovite mica sheets (SPI Supplies, West Chester, PA, USA) were cleaved using adhesive tape and placed in the evaporation chamber. Unless stated otherwise, 100 nm thick gold layers were vapor-deposited onto the cleaved side of mica sheets which were subsequently glued to glass slides. The cleaned glass substrates were pretreated in piranha solution (2 volumes H₂SO₄: 1 volume 30% H₂O₂), thoroughly rinsed with water and dried in an argon stream, finally stored for 1 h at 120 °C. **Caution!** *This mixture reacts violently with all organic materials. The solution has to be handled with extreme care to avoid personnel injury and property damage.* After cooling to room temperature, the glass slides were glued on gold-coated mica und cured over night at 50° C, loaded with a steel block of 300 g ensuring a good compression between both substrates. Besides the recommended epoxy glue (Pattex Kraft-Mix, Henkel, Düsseldorf,

Germany) used in Ref.^[185], an alternative adhesive (UHU Plus Endfest 300, Bühl Germany) was used in this work. Both consist of two components (resin and hardener mixed in a volume ratio of 1:1). The alternative glue gave a great advantage in handling due to its longer processing time of 90 min and prevented the formation of dried lumps as observed in case of the Pattex glue (processing time 10 min). The mica-gold-sandwich can be kept for weeks under ambient conditions. To expose TSG surfaces, mica was carefully stripped off in successive layers with adhesive tape.

4.6 Immobilization of nanoparticles

4.6.1 Langmuir-Blodgett assembly of iron oxide NPs on TSG substrates

The LB technique was used in order to assemble OA-stabilized Fe₃O₄-NPs TSG substrates. The measurement of surface pressure-area (π -A) isotherms and LB transfer were carried out with an LB apparatus (KSV Instruments LTD, Helsinki, Finland) using the KSV NIMA LB software (version 1.81). The liquid reservoir (the LB-trough - surface area available for the surfactant: 228 cm²) and two moving Teflon barriers for monolayer compression (Fig. 14) were made from Teflon in the university machine workshop. Furthermore, the setup was equipped with an electrobalance that uses a Wilhelmy paper plate as the surface pressure sensor. The trough and barriers were rinsed with water first and ethanol afterwards, wiped with a chloroform-soaked Kim-wipe, and finally rinsed with ethanol and then with water. For all experiments, the clean trough was filled with water as the subphase. The water surface was cleaned by compressing the barriers to a maximum and gentle suctioning with a Pasteur pipette connected to a water pump such that the surface pressure remained below 0.2 mN m⁻¹ after moving barriers back to the start position. Pure OA and OA-stabilized Fe₃O₄-NPs (5 mg mL⁻¹ in toluene) were dissolved in chloroform to different concentrations - also with additional OA - and carefully dropped on the water subphase in appropriate volumes using a micro-syringe (Hamilton, Bonaduz, Switzerland). Table 6 gives a detailed overview on all concentrations of stock solutions and the spreading volumes (concentrations) used for LB experiments. All solutions were ultrasonicated for 3 min prior to use. After the solvent

was completely evaporated (~10 min for chloroform, ~20 min for toluene), the monolayer at the air/water-interface was compressed at a barrier speed of 10 mm min⁻¹ and the π -A-isotherm was recorded. During the transfer, the KSV NIMA LB software recorded surface pressure [mN m⁻¹] versus trough area [cm²].

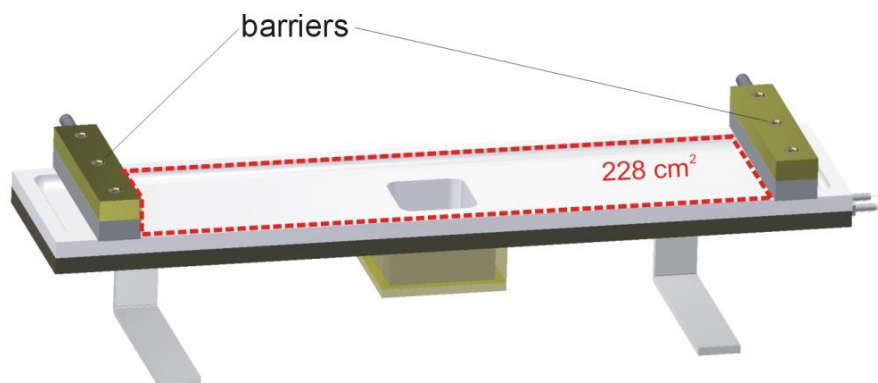


Figure 14. Homebuilt LB-trough (228 cm²) made from Teflon and equipped with two moving Teflon barriers for monolayer compression.

The LB transfer of NP-based Langmuir layer was enabled by pulling previously immersed substrates through the monolayer formed at the air-water interface with a speed rate of 5 mm min⁻¹ while keeping the surface pressure constant at selected values given in Table 6 (transfer pressure). Upon transferring LB-films at 20 mN m⁻¹, a slight excess of spreading amount was required since the barriers usually get in contact with the Wilhelmy-paper during the transfer. This disturbs the electronic feedback system for surface pressure control. All measurements were carried out inside a dust shield at room temperature.

Table 6. Concentration of stock solutions and spreading volumes: (A) oleic acid stabilized Fe₃O₄-NPs as supplied in toluene and (B) Fe₃O₄-NPs (solution in A) dissolved in chloroform with additional OA. The right column shows the surface pressure used for transfer of NP layers onto TSG or Au/glass substrates.

Exp.	Abbreviation	Concentration of stock solution	Spreading volume (concentration)	Transfer pressure
A	pure OA	1.0·10 ⁻³ mg μL ⁻¹	20 μL (2.0·10 ⁻² mg)	-
B	Fe ₃ O ₄ -NP + OA	NP: 1.0·10 ⁻⁶ mg μL ⁻¹ OA: 1.0·10 ⁻³ mg μL ⁻¹	465 μL (NP: 4.5·10 ⁻⁴ mg + OA: 1.5·10 ⁻² mg)	20 mN m ⁻¹

A previously measured arachidic acid isotherm shows a typical phase behavior as known from Ref.^[186, 187] proving the reliability of the homebuilt LB-trough and the absence of film leakage beneath the moving barriers. Figure 15 shows the dependence of π -A isotherm of arachidic acid obtained at the air-water interface with a compression speed of 10 mm min⁻¹. Three distinct regions show a) gas-like, b) liquid-like and c) solid-like behavior. They can be associated with the molecular arrangement of the monolayer in various phases as shown schematically in the Fig. 15. The collapse pressure π_c is identified as the onset of multilayer or aggregate formation.

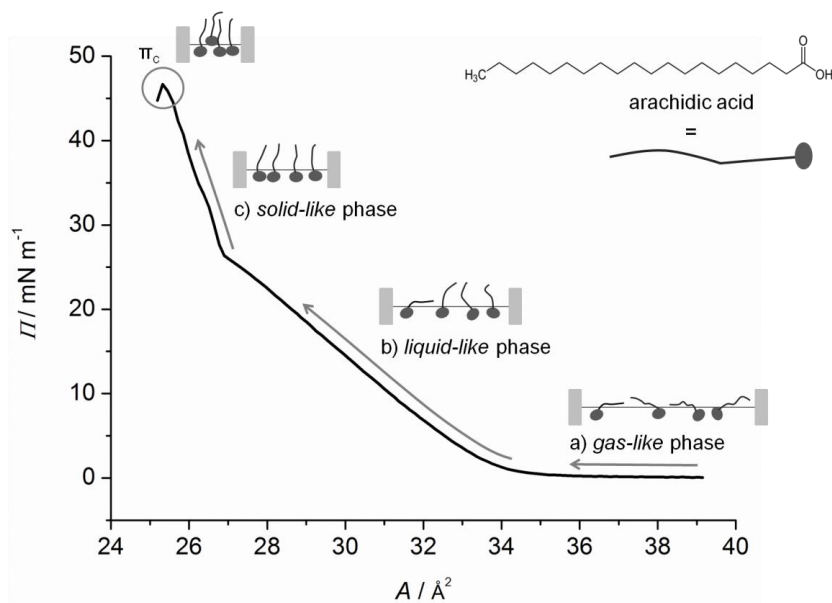


Figure 15: π -A isotherm of arachidic acid obtained at the air-water interface with a compression speed of 10 mm min⁻¹ and schematic illustration of the molecular arrangement of arachidic acid in various phases.

4.6.2 Attachment of gold NPs to APTES-functionalized ITO substrates

The silanization process on ITO introduced by Chen et al.^[188] was slightly modified. ITO substrates were cleaned in an ultrasonic bath (Bandelin Sonorex, Berlin, Germany) in ethanol and water (each 5 min) and dried in an Ar stream. Clean ITO surfaces were chemically pretreated in 1% NH₄OH solution over 1 h at 80 °C. After rinsing with water and drying in an Ar stream, the activated ITO electrodes were immersed in a solution of 1% APTES in dried toluene under Ar atmosphere. After treatment of 30 min, the silanized surfaces (ITO_{APTES}) were rinsed with ethanol and water and dried under a

stream of Ar. Based on SFM measurements, no differences in RMS roughness was observed between bare ITO vs. ITO_{APTES} (Fig. 16a, b).

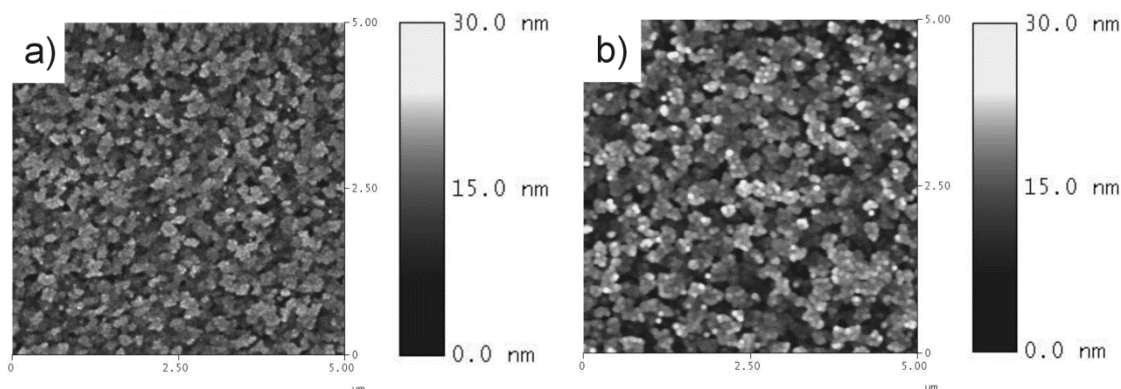


Figure 16. SFM topography images recorded in contact mode, with a MSCOT tip ($k = 0.6 \text{ N m}^{-1}$) of a) bare ITO with 2 Hz and b) ITO_{APTES} with 3.9 Hz (scan area: $5 \mu\text{m} \times 5 \mu\text{m}$).

Silane-modified ITO slides were immersed in a colloidal solution of citrate-stabilized AuNPs (30 nm diameter) for 24 h. The pH of this solution was adjusted to pH 5.0 with 0.1 M HCl solution and checked by a pH meter (Metrohm 632, Herisau, Switzerland). Previously, it was calibrated with two different commercial buffer solutions (pH 4.01 and 7.00, WTW, Weilheim, Germany). After immobilization of AuNPs, samples (AuNP/ITO_{APTES}) were rinsed with water and dried in a Ar stream. Additionally, the surface coverage of NPs on ITO_{APTES} was investigated after immobilization of AuNPs during 1 h, 2 h and 3 h.

4.7 Formation of thin matrices by electropolymerization of phenol

Thin poly(phenol) (PPh) films were prepared on cleaned ITO, ITO_{APTES} or on AuNP/ITO_{APTES} samples using the method described by Kang et al.^[189]. The electrodeposition was carried out by cyclic voltammetry in an aqueous solution containing 50 mM phenol and 0.1 M NaH₂PO₄. The potential was cycled in the range from 0 V to 1.9 V vs. Ag/AgCl at a sweep rate of 50 mV s^{-1} . After 30 potential cycles, samples were rinsed with water and dried in a slight Ar stream. These samples are denoted as PPh/ITO, PPh/ITO_{APTES} and PPh/AuNP/ITO_{APTES}. Blank polymers without template AuNPs were

used as control samples in order to estimate properties of the plain PPh layer. Under the same conditions electropolymerization of phenol was performed on Au/glass electrodes, while the potential was cycled in the range from 0 to 1.2 V vs. Ag/AgCl.

4.8 Preparation of thin iron oxide NP imprinted PDMS composites

In order to prepare PDMS layers by spin-coating, the method of Lee and Voeroes ^[190] was followed. These experiments were performed under ambient conditions using the KL-SCC-200 spin coater (L.O.T.-QuantumDesign GmbH, Darmstadt, Germany), which allows a vacuum hold-down of the substrates during spinning. The base and the curing agent (10 weight parts + 3 weight parts) of the commercial silicon elastomer were thoroughly mixed and dissolved in hexane with a total concentration of 0.5% (w/w).

The study was performed by spin-coating small amounts of PDMS containing different proportions of iron oxide NPs on clean SiO₂ and ITO surfaces. For this purpose, 5, 25, 50 or 100 µL of OA-stabilized Fe₃O₄-NP (5 mg mL⁻¹ in toluene) were dispersed in 500 µl PDMS-hexane solution and sonicated over 3 min. A volume of 500 µl of this mixture was deposited on the supporting surface (2.5 cm × 2.5 cm). This volume is considerably larger than required for the film formation. The sample was initially rotated for 3 sec at a slow rotation rate of 10 rps, then the rotation rate increased to 34 rps for 40 sec and finally slowed down to 10 rpm for 6 sec. The excess liquid was removed by this process. The resulting composites designated as C5/glass, C25/glass, C50/glass, C100/glass were cured at 60-70 °C overnight. For permeability tests of the composites, a conductive support was required. Hence, Fe₃O₄-NP imprinted polymers generated on ITO were used as analogues to the glass surfaces (C5/ITO, C25/ ITO, C50/ ITO, C100/ ITO). Non-imprinted PDMS layers (PDMS/glass and PDMS/ITO) were prepared for control measurements.

4.9 Nanoparticle removal

4.9.1 Electrochemical removal of gold and silver NPs

Linear sweep voltammetry provides an electrochemical detection and quantification scheme of template and analyte NPs. Electrochemical oxidation of AuNPs was performed in an aqueous 3 M KCl solution by scanning the potential linearly from 0 V to maximally 1.4 V at a sweep rate $\nu = 10 \text{ mV s}^{-1}$. This creates voids at places where AuNP were removed electrochemically. These are denoted as $\{\}_{\text{ec}}$. Thus, the polymer films with voids are denoted as $\text{PPh}/\{\}_{\text{ec}}/\text{ITO}_{\text{APTES}}$. The detection of analyte AgNPs in PPh-based matrices after reuptake experiments was performed in the potential range of about 0 V to 0.3 V at a scan rate of 50 mV s^{-1} in aqueous 0.1 M NaNO_3 solution as described in Ref.^[191]. LSV scans were repeated until no further metal oxidation signal was observed.

The charge density for the removal of the template or the detection of the analyte was calculated from the area of the oxidation peak from LSV measurements according to Eq. (20). The calculation considers the baseline as exemplified in Fig. 17.

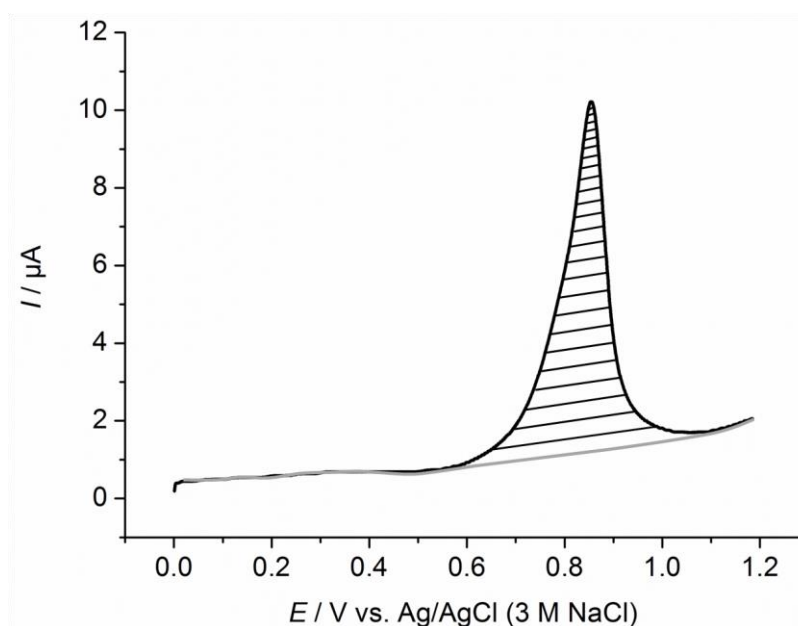


Figure 17. LSV of $\text{AuNP}/\text{ITO}_{\text{APTES}}$ recorded in 3 M KCl with a scan rate of 10 mV s^{-1} upon removal of template AuNPs. The diagonal black stripes represent the integration area of the peak used for calculating the charge. The baseline is marked in grey.

The charge was divided by the exposed area of the coated ITO electrode to obtain the charge density. The electrode area was defined by mounting the NIP-coated ITO electrode as the bottom of a cylindrical cell (Fig. 12) with an exposed area of 0.502 cm².

4.9.2 Chemical removal of gold NPs

Alternatively, AuNPs were removed chemically by treatment in aerated aqueous 6 mM KCN solution for 3 h giving PPh/{ }_c/ITO_{APTES} and PDMS/{ }_c/ITO_{APTES}, { }_c stands for the assumed presence of nanovoids at the places where template AuNPs were removed chemically. After the chemical oxidation of template AuNPs, samples were extensively rinsed with water and dried in a gentle Ar stream. The cyanide concentration was adopted from Ref.^[192], however, the duration of the treatment was determined from the AuNPs/ITO_{APTES} samples and then adapted to samples with a polymer matrix. In order to prove the stability of ITO in KCN etching solution, a clean electrode was treated in the same manner and subsequently tested using a redox active probe.

4.9.3 Chemical removal of iron oxide NPs

The chemical removal of OA-stabilized iron oxide NPs was performed overnight in a aqueous 0.6 M ascorbic acid solution adjusted to pH 3 with HCl, similar to the procedure used by Larsen et al.^[193]. After reductive dissolution of NPs, samples were rinsed with water and dried in a slight Ar stream. ITO samples were used as conductive analogues to the non-conductive glass surfaces in order to permit permeability test before and after template removal.

4.9.4 Magnetical removal of iron oxide NPs

After LB-transfer of the NP layer on TSG, the sample was carefully immersed into a beaker filled with deionized water. A strong magnet was placed in front of the container wall in order to enable the magnetically triggered release of Fe₃O₄-NPs. After 30 min, the sample was pulled out and dried in air and further characterized.

4.10 Reuptake experiments

The recognition ability of PPh-based NIPs was tested by reuptake experiments. These experiments were conducted using two different NP populations including citrate-stabilized AgNPs with a diameter of 20 nm and citrate stabilized AuNPs with a diameter of 50 nm. The uptake solution was prepared from a mixture of 20-nm AgNPs and 50-nm AuNPs with a particle ratio of 1:1. For the uptake of analyte NPs, the NIP-coated electrodes were dipped in a NP solution over 15 h. Afterwards, the samples were carefully rinsed with water in order to remove all physically adsorbed NPs. The presence of analyte NPs was verified by LSV in the same way as used for the release of the template NPs (detailed above). As control samples untreated ITO as well as non-imprinted polymer films were exposed to NP solutions and tested in the same manner afterwards.

4.11 Permeability test

The permeability of polymer films for redox active electrolyte components before and after removal of template NPs was assessed by cyclic voltammetry in aqueous 1.0 mM $[\text{Ru}(\text{NH}_3)_6]\text{Cl}_3$ + 0.1 M KCl by potential cycling in the range from 0.2 V to -0.5 V at a sweep rate of 100 mV s^{-1} . Further points of reference were obtained from permeability tests on bare ITO (before and after KCN treatment), on AuNP/ITO_{APTES} and on blank PPh films on ITO (before and after KCN treatment). The same procedure was also applied in complementary studies on bare Au/glass electrodes as well as after generating a PPh layer on it.

5. One step deposition of composites of polymer matrix and nanoobjects

The following chapter describes “one step” fabrication processes of nanocomposites. Overall, this includes promising techniques, such as spin-coating and two different Langmuir-Blodgett approaches for the formation of NIPs to be used as sensing materials for NPs. In our cooperation with the group of Prof. Dr. Daniel Mandler from the Hebrew University in Israel we published a new concept based on NIPs combined with electrochemical detection in *Angewandte Chemie International Edition*.^[194] The translation of this paper for the German version in *Angewandte Chemie* was prepared by me. The new sensor principle was first demonstrated with a poly(aniline) (PANI) film transferred simultaneously with template AuNPs by the LB technique (Chapter 5.4). My own contribution to this work was the characterization of NIPs by SFM and XPS. Using the LB technique it was additionally possible to publish an expanded scope of matrix fabrication by the formation of monomeric building blocks consisting of OA and OA-stabilized iron oxide nanoparticles (Chapter 5.3).^[195] The entire experimental work was done by me, as well the preparation of the draft, which was checked by the coauthors. However, the chapter starts with the discussion of a NIP-related model, which is synthesized by microelectrospotting and known as a molecularly imprinted polymer for protein-selective recognition (Chapter 5.1). This project was conducted in cooperation with the group of Prof. Dr. Frieder Scheller from the Fraunhofer Institute IZI-BB in Potsdam, Germany. My contribution was the characterization of the materials by SFM. The work lead to a joint publication.^[196]

5.1 Deposition and selective dissolution of protein-polymer composites

Microelectrospotting was introduced by Scheller’s group as a new approach for the preparation of protein-selective MIP microarrays on bare gold SPR imaging chips.^[196] Different from NIPs, MIPs usually consist of a 3D polymer net-work structure and are formed in the presence of a template (imprinted) molecule. However, in this research,

MIPs were prepared as thin film coatings with a thickness similar to the size of the used template. Thus their architecture is similar to that of NIPs. For the preparation of MIPs the spotting pin encloses a monomer-protein mixture that upon contacting the gold surface is in situ electropolymerized resulting in an electrically insulating surface-imprinted film. These polymer films were made with scopoletin as the monomer and ferritin as a large protein template. Scopoletin was chosen as a monomer because the film thickness can be controlled with ca. 1 nm precision,^[197] which is necessary in order to incorporate as much of the template as possible without irreversibly entrapping it. Proteins as large template molecules are rich in functionalities and are expected to provide MIP with higher binding affinities than those obtained by imprinting small molecular weight compounds. The removal and rebinding experiments of ferritin were controlled in a label-free manner by SPR imaging. Treating electrosprayed polymer films with 5 mM NaOH resulted in the removal of the template molecules from the film due to hydrolysis. This was detected as a decrease of the SPR signal. When rebinding experiments were performed at higher ionic strengths established by adding NaCl to the 4-(2-hydroxyethyl)-1-piperazineethanesulfonic acid (HEPES) buffer, a pronounced increase in the SPR signal was observed, corresponding to the binding of ferritin target molecules to the MIP. The shielding effect of NaCl describes the attraction between the negatively charged poly(scopoletin) matrix and ferritin template. The highest ratio of ferritin bound on the MIP versus the non-imprinted polymer film was obtained at 300 mM NaCl concentration while the suppression of the electrostatic repulsion was found by SPR measurements to be already sufficient at 150 mM NaCl. As a control, non-imprinted polymer films were prepared under the same conditions as the ferritin-MIPs but without ferritin in the monomer solution. Applying the procedures of removal and rebinding to non-imprinted polymer films show negligible effects during SPR imaging, which confirmed the reuptake ability of MIPs.

For SFM measurements the MIP was deposited on flat gold disk electrodes using the same pulse regime as for their preparation on SPR chips. The MIPs were incubated in 5 mM NaOH for 20 min to remove the template. Rebinding of the target was performed by incubating the MIP-covered electrode in 10 mM HEPES (pH 7.4) containing 150 mM NaCl and 500 nM ferritin for 30 min. Figure 18 shows SFM images of non-imprinted poly(scopoletin) as well as ferritin-imprinted poly(scopoletin) right after preparation, and

after removal and rebinding of the ferritin template. The morphology seen for the non-imprinted polymer (Fig. 18a) is that of the underlying polycrystalline Au substrate on which electropolymerization of scopoletin forms a conformal film of 6 nm thickness (Table 7).

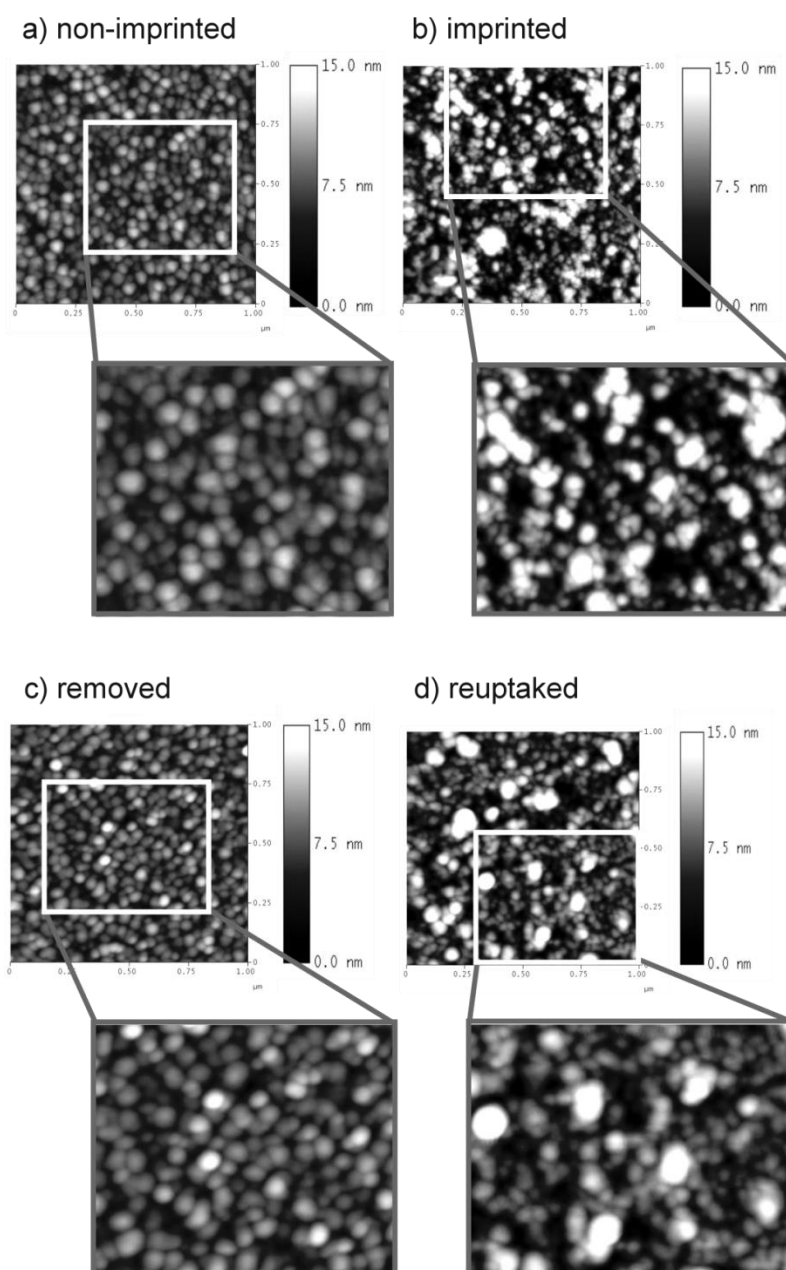


Figure 18. SFM topography images (scan area: 1 $\mu\text{m} \times 1 \mu\text{m}$ + enlarged subsection) recorded in intermittent mode with a resolution of 256 \times 256 pixels of a) non-imprinted poly(scopoletin), b) poly(scopoletin) imprinted with ferritin, c) ferritin-imprinted poly(scopoletin) after removal of ferritin by 5 mM NaOH for 20 min; d) sample c) after template-rebinding from a 500 nM ferritin solution for 30 min using a NCHV-A SFM tip ($k = 42 \text{ N m}^{-1}$).

Table 7. Film thickness (Appendix, Fig. A1), roughness values (RMS, determined for $1 \mu\text{m} \times 1 \mu\text{m}$) and height (Appendix, Fig. A2) of typical structures for different poly(scopoletin) films. The relevant SFM measurements are provided in the Appendix of this thesis (Appendix, Fig. A1, 2).

Sample	Thickness [nm]	RMS Roughness [nm]	Object heights [nm]
a) non-imprinted poly(scopoletin)	6.0	1.63	5.6, 3.6, 4.3
b) ferritin-imprinted poly(scopoletin) (MIP)	18.1	3.88	13.7, 15.4, 8.7
c) sample b) after removal of ferritin	9.3	1.78	7.5, 3.6, 5.5
d) sample c) after reuptake of ferritin	9.7	3.52	11.9, 16.8, 9.8

If the poly(scopoletin) film is prepared in presence of ferritin, a completely different film morphology is obtained (Fig. 18b). Elevated structures are clearly visible in the SFM image and the representative objects have dimensions similar to ferritin (Table 7). The layer thickness is about 12 nm higher than that of the non-imprinted polymer layer. Given the experimentally determined hydrodynamic radius of 8.7 nm for ferritin, this suggests that only a part of the ferritin molecule is embedded in the polymer layer. This tentative assignment of the elevated structures to ferritin molecules (or clusters of them) is confirmed by the SFM image after removal of ferritin in 5 mM NaOH for 20 min which leads to a film morphology that is similar to that of the non-imprinted film (Fig. 18c). Also the film thickness (Table 7) decreases substantially indicating that ferritin molecules are only partially embedded in the poly(scopoletin) matrix and as such can be released into the solution. Some depressions are visible and might originate from shallow voids in the film. Given the convolution of surface morphology with the SFM tip shape, this assignment cannot be further substantiated. After exposure of the sample to a 500 nM ferritin solution for 30 min, a surface morphology similar to the original MIP is observed (Fig. 18d), although the average film thickness increases only slightly (Table 7). However, the sizes of representative objects is again in the range of ferritin molecules (Table 7). The number of elevated objects seems to be smaller than in Fig. 18b which explains the lower average film thickness in comparison to the original MIP. The observed lower ferritin rebinding is reasonable because at 500 nM solution concentration during the reuptake only half of the saturation is reached as confirmed by SPR measurements.^[196] Therefore, it is unlikely that each binding site is reoccupied.

From SPR imaging it was not possible to distinguish between target proteins inside the remaining cavities of the matrix or protein molecules on the top of the film. However, it was clearly shown that shielding of charges has an important impact on the reuptake efficiency of MIPs. When binding experiments were performed at a higher ionic strength (established by adding NaCl to the HEPES buffer) the electrostatic repulsion between the protein and the poly(scopoletin) layer decreases. This was confirmed by a pronounced increase of the SPR signal until reaching the steady state. On the contrary, binding of ferritin was not observed in pH 7.4 HEPES buffer due to a negligible SPR signal change associated with high electrostatic repulsion at low ionic strength. This result can be directly transferred to NIP-systems, because shielding of surface charges can change interaction between analyte NPs and the polymer matrix in a controlled way. Furthermore, it was evident, that with the change of the pH, proteins can be easily manipulated and removed by hydrolysis and washing procedures. This knowledge can be useful if NIPs are formed of protein-coated or polymeric NPs.

Furthermore, imaging of small cavities (~ 8.7 nm) via SFM turns out to be rather difficult due to the appearance of convolution effects (Chapter 2.1.1). In spite of that, changes in the topography could be detected by obtaining the RMS surface roughness (Table 7). However, if these values are to be meaningful, reference measurements are required which provide reproducible information about the individual surface characteristics. These are time-consuming experiments and a reason why SFM is not recommended as routine method for detection of cavities.

5.2 Spin coating of composites of iron oxide NPs and PDMS

The initial approach for NIP fabrication is focused on the generation of a PDMS-matrix imprinted by OA-stabilized Fe₃O₄-NPs with a mean diameter of 10 nm (details of chemicals can be found in Chapter 4.8). Spin coating was used to form thin layers from a mixture of NPs and PDMS on flat glass and ITO substrates. A small amount of coating material is applied on the substrate, which is subsequently rotated at an appropriate speed in order to spread the coating material by centrifugal force until the desired thickness of the film is achieved. The applied solvent is usually volatile, and simultaneously

evaporates.^[198] The thickness depends on several factors like spinning speed and the duration, viscosity and concentration of both solution and solvent as well as on the ambient temperature or the substrate temperature.^[199, 200]

Poly(dimethylsiloxane) is a commonly used silicon-based organic polymer. Due to its flexibility, optical transparency and bio-compatibility, it has become a preferred choice for components of microfluidic devices,^[201-203] membrane devices^[204] and optical waveguides.^[205] In many of these applications spin-coating enables the formation of thin PDMS films, which was one deciding point to use the elastomer for NIP fabrication. The major intention was to achieve a good distribution of Fe₃O₄-NP inside a PDMS-matrix which has at best a thickness less than the diameter of the NP template (< 10 nm, Fig. 19a). In this manner, the particles remain accessible to the ascorbic acid solution used for chemical removal of the templates. After removal (Fig. 19b), the cavities are meant to provide a sufficient area to interact with analyte particles.

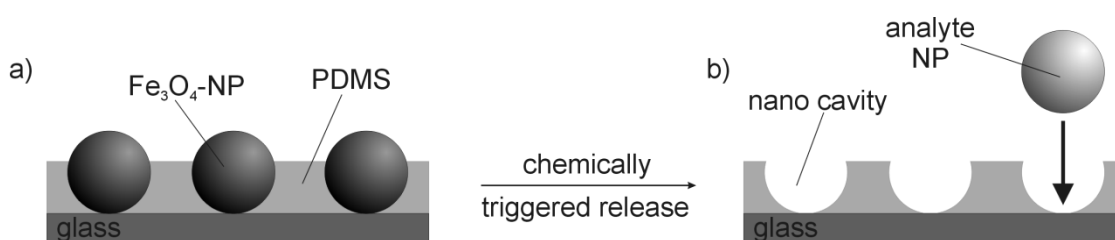


Figure 19. Schematic representation of a) the 2D composite consisting of Fe₃O₄-NPs and PDMS, and b) the remaining PDMS matrix after chemically triggered release of the Fe₃O₄-NPs.

The study was performed by spin-coating small amounts of PDMS (prepared in hexane, see section 4.8) containing different proportions of iron oxide NPs on SiO₂ and ITO surfaces. The samples were named depending on the amount of NPs added to the spin-coating solution and the nature of the substrate (C5, C25, C50, C100/substrate, C = composite, number = particle amount in μ l, substrate = glass, ITO). SFM investigations of non-imprinted PDMS-layers on glass revealed a smooth surface morphology (RMS = 1.84 nm for PDMS/glass) and a layer thickness that varied depending on the prepared sample batch between 7-12 nm (Fig. 20a). This is in disagreement with ellipsometric thickness measurements made by Lee and Voeroes^[190] of PDMS-films (~30 nm) prepared using similar conditions.

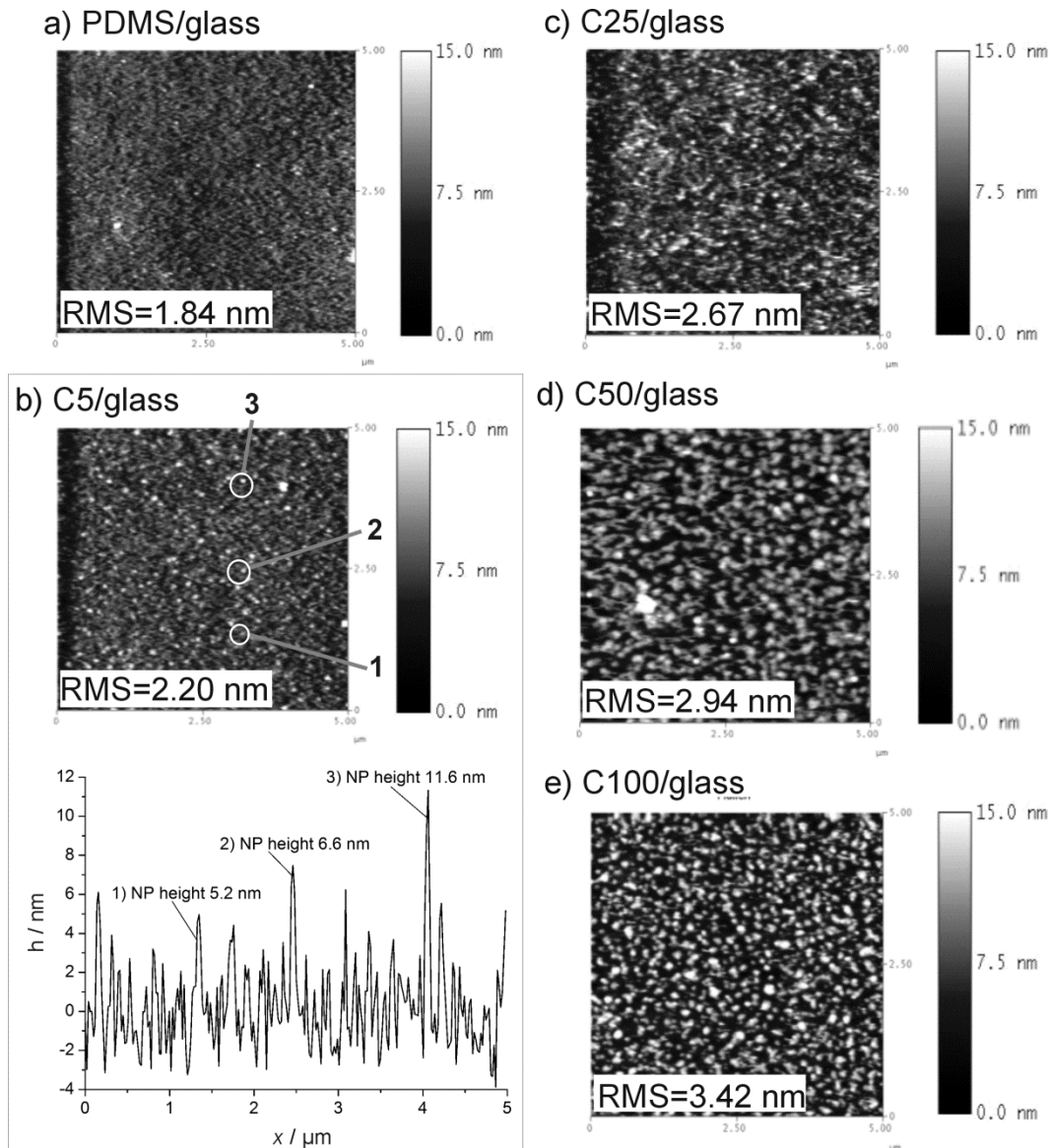


Figure 20. SFM topography images recorded in the contact mode with a MSCT SFM tip ($k = 0.6 \text{ N m}^{-1}$) at a scan rate of 2.0-3.0 Hz with 256×256 pixels (scan area: $5 \mu\text{m} \times 5 \mu\text{m}$). The surface roughness (or aggregate formation) increases concomitantly to the amount of particles within a PDMS film: a) PDMS/glass, b) C5/glass (+ extracted cross section where NP 1 protrudes the polymer film by 5.2 nm, NP 2 by 6.6 nm and NP 3 identifies a NP with 11.6 nm located on the top of matrix), c) C25/glass, d) C50/glass, e) C100/glass.

The difference in film thickness may be related to the method used for its determination, but might also be affected by even the smallest change in the conditions (total concentration, ratio of base and curing agent, ambient temperature). To exclude, or at least reduce, concentration and ambient temperature effects, experiments were usually

conducted within one sample batch prepared from one PDMS-solution during a short time of ~1-2 h. In the presence of Fe₃O₄-templates, thinner layers of about 5-8 nm were achieved. This thickness change can be attributed to a reduced viscosity of the polymer-solution which might be caused by free OA-ligands originating from the NP solution. Figure 20b shows the SFM topography image of a C5-composite surface. This represents an appropriate final NP concentration as the particles (diameter ~10 nm) are well distributed and embedded at different depths into the PDMS matrix. The corresponding cross section is represented below, where NP 1 protrudes the polymer film by 5.2 nm, NP 2 by 6.6 nm and NP 3 identifies a NP with 11.6 nm located on the top of matrix. Occasionally, some aggregation is noticeable along the scan lines. Increasing particle concentration favors the formation of aggregates (monitored using SFM, Fig. 20c-e for C50/glass and C100/glass). This is probably caused by an overload of the polymer film with magnetic iron oxide particles, which in addition strongly attract each other.

UV-vis spectra of template NPs within a PDMS matrix show an enhancement in the absorption upon an increase in particle amount (Fig. 21, curves 1-4). The spectral profiles depicted in Fig. 21 are similar to investigations of Fe₃O₄ nanocrystals dispersed in hexane and in LB-multilayer assemblies as conducted by Zhang et al.^[206].

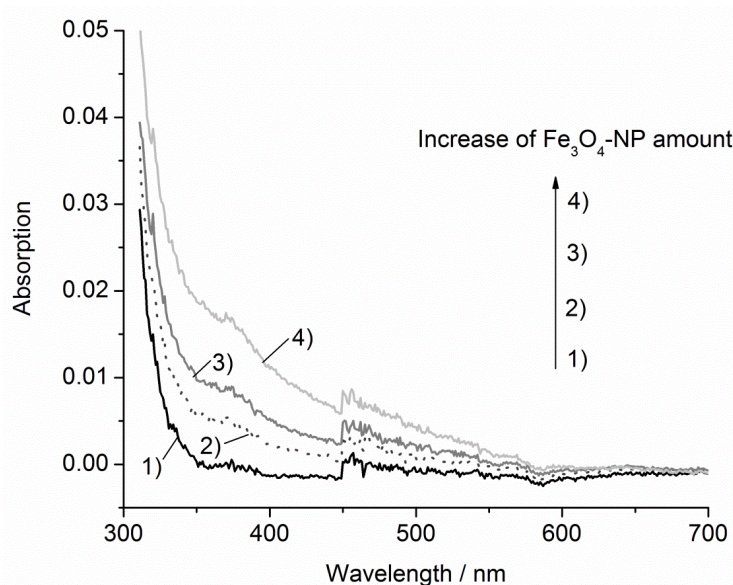


Figure 21. UV-Vis observations of Fe_3O_4 -NPs imprinted PDMS-matrices showing a continuous increase in absorption caused by an increase of template concentration: 1) C5/glass, 2) C25/glass, 3) C50/glass and 4) C100/glass. The discontinuity at 450 nm is an artefact which corresponds to an instrumental artifact due to the change between the deuterium and halogen lamps of the SPEKOL 2000 spectrometer.

In order to enable electrochemical investigations of the NIPs, a conductive support was required. Hence, non-imprinted and Fe_3O_4 -NP-imprinted PDMS layers generated on ITO were used as analogues to the glass surfaces. Cyclic voltammetry measurements of the redoxactive probe $[\text{Ru}(\text{NH}_3)_6]^{3+}$ were performed to assess the permeability of PDMS-based layers. Figure 22a shows the CVs of bare ITO, PDMS/ITO, C5/ITO, C25/ITO, C50/ITO and C100/ITO in 1.0 mM $[\text{Ru}(\text{NH}_3)_6]\text{Cl}_3 + 0.1 \text{ M KCl}$. The response on bare ITO shows a well-developed quasi-reversible CV for $[\text{Ru}(\text{NH}_3)_6]^{3+/2+}$ (Fig. 22a, dashed curve). The CV after spin-coating a non-imprinted PDMS-film on the ITO surface is typical for a blocking layer that permits small residual currents only (Fig. 22a, black curve for PDMS/ITO). A slight increase in the anodic current response is observed with the increase of particle concentration (Fig. 22b, enlarged scale of CVs at PDMS/ITO in comparison to C5/ITO, C25/ITO, C50/ITO and C100/ITO), which might have two different reasons. Firstly, magnetite (Fe_3O_4) is one of the preferred well known filler materials, which can enhance the effective electrical conductivity in organic polymers/nanocomposites.^[207, 208] Semiconducting properties of Fe_3O_4 are related to its cubic inverse spinel structure with fcc close packed oxygen anions and Fe cations

occupying the interstitial A and B sites.^[209] While A sites are tetrahedrally coordinated to oxygen and occupied only by Fe^{3+} ions, B sites are octahedrally coordinated to oxygen and occupied by an equal number of Fe^{2+} and Fe^{3+} ions as represented with the formula: $(\text{Fe}_8^{3+})_A[\text{Fe}_{40/3}^{3+} \text{Fe}_{8/3}]_B\text{O}_{32}$. Electron hopping between mixed valences of Fe ions in the octahedral sites is responsible for relatively high electric conductivity of Fe_3O_4 above $T_v \approx 125$ K, the point of Verwey order-disorder phase transition,^[210] rendering magnetite an important class of half-metallic materials.^[211]

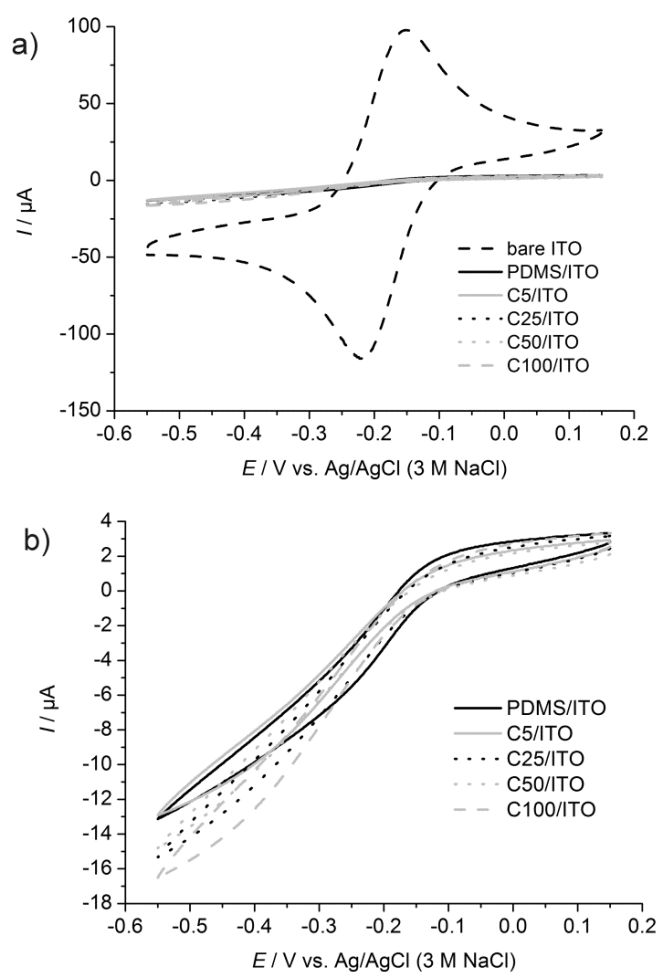


Figure 22. CVs recorded in 1 mM $[\text{Ru}(\text{NH}_3)_6]\text{Cl}_3 + 0.1$ M KCl at a scan rate of 0.1 V s^{-1} at a) bare ITO, C5/ITO, C25/ITO, C50/ITO, C100/ITO and b) the enlarged scale of CVs at PDMS/ITO, C5/ITO, C25/ITO, C50/ITO, C100/ITO.

The second reason for the slight increase in the anodic current response of $[\text{Ru}(\text{NH}_3)_6]^{3+/2+}$ might be associated with the loss in stability and cross-linked density of PDMS composites with addition of OA-stabilized iron oxide NPs. An indication of that

issue is given by force-distance curves recorded during SFM-imaging in contact mode (Fig. 23).

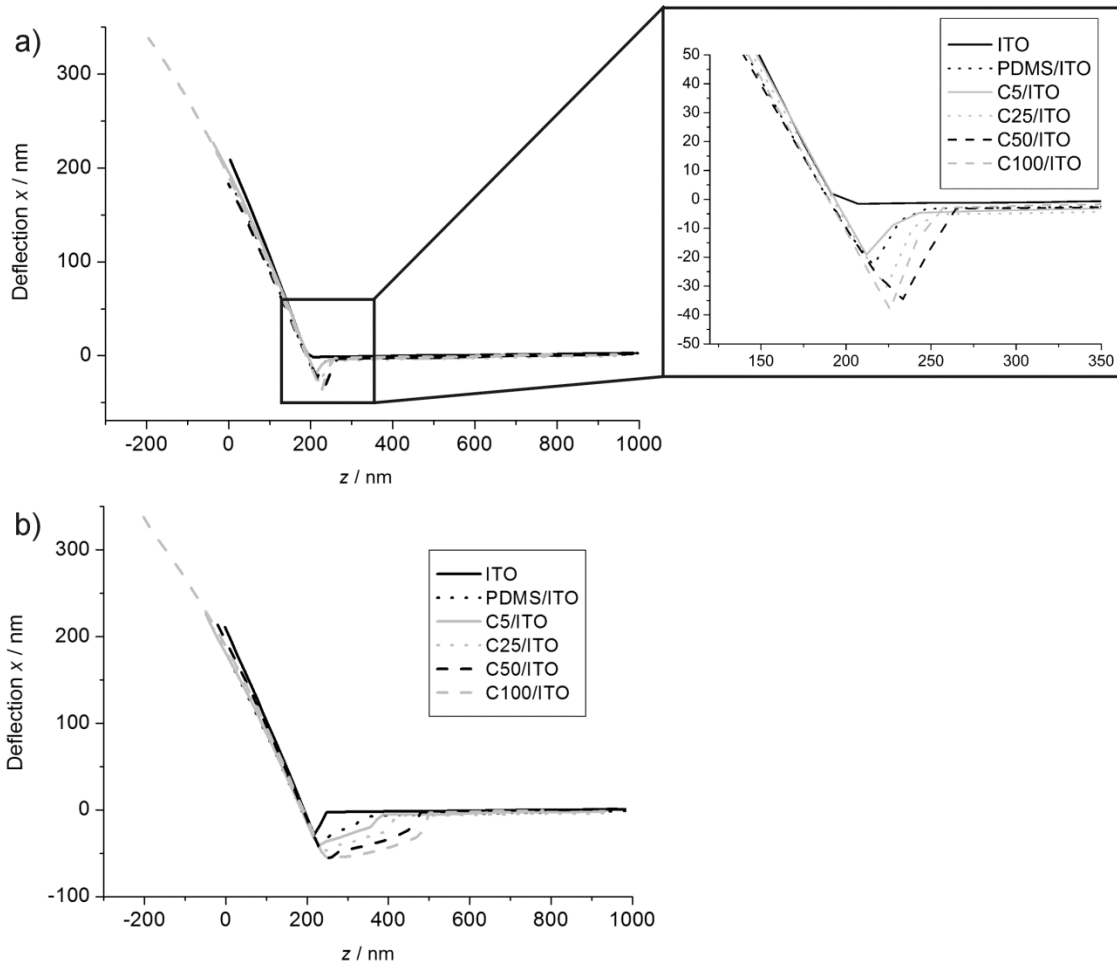


Figure 23. Force-distance plots measured with a MSCT SFM tip ($k = 0.6 \text{ N m}^{-1}$) during imaging in contact mode representing in a) the approach (+ enlarged view) and in b) the retraction of the cantilever on bare ITO, PDMS/ITO, C5/ITO, C25/ITO, C50/ITO and C100/ITO.

The force plot obtained at PDMS/ITO (Fig. 23a, dotted black curve) shows an extended area of negative tip deflection after the SFM tip has jumped in contact indicating attractive forces, which are different to force-distance curves measured on bare ITO where no snap-in is observed due to repulsive interaction between the tip and ITO (Fig. 23a, black curve). The attractive force increases with the amount of OA-stabilized Fe_3O_4 -NPs, and is most likely caused by the formation of a capillary meniscus as the tip approaches the sample surface and penetrates into the polymeric matrix. A continuous pull out during retracting of the SFM tip indicate capillary adhesion between the SFM tip and the PDMS surface as well, whereas an abrupt pull-off is observed at bare ITO (Fig.

23b). In general, any surface exposed to ambient conditions show a strong adhesion force induced by adsorbed water molecules at the interface of the tip and the sample.^[212] As the surface of PDMS is inherently hydrophobic, meaning that water cannot easily penetrate its surface, the capillary adhesion might involve polymer-melt forces rather than condensed water. Butt and coworkers^[213, 214] showed that such attractive force occurs in short-chain PDMS polymer melts with a low molecular weight when the SFM tip approaches the sample and polymer segments are able to move out of the closing gap and equilibrate with the bulk reservoir. Long-chain PDMS melts with a high molecular weight are more entangled and form an immobilized layer, in which individual chains are prevented from leaving the closing gap and thus creating a repulsive force on the tip. The forces measured on PDMS-coated samples show a greater range of interaction than dried ITO samples due to the presence of a liquid-like polymer layer. An incomplete polymerization creates a lack of stability and makes composites more susceptible to tip penetration. Material abrasion was often observed during imaging when using a truncated SFM tip as the magnitude of adhesive forces increases with the radius of the tip apex.^[215] A large penetration depth may also induce artifacts to height measurements, which might explain the variation in composite thickness measured by SFM.

Equal to PDMS-based films prepared on glass substrates, the SFM images recorded of spin-coated polymer layers at bare ITO show a continuous and smooth topography with thicknesses varying between 5.9-18.1 nm. Figure 24 shows the surface structure of a 17.2 nm thick PDMS-layer (Fig. 24a), while at less than 10 nm thickness (Fig. 24b) the ITO surface structure is noticeable to some extent. Due to the rough structure of ITO (RMS = 3.2 nm) compared to the glass surface (RMS = 1.46 nm), it was impossible to distinguish clearly between template NPs and the polymeric matrix (Fig. 24c, SFM-images of the C25/ITO surface and the corresponding cross section).

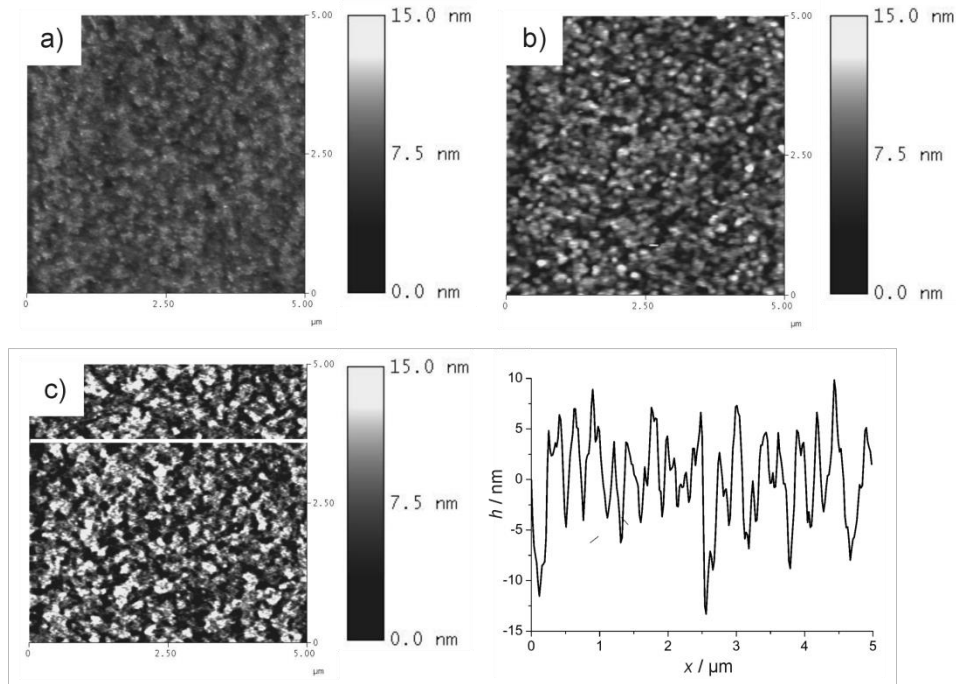


Figure 24. SFM topography images recorded in contact mode using a MSCT SFM tip ($k = 0.6 \text{ N m}^{-1}$) at a scan rate of 2 Hz with 256×256 pixels (scan area: $5 \mu\text{m} \times 5 \mu\text{m}$), showing the topography of PDMS-films (PDMS/ITO) with a thickness of a) 17.2 nm and b) 8.6 nm and of the c) C5/ITO composite surface (+ extracted cross section).

However, from SFM investigations of composites prepared on glass substrates it was obvious that the C5-composite (Fig. 20b) most closely matches the schematic representation of the desired NIP architecture (Fig. 19, left). Furthermore, force measurements by SFM indicate that a less stable matrix is formed upon an increase of NP concentration. Thus, the chemically triggered release of templates was conducted with C5/glass and C5/ITO samples. In order to release Fe_3O_4 -NPs by a reductive dissolution, the samples were treated for 24 h in an aqueous 0.6 M ascorbic acid solution adjusted to pH 3 with HCl. Fe_3O_4 is a mixed oxide that can be considered stoichiometrically as a “mixture” of Fe_2O_3 and FeO. It reacts with HCl as follows:



In order to determine the concentration of released iron ions, ascorbic acid ($\text{C}_6\text{H}_8\text{O}_6$) is employed as a reducing agent for Fe^{3+} . This reaction has been studied in detail by Larsen et al.^[193] and Echigo et al.^[216]. For determination of Fe^{2+} the fluorescent iron-binding dye ferrozine can be used, which forms a red-colored ferrozine-iron-complex selectively.^[217]

In this assay the concentration of released iron was too low to be verified in that manner. The iron concentration that is expected if all imprinted NPs had been resolved was estimated from the volume ($V_{\text{Fe}_3\text{O}_4} = 1.6 \times 10^{-19} \text{ cm}^3$) and density ($\rho_{\text{Fe}_3\text{O}_4} = 5 \text{ g cm}^{-3}$) of one NP (average diameter: $r_{\text{NP}} = 5 \text{ nm}$, molar mass: $M_{\text{Fe}_3\text{O}_4} = 231.5 \text{ g mol}^{-1}$) according to the calculations in (21-23). The total number of NPs ($\Gamma_{\text{NP}} = 4.0 \times 10^9 \text{ cm}^{-2}$) inside the PDMS matrix was determined from counting NP densities in SFM images (Fig. 20b, C5/glass). Based on this approximation, the iron concentration would be about $0.003 \text{ }\mu\text{M}$, which cannot be detected using the colorimetric method as the detection limit of this technique requires a least an iron concentration of $0.4 \text{ }\mu\text{M}$.^[218] However, a control experiment with a highly concentrated NP solution yielded a solution of 0.6 M in dissolved iron species and showed the formation of a redly fluorescent ferrozine-iron complex.

Subsequent UV-vis measurements of the imprinted PDMS films did not show changes of absorption intensities and hence did not allow a detection of removal, most likely because only a small fraction of the template was actually removed. Pulsed-force microscopy images confirmed that many templates were still located within the PDMS matrix, but allow the detection of some remaining nano cavities (Fig. 25). The section analysis reveals depth profiles of 6.4 nm and less (Fig. 25, corresponding cross section), which is approximately the size of the used NPs. Despite this successful example, the detection of NP templates as well as remaining cavities by SFM was a challenging task. From SFM images it was difficult to distinguish between small particles/cavities ($\sim 10 \text{ nm}$) and background features of the polymer. Likewise, high resolution SEM images of NIPs remained unsuccessful because the blocking properties of the composites cause charge accumulations during measurements.

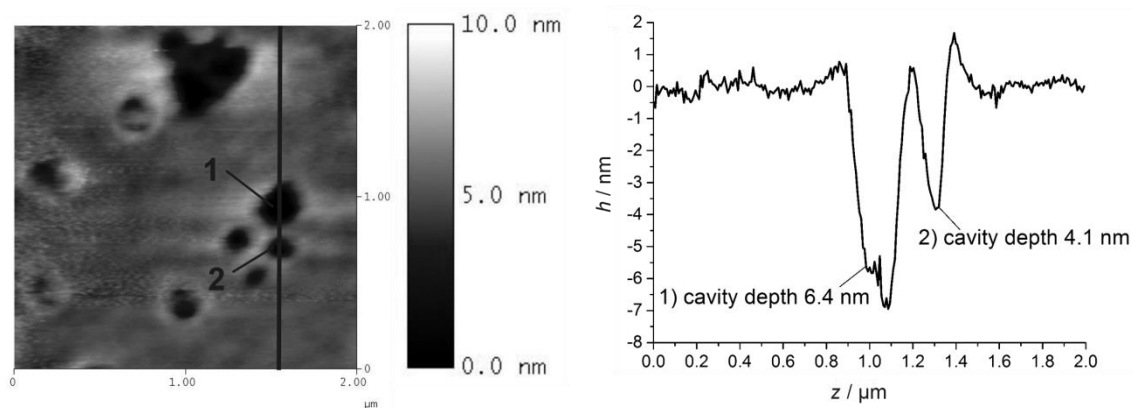


Figure 25. SFM topography images (scan area: $5 \mu\text{m} \times 5 \mu\text{m}$) recorded in pulsed-force using a NFESPA SFM tip (3 N m^{-1}) at a scan rate of 0.5 Hz (256×256 pixels) of composites after removal of Fe_3O_4 -NPs in ascorbic acid and the corresponding cross section.

Better insight was possible by monitoring changes in the electrode response of $[\text{Ru}(\text{NH}_3)_6]^{2+/3+}$ as redox probe before and after the template removal. Cyclic voltammograms obtained after template removal show an increase in the anodic current response (Fig. 26a, grey curve). This requires the NP template to be within nanometer distance to the supporting surface in order to assure that a templated void traverses through the entire PDMS film. These cavities can be considered as randomly arranged microelectrodes (RAM).^[219] Based on the steady-state diffusion-limited current, it is possible to estimate the number of open cavities at the electrode surface.

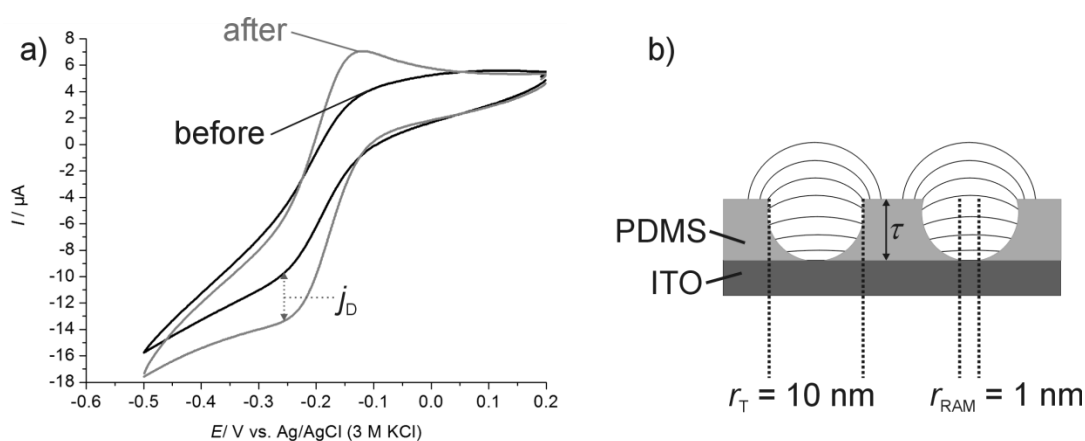


Figure 26. a) CVs recorded at C5/ITO in 1 mM $[\text{Ru}(\text{NH}_3)_6]\text{Cl}_3 + 0.1 \text{ M KCl}$ at a scan rate of 0.1 V s^{-1} show the permeability before (black curve) and after (grey curve) template removal, b) schematic illustration of the PDMS-matrix after template removal, in which remaining nanovoids are considered as randomly arranged microelectrodes.

Equation (17) gives the total current density of an array of recessed nanoelectrodes, where $n_z = 1$ is the number of transferred electrons, $D = 9.1 \cdot 10^{-6} \text{ cm}^2 \text{ s}^{-1}$ is the diffusion coefficient^[220] and $c^* = 1.0 \cdot 10^{-6} \text{ mol cm}^{-3}$ the concentration of $[\text{Ru}(\text{NH}_3)_6]^{2+/3+}$. The number of NPs Γ_{NP} was determined from counting NP densities in SFM images. However, this value might be very imprecise, due to the low resolution of microscopic images. Given the film thickness τ from SFM experiments (Appendix, Fig. C1) and the estimation of the active area of an individual inlaid nanoelectrode $r_{\text{RAM}} = 1.0 \cdot 10^{-7} \text{ cm}$, it is possible to estimate the diffusion limited steady-state current that is expected if all NPs had been resolved and would leave an electrochemically active nanovoid imprinted into the film.

$$\begin{aligned}
 j_{\text{RAM,expected}} &= \Gamma_{\text{NP}} \cdot \frac{1}{\chi} 4n_z F D c^* r_{\text{RAM}} \\
 &= 4.0 \cdot 10^9 \text{ cm}^{-2} \cdot \frac{1}{\chi} \cdot 4 \cdot 1 \cdot 96485 \text{ As mol}^{-2} \cdot 9.1 \cdot 10^{-6} \text{ cm}^2 \text{ s}^{-1} \cdot \\
 &\quad 1.0 \cdot 10^{-6} \text{ mol cm}^{-3} \cdot 1.0 \cdot 10^{-7} \text{ cm} \\
 &= \frac{1.4 \cdot 10^{-3}}{\chi} \text{ A cm}^{-2}
 \end{aligned} \tag{17}$$

The ratio χ between the diffusion-limited currents at an inlaid nanoelectrode i_d and a recessed nanoelectrode i_{RAM} of the same radius is given by Eq. (18).^[219]

$$\begin{aligned}
 \chi &= 1 + \frac{4\tau}{\pi \cdot r_{\text{RAM}}} = \frac{i_D}{i_{\text{RAM}}} \\
 &= 1 + \frac{4 \cdot 8 \cdot 10^{-7} \text{ cm}}{\pi \cdot 1 \cdot 10^{-7} \text{ cm}} = 11.2
 \end{aligned} \tag{18}$$

$$A = \frac{j_D}{j_{\text{RAM,expected}}/\chi} \cdot 100\% = \frac{7.2 \cdot 10^{-5} \text{ A cm}^{-2}}{1.3 \cdot 10^{-4} \text{ A cm}^{-2}} \cdot 100\% = 57\% \tag{19}$$

Due to the spherical shape of the template, the active area ($r_{\text{RAM}} = 1 \text{ nm}$) is supposed to be much smaller than the real diameter ($r_{\text{RAM}} = 10 \text{ nm}$) of one NP (Fig. 26b). This expected current $j_{\text{RAM,expected}}$ is compared to the experimentally measured current j_D (Fig. 8a). Under this assumption about 57 % of the cavities are open and behave like recessed nanoelectrodes (Eq. 19). This calculation is considerably simplified, but it gives the order

of magnitude and confirms either an incomplete removal of templates (Fig. 27b, 1) or indicates that there is only in exceptional cases a direct contact between the template and the sample surface (Fig. 27b, processes 2 and 3).

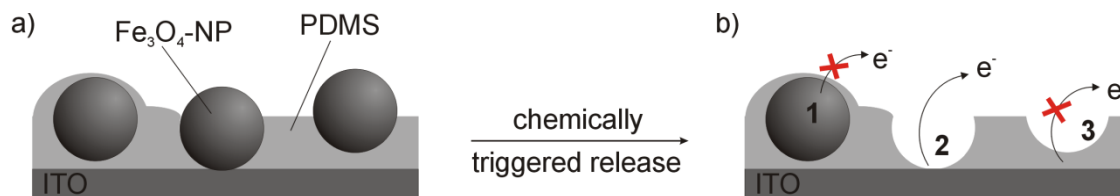


Figure 27. Schematic illustration of a Fe_3O_4 -NP thin film PDMS composite a) before and b) after template removal. Part b) shows (1) a non-dissolved NP covered by a thin PDMS layer, (2) a formed cavity where the template was in a direct contact with the electrode surface and (3) the template was separated from the surface by a thin PDMS film.

In this study, the spin-coating technique provides the formation of Fe_3O_4 -NP thin film composites. To the best of my knowledge, this is the thinnest PDMS layer so far constructed and characterized by spin-coating. However, PDMS hardly offers any possibilities to introduce specific interactions for NPs. Furthermore, there was no suitable characterization method available to detect analyte NPs in the film. Therefore, no reuptake studies have been undertaken and this particular system was not further considered. As an attractive alternative to PDMS, poly(ethylenimine) offers the opportunity to introduce certain chemical groups capable of forming selective polymer-mediated interactions.^[221-223] However, it needs to be characterized in terms of the layer thickness or morphology before it can be classified as suitable for the preparation of NIPs.

5.3 System with iron oxide nanoparticles and oleic acid

In the next approach the scope of matrix fabrication was expanded by the use of monomeric building blocks, namely OA and OA-stabilized iron oxide nanoparticles (Fe_3O_4 -NPs) with an average diameter of 10 nm. Oleic acid is a monounsaturated fatty acid that is the most widely distributed and abundant fatty acid found in nature.^[224] For the formation of 2D nanocomposites, the NPs and the OA molecules were arranged as a monolayer at the air-water interface and then transferred to a TSG electrode by LB

transfer. Oleic acid works as a diluent in between the NP templates with an average diameter of ~ 10 nm. Their release was triggered by an external magnetic field instead of chemical dissolution in Chapter 4.9.4. In contrast to chemical dissolution, magnetic release leaves the NP intact so that it can be used for a controlled transfer of NPs. As Fe_3O_4 -NPs are increasingly used in catalysis^[225] and bio-applications including various labeling and separation techniques,^[226] drug delivery systems and magnetic resonance imaging,^[227] there is an increasing need to manipulate them by external triggers. This may be used for controlling their mobility and eventually their position, for instance, for target specific locations in vivo or to detect NPs in assays selectively based on their size, shell and core material.

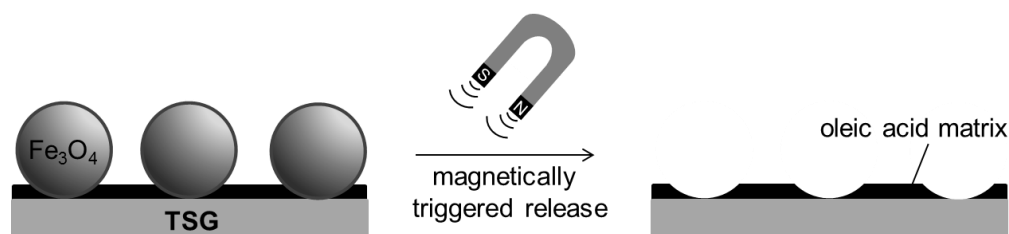


Figure 28. Schematic representation of the 2D composite consisting of Fe_3O_4 -NP and a LB-monolayer of oleic acid (left) and the magnetically triggered release of the Fe_3O_4 -NP (right).

An appealing approach for making a monolayer film of NPs is the LB technique, in which nanoobjects can be incorporated into monolayers made of amphiphiles.^[228-230] Figure 29, curve 1 shows the Langmuir isotherm during the compression of a mixture of OA and Fe_3O_4 -NPs. The isotherm for pure OA is given for comparison in Fig. 29, curve 2. The isotherm of the mixture was obtained after several optimization rounds. It shows a collapse pressure of 32 mN m^{-1} and produces continuous curves with a large plateau region at small molecular areas. In contrast, isotherms of pure OA molecules show a steeper slope and the collapse of the monolayer at $27\text{-}30 \text{ mN m}^{-1}$. Emphasis was put on the aim to record LB isotherms showing the gas-like phase as well as the collapse point of the monolayer. This requires careful optimization. Due to the brush-like shape of the used NPs the area per molecule can be compressed so far until the barriers are at the limit, without reaching a collapse. If the amount of NPs is increased, the isotherm does not start from the zero line, but achieve the point of collapse.

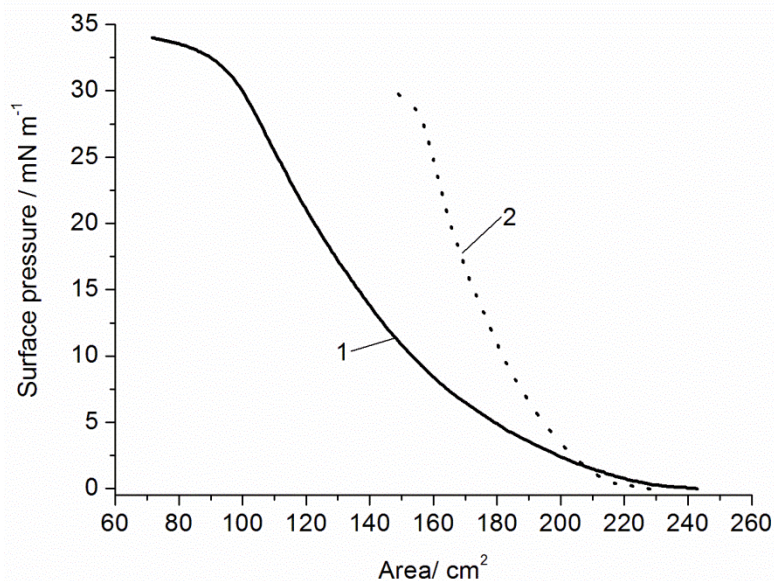


Figure 29. Langmuir isotherm of (1) a mixture of Fe_3O_4 -NPs and OA and of (2) pure OA recorded with 10 mm min^{-1} .

Initial attempts to use lower volumes of the same or higher concentrated NP stock solution (without addition of pure OA) did not give reproducible results, presumably because the Fe_3O_4 -NPs already agglomerated during application of the stock solution to the air-water interface. This became evident by irreproducible collapse pressures well below the collapse pressure of an OA monolayer of 27 to 30 mN m^{-1} ^[143, 231] in Fig. 29, curve 2. In addition, after an initial closing and opening of the barriers of the LB trough, further compressions showed a much steeper rise of surface pressure and a much larger extended region of gas-like behavior most likely because the 2D aggregates of Fe_3O_4 -NP formed during the first compression did not disperse during the re-opening of the barriers. The isotherms in Fig. 29 were not normalized to the area per molecule since this quantity is not reasonable for a mixture of NP and OA. In addition, the Fe_3O_4 -NP preparation did contain an unspecified excess of unbound OA. The optimized mixture of OA and Fe_3O_4 -NPs allowed reproducible LB transfers at 25 mN m^{-1} .

The arrangement of the NPs within the matrix and their triggered release was characterized by SFM and PM IRRAS. The PM IRRAS spectrum obtained for the LB-layer in Fig. 30 shows the absorption bands of the symmetric and asymmetric CH_3 - and CH_2 -stretching vibrations of OA (for assignment of vibrations, see Tab. 8). The unsaturated groups of oleic acid are potentially important as polymerizable groups. On

the other hand, the double bond introduces disordering of the hydrocarbon chains.^[143] The weak band at 3005 cm^{-1} of the C-H stretching vibration in C=C-H cis-double bond was not observed in the LB films (Fig. 30a). This is most likely due to a low surface concentration of oleic acid molecules and the unfavorable orientation of the bond with respect to the surface normal. The vibration was observed as a weak signal in isotropically arranged films of OA obtained by drop-casting OA on a TSG substrate (Fig. 30b).

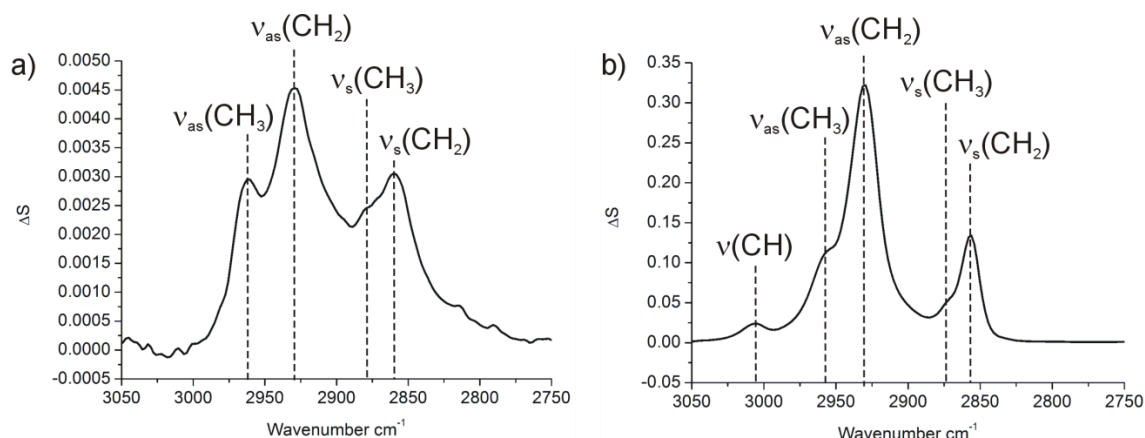


Figure 30. PM IRRA spectra in the CH stretching region of a) the LB-layer formed by Fe_3O_4 -NPs and OA, b) isotropically arranged thin film of OA on TSG.

Table 8. Assignment of symmetric and asymmetric CH_3 - and CH_2 stretching vibrations of OA.

LB-layer wavenumber [cm^{-1}]	Free oleic acid wavenumber [cm^{-1}]	Assignment	Description
2960	2955	$v_{\text{as}}(\text{CH}_3)$	asymmetric C-H stretch
2929	2930	$v_{\text{as}}(\text{CH}_2)$	asymmetric C-H stretch
2877	2872	$v_{\text{s}}(\text{CH}_3)$	symmetric C-H stretch
2859	2857	$v_{\text{s}}(\text{CH}_2)$	symmetric C-H stretch
-	3005	(=C-H)	C-H stretch

Figure 31a shows the topography SFM image of the unmodified TSG surface with a root mean square roughness of 0.7 nm within $1\ \mu\text{m} \times 1\ \mu\text{m}$. The largest structures are 3 nm high (Fig. 31b, section analysis). In LB layers of OA with Fe_3O_4 -NPs, aggregation of NP were observed (Fig. 31c) even when the LB isotherms and transfer data seem to indicate a well-reproducible transfer. The NP can easily be distinguished from the smooth

background. Although most of the particles were indeed present in a monolayer, a section analysis shows that a few particles were located on top of the first monolayer (Fig. 31d). NPs have been embedded into thin films by diverse methods such as electrodeposition,^[232, 233] spin-^[234, 235] and dip-coating,^[236] and layer-by-layer^[237, 238] and vacuum deposition.^[239] Nevertheless, it is still not possible to generate highly ordered and close-packed homogeneous Fe₃O₄-NP monolayers as the particles tend to agglomerate due to their strong magnetic interaction. Typically, the area where NPs were arranged in a monolayer was smaller than 5 μm × 5 μm. Such behavior has also been reported in Ref.^[240, 241].

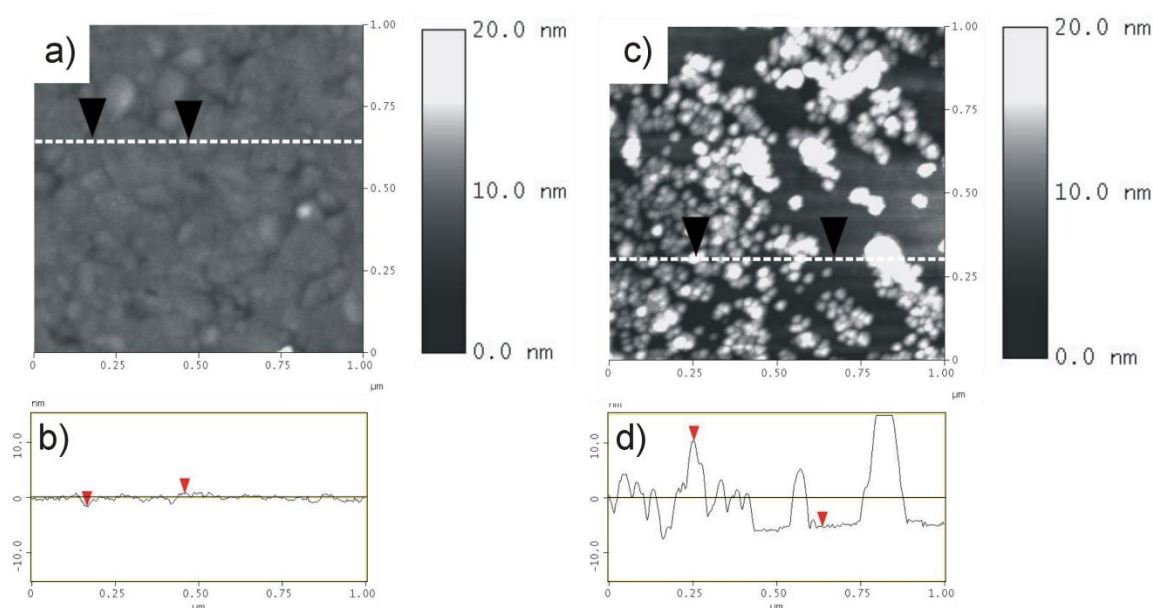


Figure 31. SFM topography images (scan size: 1 μm × 1 μm) recorded in the intermittent mode at a scan rate of 0.8 Hz with Tap300-G tip ($k = 40 \text{ N m}^{-1}$) at a) an unmodified TSG substrate and c) TSG after assembling the LB-layer of Fe₃O₄-NPs and additional OA. The corresponding section analysis of both samples is given below the corresponding images in b) and d).

After LB-transfer of the NP layer on TSG, the sample was carefully immersed into a beaker filled with deionized water. A strong magnet (W-12-N, Supermagnete, Germany) placed in front of the container wall enabled the magnetically triggered release of Fe₃O₄-NPs. Figure 32a shows an SFM image after magnetically triggered release of the Fe₃O₄-NPs from the OA matrix. Except a few particles in the middle of the image frame, the particles had been removed. PM IRRA spectra in Fig. 32 indicate that the OA

matrix remains on the surface after Fe₃O₄-NP removal (for assignment of vibrations, see Tab. 9).

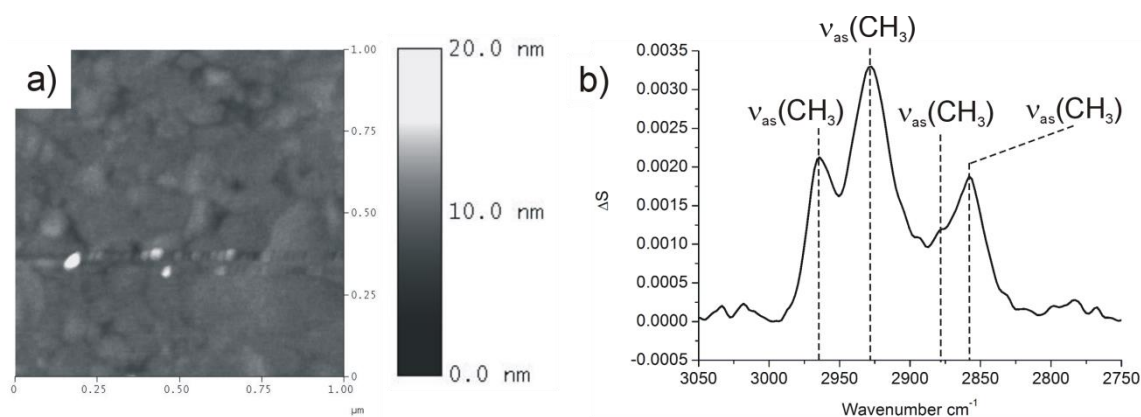


Figure 32. a) SFM topography image (scan area: 1 $\mu\text{m} \times 1 \mu\text{m}$) recorded in intermittent mode at a scan rate of 0.8 Hz with a Tap300-G ($k = 40 \text{ N m}^{-1}$) and b) PM IRRA spectrum in the CH stretching region of the LB-layer after magnetically triggered release of Fe₃O₄-NPs.

Table 9. Assignment of symmetric and asymmetric CH₃- and CH₂- stretching vibrations of OA (LB-layer after removal of Fe₃O₄-NPs).

Wavenumber [cm^{-1}]	Assignment	Description
2964	$\nu_{\text{as}}(\text{CH}_3)$	asymmetric C-H stretch
2927	$\nu_{\text{as}}(\text{CH}_2)$	asymmetric C-H stretch
2878	$\nu_{\text{s}}(\text{CH}_3)$	symmetric C-H stretch
2857	$\nu_{\text{s}}(\text{CH}_2)$	symmetric C-H stretch

However, attempts for reuptake failed. It was assumed that the lateral mobility and flexibility of oleic acid molecules in the matrix reduces the specificity of imprinted cavities and that this system suffers from the lack of a stable matrix after template removal. Irradiation with low intensity UV light ($\sim 185 \text{ nm}^{[242]}$) should initiate cross-linking to OA molecules, which might lead to the formation of a more stable matrix. The available UV light in this study had a higher wavelength (365.4 nm) and therefore did not achieve the expected effect. Furthermore, the detection of iron oxide NPs in monolayer amounts turned out to be more difficult than expected at least with simple instrumentation. XPS was not promising for particle detection as it was not possible to distinguish between NPs inside cavities and on the surface of the films. Much effort was also put into attempts to create Fe₃O₄-NPs with different ligands in order to prevent NP

agglomeration. However, ligand exchange procedures were poorly reproducible and difficult to characterize, hence experiments were performed with well-defined batches of NP as a template and analytes.

It was shown that LB films of magnetic Fe_3O_4 -NP can be successfully transferred to TSG substrates. This sub-monolayer of Fe_3O_4 -NPs could be released from the substrate surface in an external magnetic field of a permanent magnet opening the route for the controlled, local and directed release of specified small quantities of magnetic nanoparticles.

5.4 System with gold NPs and poly(aniline)

In our cooperation with Professor Daniel Mandler's group we published the first realization of nanoparticle imprinted polymers combined with electrochemical detection.^[194] The new sensor principle was successfully demonstrated with a PANI film transferred simultaneously with template AuNPs by the Langmuir-Blodgett technique onto an indium doped tin oxide substrate. Citrate-protected AuNPs were dissolved in the aqueous subphase (pH 5) of a Langmuir trough. An insulating PANI layer was spread at the water-air interface. This layer is positively charged at pH 5 while the citrate-protected AuNPs carry negative charges at the same pH. The extracted AuNPs strongly associate with the PANI film to form a preorganized composite at the water-air interface. This approach allows one to control the concentration of the AuNPs, because successive deposition results in multilayers. Electron microscopic images after the transfer showed randomly distributed NPs with insignificant agglomeration. The release of the AuNPs could be easily controlled and observed by electrooxidation. In this system, SEM investigations after electrooxidation confirm the formation of open cavities in the film.^[194] It was possible to show that the cavities are capable to re-capture analyte NPs with size-exclusion behavior. This was accomplished by an electrochemical approach in the same way as used for the release of the template NPs. Nevertheless, not all embedded AuNPs could be dissolved, some remained chemically unchanged, as was confirmed by X-ray photoelectron spectroscopy. Figure 33 shows the Au 4f spectra before (bottom) and after (top) electrochemical oxidation and release of the AuNPs. Before the oxidation, the

metallic AuNPs showed a peak shape with reduced asymmetry compared to the spectra of bulk gold. After oxidation, the overall intensity was greatly diminished.

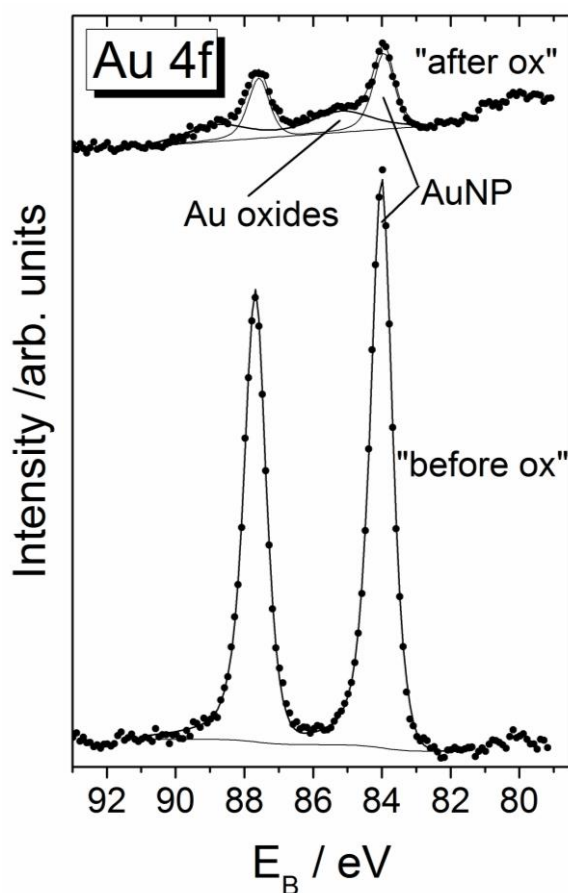


Figure 33. XPS of AuNPs in PANI film after LB transfer of 2 layers (bottom) and subsequent electrochemical oxidation by linear sweep voltammetry between 0.0 V and 1.4 V vs. Ag/AgCl with a scan rate of $\nu = 0.1 \text{ V s}^{-1}$ in aqueous 0.1 M KCl solution.

Furthermore, the appearance of a signal at higher binding energy E_B (Au $4f_{7/2}$, $E_B = 85.22 \text{ eV}$, 10 % of the intensity before LSV) indicated the presence of gold in higher oxidation states often described as mixed oxides of Au^{I} and Au^{III} species.^[243] This gold oxide should dissolve in chloride-containing solution. Dissolution of the Au nanoparticles might be inhibited or prevented in case that the local chloride concentration is insufficient or the access of the solution is hindered by a PANI film covering the AuNPs to the solution side. Remaining metallic Au (Au $4f_{7/2}$, $E_B = 83.94 \text{ eV}$, 13 % of the intensity before LSV) may result from AuNPs that were electrically insulated from the ITO support during oxidation or from re-reduction of initially formed Au_2O_3 . There was no

indication that secondary electrons during XPS measurements contributed to the reduction.

Beside XPS measurements, the authors contributed to this study by SFM thickness determination of the PANI layer. The PANI film of 3 LB layers with embedded AuNPs is used as an example. The film was locally removed by scanning a frame of $1\ \mu\text{m} \times 1\ \mu\text{m}$ over 5 min with an MSCT tip and a setpoint of 10 V in contact mode to remove the PANI layer, but not to alter the ITO surface. Afterwards, the force was reduced and a larger frame was scanned (Fig. 34a). The local removal of the PANI film was confirmed by the friction force image recorded simultaneously (Fig. 34b). This image highlights the material contrast between bare ITO and PANI. The roughness in the height image (Fig. 34a) is due to the roughness of the ITO substrate. Using the software tool “step height”, the line scans within the white rectangle were averaged (profile in Fig. 34c). The height difference was 3 nm taken as the average of data between the green marker lines vs. the average between the red marker lines. This corresponds exactly to previous thickness determinations by SFM in air and by XPS.^[150] With measurements in a 0.1 M KCl solution it was shown that swelling effects of the film in water are below the detection limit.

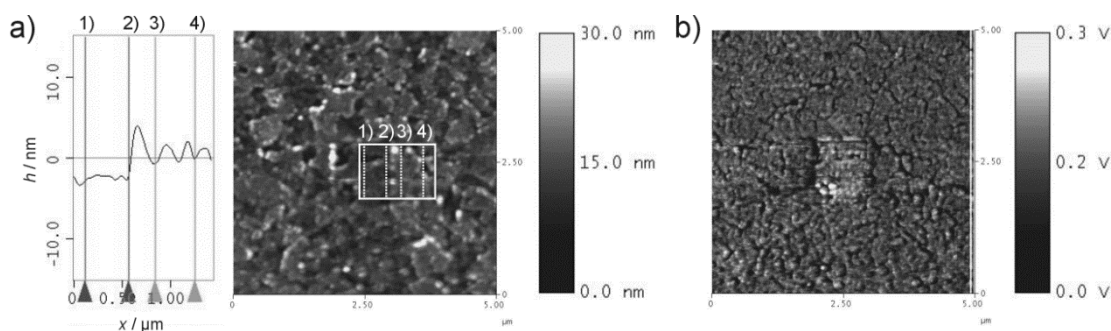


Figure 34. Thickness determination of a film of 3 LB layers of PANI with AuNPs in 0.1 M KCl. a) Contact mode image of a region with the film removed by scratching and the corresponding cross section showing the average height data along the edge of the modified area. b) Friction image of the modified area.

From this approaches we learned two lessons. The matrix is by far the most critical component determining the success of selective recognition of NPs. The lack of an ohmic contact between embedded particles and the substrate prevents the dissolution

of NPs (Fig. 35, NP A and B). It is particularly important that the NIP-matrix have a smaller thickness than the diameter of the NP (as illustrated in Fig. 35 with NP C and D) because thicker films would prevent the access to the solution phase. At the same time, the formed cavity should also be thick enough to enable size exclusion and to provide sufficient area for specific interaction (Fig 35, formed cavities after electrochemical removal).

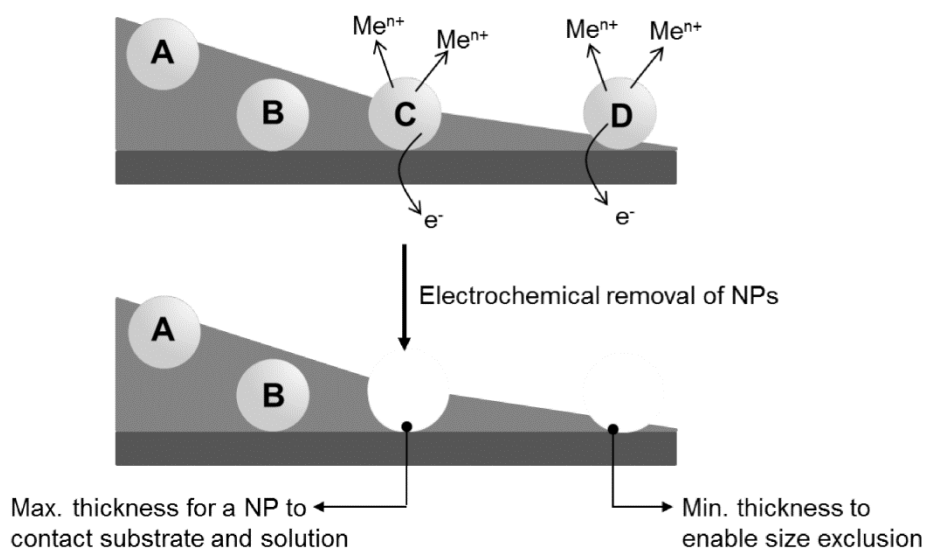


Figure 35. Model of the electrochemical NP removal process shows the effect of matrix thickness. The dissolution of particle A and B is prevented due to the lack of an ohmic contact to the substrate. NIP-matrices with a smaller thickness than the diameter of the NP provide an access to the solution phase. Therefore particle C and D can be removed.

This work demonstrates for the first time the size-exclusion of nanoparticles by extremely thin, imprinted polymers. Changing the pH in our system provides a convenient way to adjust specific interaction between the matrix and the analyte NPs. The recognition ability of the NIPs was examined by inserting the template matrix in an AuNP containing alkaline solution (pH 10), since the PANI film is neutral at this pH and non-specific electrostatic attractions between the polymer matrix and the negatively charged AuNPs are eliminated. The insulating poly(aniline) allows communication only to those NPs that are inside the cavities and in an ohmic contact to the substrate electrode. This assumption is supported by Ahn and Bard's investigations of single nanoparticle collision events on titanium dioxide passivated n-silicon electrodes, as tunneling electron

transfer could only be observed when the thickness of the blocking layer is less than 2 nm.^[122]

6. NIP system realized by sequential deposition of matrix and nanoobjects

As it is evident from the approaches in Chapter 5, the formation of NIP is not trivial and requires taking into consideration several interdependent issues. Different questions raised related to the material the NPs are made of, the chemical nature and formation of the matrix, the removal of template NP and the reuptake of analyte NP. The objective of this part is to form NIPs with a quite different and more mature point of view on how to design and study such systems. Considering the experience related to the one step deposition of nanocomposites a new approach was followed for NIP fabrication realized by a sequential deposition of nanoobjects and matrix (Chapter 6.3). Since the removal of imprinted iron oxide (magnetite) NPs from a matrix by an external magnetic field was not simple, the focus was placed on NPs made of metals, namely gold and silver, that can be anodically dissolved in case of an ohmic contact to the electrode surface. The current during dissolution gives an immediate and quantitative indication about the success of the removal step. The major drawbacks of using a matrix formed from molecular mono- or multi layers are their low stability and the limited thickness of the layers. Therefore, electropolymerization was used as a mean of controlling the NIP thickness. Two optional polymers, namely poly(phenol) and poly(plumbagin), were studied in terms of parameters such as the thickness, rigidity and permeability. The characterization of plumbagin-based polymer films by SFM and SEM discussed in Chapter 6.2 was my contribution to the joint publication^[244] with Saustin Dongmo (Wittstock's group) on a new class of plumbagin-derived polymers, which allows a free adjustment of the film thickness and apparently led to the permeability and catalytic activity of this polymer. The investigation of phenol-based polymers for NIPs was not part of the published work and was initiated by me and carried together with Anne Staggenborg.

6.1 Immobilization of template gold NP on APTES-modified ITO samples

A variety of strategies have been developed to link AuNPs to properly functionalized surfaces. Among these, the self-assembling approach provides a simple and versatile method to obtain well-ordered 2D nanoparticle arrays in which coverage and spatial distribution can be easily controlled.^[132, 245-248] The bifunctional crosslinker APTES is the most commonly used organosilane for immobilization of colloids and was used here in order to attach AuNPs as templates on ITO electrodes. Figure 36 illustrates schematically the steps involved in the preparation of AuNP/ITO_{APTES} electrodes. Pretreatment of clean ITO electrodes in 1% NH₄OH leads to an active hydroxylated surface layer^[188] necessary for covalent attachment of alkoxy-silanes to the surface via condensation reaction. The contact angle of bare ITO after treatment in NH₄OH was 24.1° providing the hydrophilic nature of a hydroxy-terminated surface. The contact angle of a clean, untreated ITO surface was 83.3° indicating a hydrophobic surface. The APTES layer is grown under dry conditions in order to prevent multi-layer formation.^[249] After the silanization process, no agglomeration was noted in SFM topography images of the ITO_{APTES} surface (Fig. 16 b).

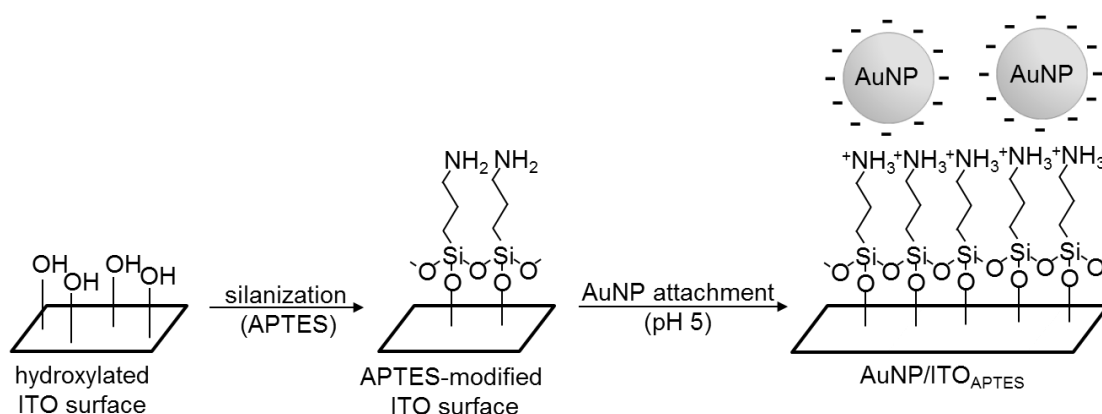


Figure 36. Procedure for the preparation of AuNP/ITO_{APTES} electrodes: a) generation of an active hydroxylated ITO surface, b) silanization with APTES, c) electrostatic assembling of citrate stabilized AuNPs on APTES-modified ITO samples at pH 5.

However, contact angle measurements after silane modification (contact angle = 50.7° Lit.^[138, 250] 50-66°) indicated a successful formation of a APTES-monolayer. Electrostatic interactions between negatively charged AuNPs with a diameter of 30 nm

and the positively charged APTES-monolayer at pH 5.0 enabled a controlled assembly of dispersed NPs onto ITO electrodes. This was evidenced by SEM and SFM. SEM images in Fig. 37 show randomly arranged AuNPs with a broad size distribution and a mean AuNP size of 38.5 nm.

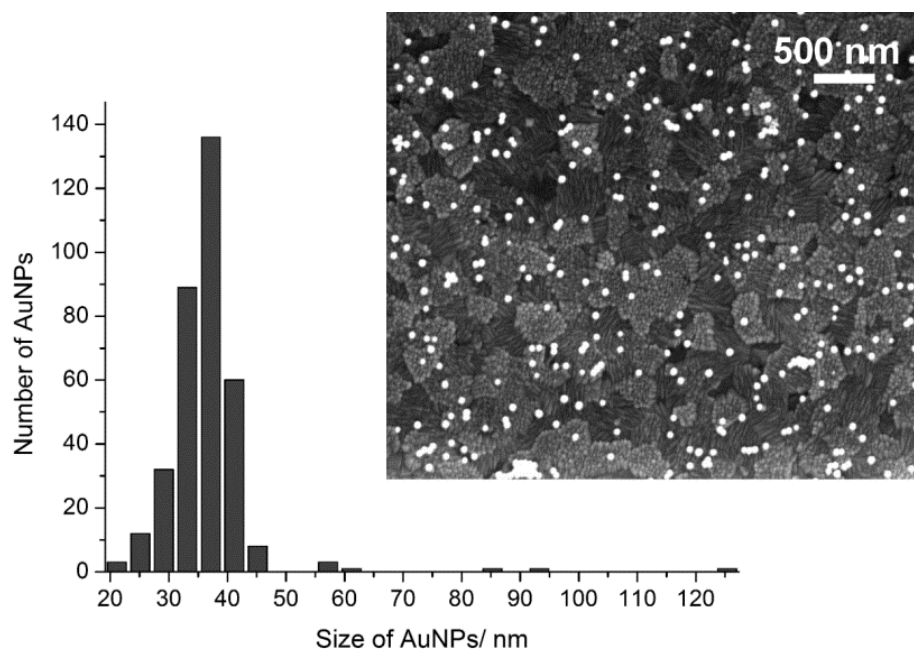


Figure 37. Size distribution of immobilized template AuNPs and corresponding SEM image.

The amount of NPs strongly depends on exposure time of $\text{ITO}_{\text{APTES}}$ to the AuNP solution and on the pH.^[136-138] The time-dependency was confirmed by investigating samples after 1 h, 2 h and 3 h (Fig. 38a-c) by SEM, while saturation coverage of AuNPs on the $\text{ITO}_{\text{APTES}}$ electrode occurs after approximately 24 h (Fig. 38d). During longer exposure time, AuNPs on $\text{ITO}_{\text{APTES}}$ are not well dispersed but rather tend to aggregate and accumulate in certain regions.

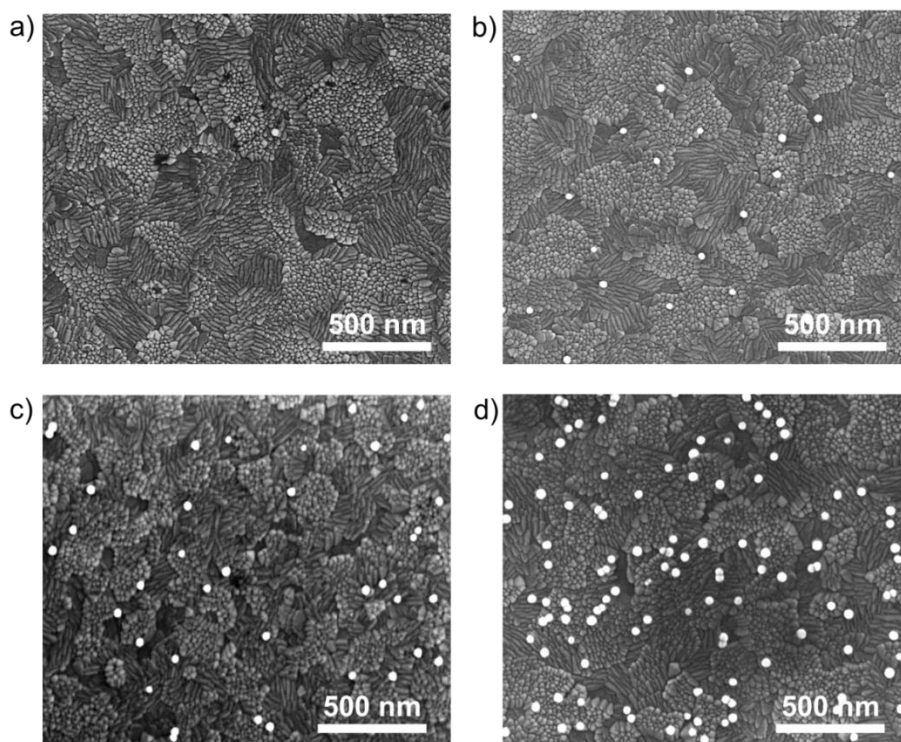


Figure 38. SEM images recorded at 20-30 kV of AuNP/ITO_{APTES} after a) 1 h (1NP), b) 2 h (20 NPs), 3 h (40 NPs), d) 24 h (127 NPs) at $\sim 3.0 \mu\text{m}^2$ area.

SFM topography images of prepared samples confirmed the presence of AuNPs on APTES-modified ITO (Fig. 39). The nanoparticle height was 24.2-39.4 nm measured as difference between the peak height and the average baseline.

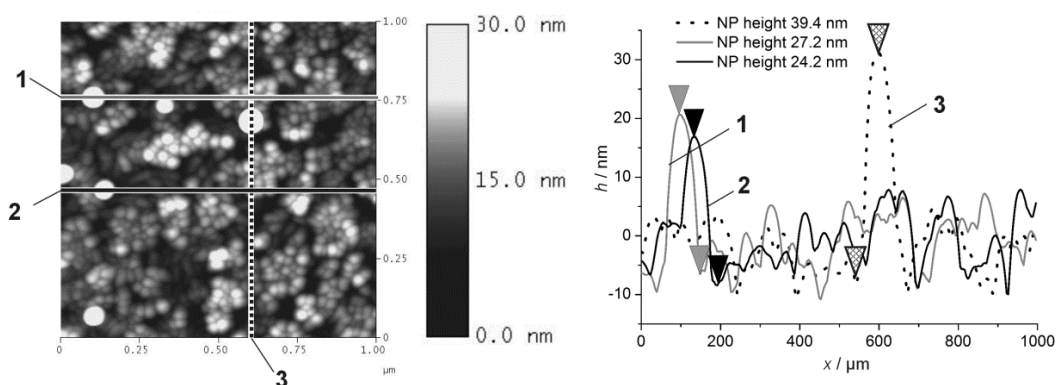


Figure 39. SFM topography images (left panel) recorded in intermittent mode within a scan area of $1 \mu\text{m} \times 1 \mu\text{m}$ using a NCHV-A SFM tip ($k = 42 \text{ N m}^{-1}$) at a scan rate of 1.5 Hz (256×256 pixels) and three extracted cross sections (right panel).

Particle amount and distribution seem to be strongly influenced by the quality of the silane monolayer. Although, silanization is a commonly used approach to modify the surface of ITO, well-controlled introduction of silanes is not straightforward due to the uncontrollable surface hydroxyl concentration of ITO^[251] and the poor reactivity of the functionality.^[252] Furthermore, a rather high surface roughness and inhomogeneity in terms of electric conductivity and composition are responsible for the difficulties encountered in many ITO applications.^[253, 254] It is known that hydroxyl group density on the ITO substrate is lower than that on glass or silicon, and the latter have even a lower roughness enabling the generation of a close-packed silane monolayer, which is an important requirement to achieve a homogeneous distribution of citrate-stabilized AuNPs. However, non-conducting substrates were not suitable for different aspects of this thesis including the electrochemical detection of metal NPs or the formation of electropolymerized thin films. Beside the monolayer quality, the ionic strength of colloidal solutions is a crucial parameter affecting the distribution and amount of immobilized NPs upon an electrostatic attachment.^[132] A promising approach to maintain the positioning of NPs over long distances have been reported by Zhang et al.^[255] through a self-assembled 2D DNA nanogrid, which was successfully used as template to organize 5-nm Au NPs into square lattice with accurate control of interparticle spacing of 38 nm. Evenly distributed AuNP arrangements may find applications in nanoelectronic, nanophotonic and sensor devices.

Finally, LSV was applied in order to determine the accessible amount of template AuNPs (Fig. 41) and to confirm that the immobilized AuNPs undergo electron transfer with the underlying ITO electrode. According to a plot developed originally by Pourbaix,^[256] gold is stable over a large potential and pH range in the presence of water and aqueous solutions free from complexing substances (Fig. 40a). Pourbaix diagrams are generally used for predicting and rationalizing the boundaries of thermodynamic stability for various solid-aqueous systems as a function of pH and the redox potential E . Most of them denote the region of stability of water to reduction (dashed line 6 in Fig. 40a, b) and oxidation (dashed line 7 in Fig. 40a, b). Although thermodynamic data do provide a basis for the study of electrochemical reactions, they do not take into account the kinetic properties of the systems and therefore are not always reliable. It may be seen from Fig. 40a (Au-HO system at 25 °C) that the electrochemical oxidation of gold occurs only at

potentials significantly larger than those of line 5. In solution, the trivalent state of gold is the most stable one, however, in the absence of complexing agents, the dissolved Au^{3+} ion is considered to precipitate as hydrated auric oxide (Au_2O_3) or hydroxide ($\text{Au}(\text{OH})_3$) almost over the whole pH range. The formation of Au_2O_3 is possible at higher E values, but it is less stable than the Au(III) hydroxide.

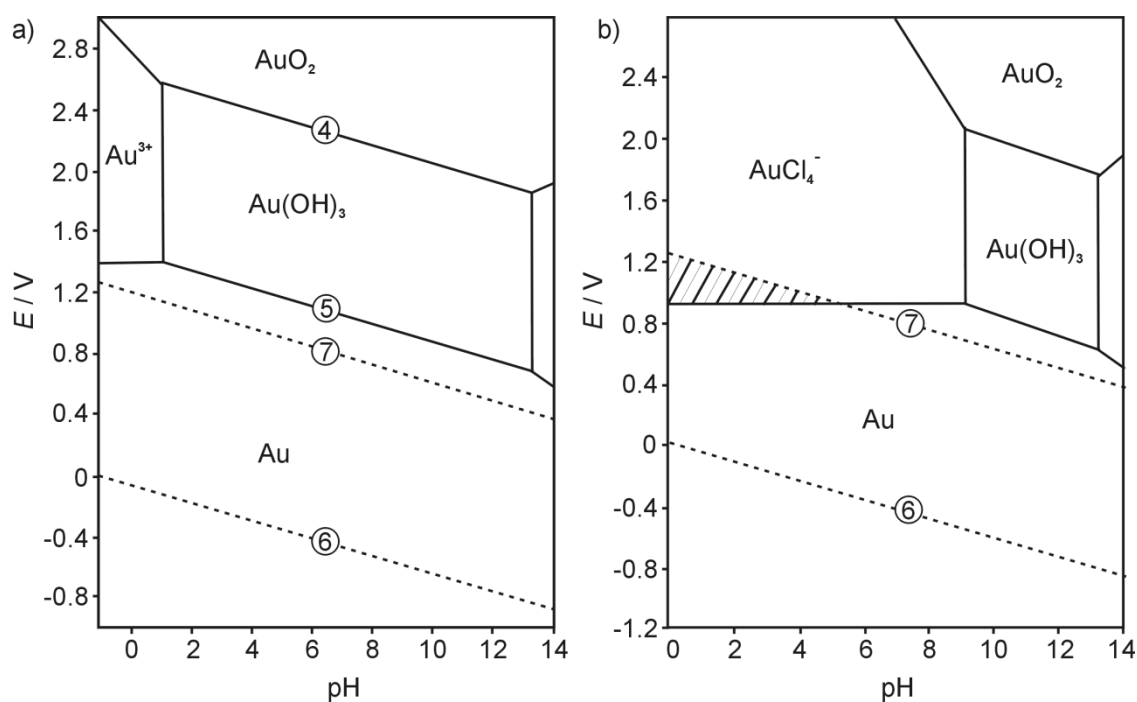


Figure 40. Pourbaix diagram for the systems a) $\text{Au-H}_2\text{O}$ ($[\text{Au}] = 10^{-4} \text{ M}$) based on Ref.^[256] and b) for the system $\text{Au-H}_2\text{O-Cl}^-$ ($[\text{Au}] = 10^{-2} \text{ M}$, $[\text{Cl}^-] = 2 \text{ M}$) based on Ref.^[257] at 25°C .

With increasing potentials the anode becomes covered with a passivation layer of gold peroxide (AuO_2), which is thermodynamically unstable in water and readily decomposes to form Au_2O_3 and O_2 .^[258, 259] In strong acidic media ($\text{pH} > 1$) and at potentials higher than 1.4 V, auric ions exist in a hydrated state ($\text{Au}(\text{H}_2\text{O})_4^{3+}$) as a complex of low stability, which will undergo spontaneous reduction to the metal with the oxidation of H_2O to O_2 . The introduction of trace amounts of certain complexing species such as chloride ions is necessary to stabilize this ion and to destroy the passivating layer. In order to get a better understanding of the tendency of Au^{3+} to form complexes, Finkelstein and Hancock^[257] show the influence of chloride ions to the $\text{Au-H}_2\text{O}$ system (Fig. 40b). Comparison with the thermodynamic data from Fig. 40a shows a reduced domain in which $\text{Au}(\text{OH})_3$, and AuO_2 are the most stable species. Since the Cl^- ion is a

stronger complexing ligand than H_2O , the equilibria in Eq. (4-5) will be established. The extent of the domain of the predominant species $[\text{AuCl}_4]^-$ varies directly with the concentration of Au^{3+} and Cl^- , while the grey shaded region shows the area for which the gold chloride complex is stable in water at 25°C . It is important to note that the chloride promoted dissolution of gold is predicted to occur at much lower potentials than it does in pure water [Chapter 2.3, Eq. (6-15)].

Using 3 M KCl as the gold stripping solution, gold oxidation at $\text{AuNPs}/\text{ITO}_{\text{APTES}}$ occurs at 0.85 V in the first scan, most likely according to reaction (5). In the subsequent scan the peak is slightly shifted to 0.76 V. This is in agreement with calculated formal potential of gold in the presence of chloride ions [Chapter 2.3, Eq. (15)]. Scans were performed until no further metal oxidation was detected. Typically, this was in the 3rd sweep (Fig. 41). In an aqueous 0.1 M H_2NaPO_4 solution free of complexing species, gold oxidation occurs at a potential of 1.1 V (Fig. 49), which clearly show that the introduction of a complexing agent like potassium chloride can be useful to shift the redox potential of gold to a more negative value.

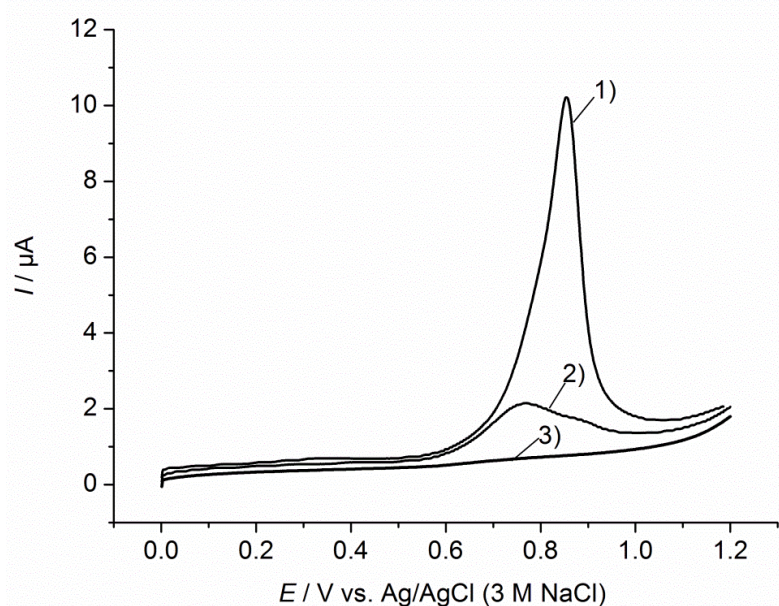


Figure 41. LSV of $\text{AuNPs}/\text{ITO}_{\text{APTES}}$ in 3 M KCl solution, $\nu = 10\text{ mV s}^{-1}$.

Subsequent SEM measurements confirmed the complete removal of NPs. Integration of the area of the AuNP oxidation peaks in Fig. 41 between $E_1 = 0.55\text{ V}$ and $E_2 = 1.1\text{ V}$ vs. a linear background according to Eq. (20), where ν is the scan rate (10 mV

s^{-1}) and I and E are the current and potential, together with the area $A = 0.5 \text{ cm}^2$ of the ITO electrode revealed a charge density Q/A of $5.02 \times 10^{-5} \text{ As cm}^{-2}$ from which the AuNP coverage of $\sim 1.25 \times 10^8 \text{ NPs cm}^{-2}$ was calculated as shown by the following example:

$$\frac{Q}{A} = \frac{1}{v \cdot A} \int_{E_1}^{E_2} I(E) dE \quad (20)$$

→ Mass m_{AuNP} of one AuNP with a diameter of 30 nm (NP radius $r = 15 \text{ nm}$, density of gold $\rho = 19.32 \text{ g cm}^{-3}$):

$$V_{\text{AuNP}} = \frac{4}{3} \cdot \pi \cdot r^3 = 14137.17 \text{ nm}^3 = 1.41 \cdot 10^{-17} \text{ cm}^3 \quad (21)$$

$$m_{\text{AuNP}} = \rho \cdot V_{\text{AuNP}} = 19.32 \text{ g cm}^{-3} \cdot 1.41 \cdot 10^{-17} \text{ cm}^3 = 2.73 \cdot 10^{-16} \text{ g} \quad (22)$$

→ Amount N_{Au} of Au atoms in one AuNP of 30 nm diameter:

$$n_{\text{Au}} = \frac{m_{\text{AuNP}}}{M_{\text{AuNP}}} = \frac{2.73 \cdot 10^{-16} \text{ g}}{196.96 \text{ g mol}^{-1}} = 1.39 \cdot 10^{-18} \text{ mol} \quad (23)$$

→ Required charge Q_{AuNP} to remove one AuNP with a diameter of 30 nm ($n_z = 3$, $F = 96485 \text{ As mol}^{-1}$):

$$Q_{\text{AuNP}} = n_{\text{Au}} \cdot n_z \cdot F = 1.39 \cdot 10^{-18} \text{ mol} \cdot 3 \cdot 96485 \text{ A s mol}^{-1} = 4.01 \cdot 10^{-13} \text{ As} \quad (24)$$

→ Integrated charge Q_{total} obtained on $A = 0.5 \text{ cm}^2$ electrode area:

$$\frac{Q_{\text{total}}}{A} = \frac{1}{v \cdot A} \int_{E_1}^{E_2} I(E) dE = \frac{2.51 \cdot 10^{-5} \text{ A s}}{0.5 \text{ cm}^2} = 5.02 \cdot 10^{-5} \text{ As cm}^{-2} \quad (25)$$

→ Number Γ_{NPec} of electrochemically dissolved particles:

$$\frac{\Gamma_{\text{NPec}}}{A} = \frac{Q_{\text{total}}}{A} \cdot \frac{1}{Q_{\text{AuNP}}} = \frac{2.51 \cdot 10^{-5} \text{ A s}}{0.5 \text{ cm}^2} \cdot \frac{1}{4.01 \cdot 10^{-13} \text{ A s}} = 1.25 \cdot 10^8 \text{ NPs cm}^{-2} \quad (26)$$

Based on SFM images in Fig. 39 about 5-6 AuNPs can be noted within the area of $1 \times 1 \mu\text{m}^2$ ($5.5 \cdot 10^8 \text{ NPs cm}^{-2}$), which is comparable to the calculated number of electrochemically dissolved NPs in Eq. (26).

Aside from knowing the stability range of the NPs, it is important to know in which potential range the ITO substrate is stable, as that presents a major limitation for

the combination of systems. Liu et al.^[260] show that the ITO films partially dissolve and form particles consisting of metallic indium and tin upon applying negative potentials (< -1.0 V vs. Ag/AgCl). Furthermore, several studies^[261-263] confirm that apart from the potential limit, the pH and the anion of the electrolyte and the duration of cathodic polarization play a vital role in the electrochemical stability of ITO and should be borne in mind when performing electrochemical experiments. However, there is a relatively wide potential range available (AuNP oxidation at 0.85 V and ITO reduction at approximately -1.0 V) to select appropriated processes, i.e. for the generation of a matrix.

6.2 Electropolymerization of conformal films

In this part of the work an appealing approach was introduced to realize matrix systems with film thicknesses controlled by the deposition potential and time. While conventional electropolymerization of 5-hydroxy-2-methyl-1,4-naphthoquinone (plumbagin) leads to self-limited growth of an inhibiting film (polyPLG/GC, Fig. 42a), electropolymerization onto a grafted monolayer of plumbagin on glassy carbon (PLG/GC) yields continuous growth of a polymer film (polyPLG/PLG/GC, Fig. 42b).^[244]

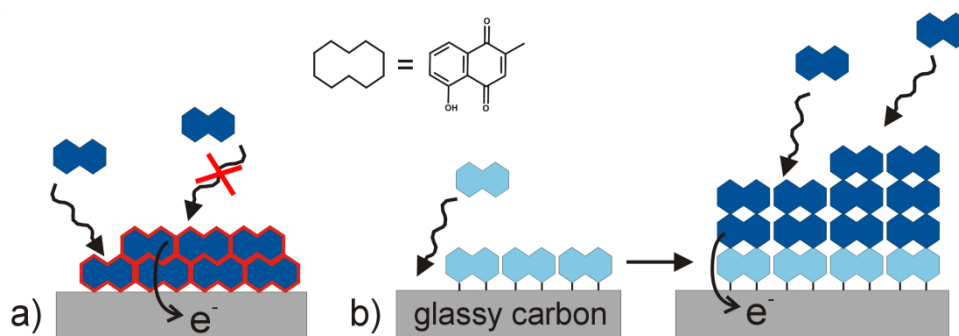


Figure 42. Schematic illustrating a) the conventional self-limiting electropolymerization of plumbagin to an inhibiting film (polyPLG/GC) and b) electropolymerization onto a grafted monolayer of plumbagin on glassy carbon (PLG/GC) showing a continuous growth of a polymer film (polyPLG/PLG/GC).

The electrochemical properties of polyPLG/PLG/GC have been intensively characterized by CVs and showed the preservation of the redox chemistry of the quinone system within the polymer. The surface morphology and thickness of polymer films were

investigated using SEM and SFM. Thickness measurements of polyPLG/PLG/GC were performed after 10, 25, 50, 100 and 150 potential cycles in 0.2 mM plumbagin onto PLG/GC by scratching a selected $1\ \mu\text{m} \times 1\ \mu\text{m}$ region of the polymer film until the underlying GC electrode was exposed using an SFM tip. Full details of all data points are given in the Appendix, Fig. B1.

Figure 43 shows a plot of SFM-determined film thicknesses vs. number of potential cycles for different films. For polyPLG/PLG/GC (Fig. 43, solid line) a fast increase in film thickness was observed up to 50 cycles followed by a slower further growth when the film-solution interface was far from the surface of the GC electrode. In the case of polyPLG/GC (Fig. 43, dashed line), thickness was much smaller (12 nm after 25 cycles) than at polyPLG/PLG/GC (25 nm after 25 cycles) and remained at this value even after further cycling.

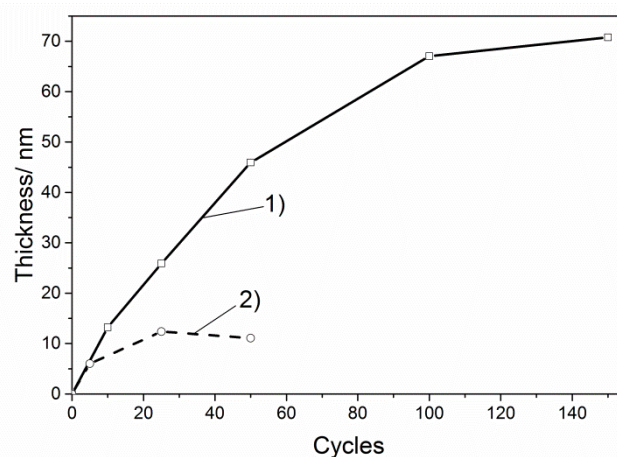


Figure 43. SFM thickness determination of 1) polyPLG/PLG/GC after 10, 25, 50, 100, 150 potential cycles and 2) polyPLG/GC after 5, 25, and 50 potential cycles.

Independent of the electrode nature and the layer thickness, the surface structure of polymers appeared to be homogeneous and smooth with no significant agglomeration. Figure 44a shows an example of a polyPLG/PLG/GC formed in 25 CV cycles. The surface topography was dominated by polishing streaks on the GC support that are smaller than 20 nm in depth. The substrate features were flattened out and lose contrast as the film thickness grows during further cycling (Fig. 44b).

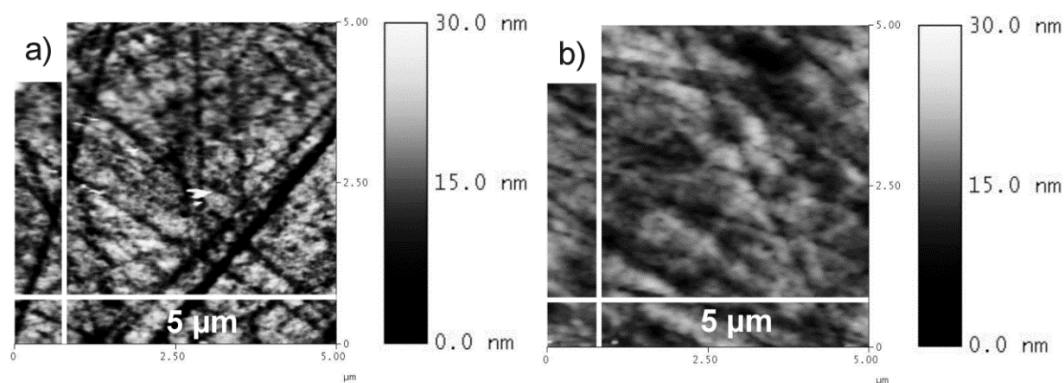


Figure 44. SFM topography images (scan area: $5\ \mu\text{m} \times 5\ \mu\text{m}$) recorded in contact mode with a MSCT tip ($k = 0.6\ \text{N m}^{-1}$) of the polyPLG/PLG/GC after a) 25 and b) 100 CV cycles.

Complementary SEM measurements revealed a homogeneous polyPLG/PLG/GC film. As observed in the tilted (40°) plane of the sample, the morphology of the polymer is characterized by a globular morphology and pits probably affected by the grafted PLG layer (Fig. 45b). The surface PLG/GC (Fig. 45a) after grafting has a very different morphology. In contrast, direct electropolymerization of plumbagin on GC (polyPLG/GC) yields a dense and thin film (Appendix, Fig. B2b) that is conformal to the topography of the underlying GC substrate (Appendix, Fig. B2a), a feature very similar to well-known polyphenol films.

The preservation of the redox activity of plumbagin is caused by the quinone group and its ability to produce semiquinone radicals.^[264-266] The self-limiting behavior was related to the phenolic part of this compound. Electropolymerization of phenols is a prototypical example for the formation of an insulating film.^[267-269] The use of phenol (see following Chapter 6.3) for the preparation of NIPs, raises an interesting question, whether the growing mode of PPh could be also influenced by a grafted PLG monolayer. Indeed, CVs obtained for the electropolymerization of phenol on a PLG/GC electrode indicate a continuously film grow over many potential cycles.^[244]

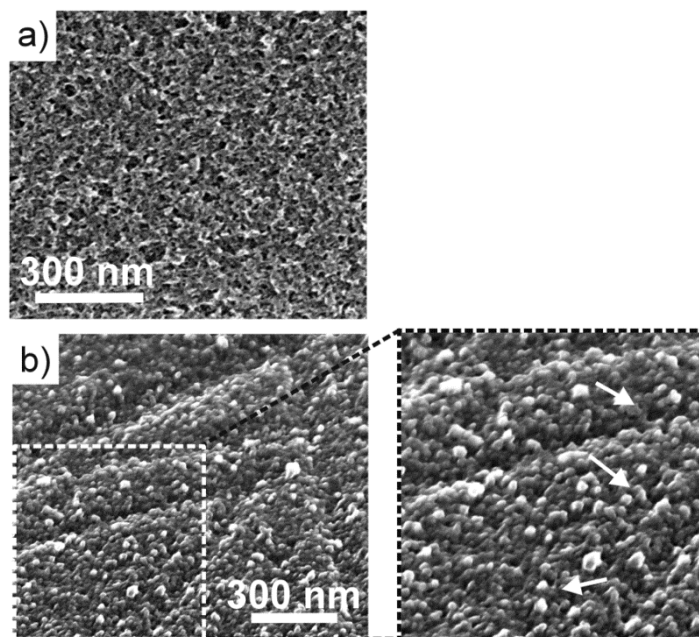


Figure 45. SEM images recorded at 15-25 kV of a) PLG/GC and b) poly/PLG/PLG/GC after 25 cycles.

Surprisingly, SFM thickness determination could not prove an unrestricted growth of the PPh on grafted GC. The thickness is 6.2 nm and thus comparable to PPh films obtained at bare GC. However, SFM topography images clearly show that the structure of the surface changes if the electrode was previously modified with a monolayer of PLG (Fig. 46, a-PPh on bare GC, b-PPh on PLG/GC). The topography of the polymer is characterized by globular structures, which is probably affected by the grafted PLG layer and comparable to the topography of poly(plumbagin) layers at PLG/GC.

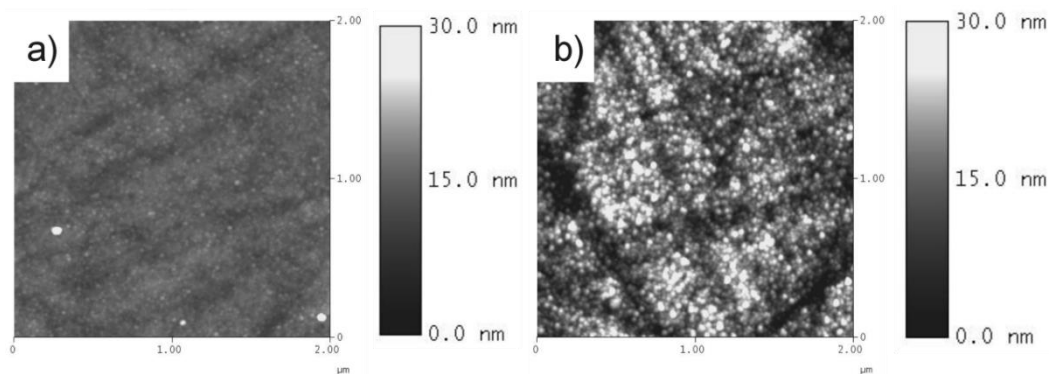


Figure 46. SFM topography images recorded with the MSCT SFM tip ($k = 0.6 \text{ N m}^{-1}$) at a scan rate of 1.0 Hz and with a resolution of 256×256 pixels show the surface of PPh deposited on a) bare GC and b) PLG/GC.

To conclude, the grafting of plumbagin allows subsequent electropolymerization of a plumbagin polymer. The potential observed during electropolymerization was different than in direct electropolymerization on bare GC. In contrast to polyPLG/GC, the growth of polyPLG/PLG/GC is not limited. This allows a free adjustment of the film thickness that and apparently led to the permeability of this polymer. The controlled formation of a macroscopically smooth film with permeability for electrolytes might also be used for nanoparticle imprinted polymers. However, a significant amount of work has to be done in order to clarify the mechanisms of phenol during electropolymerization on the grafted GC electrode.

6.3 Polyphenol-based NIP systems

The last approach in order to obtain polymer-based matrices is performed by electropolymerization of phenol at AuNP/ITO_{APTES} (Fig. 47). The first step of NIP fabrication includes the organization of AuNPs as templates on amino-terminated ITO sample. This is realized by electrostatic interaction between the negatively charged NPs and the positively charged monolayer (AuNP/ITO_{APTES}, Chapter 6.1). In the second step a thin matrix is formed by electropolymerization of phenol, which has a thickness of the order of the used AuNPs (PPh/AuNP/ITO_{APTES}).

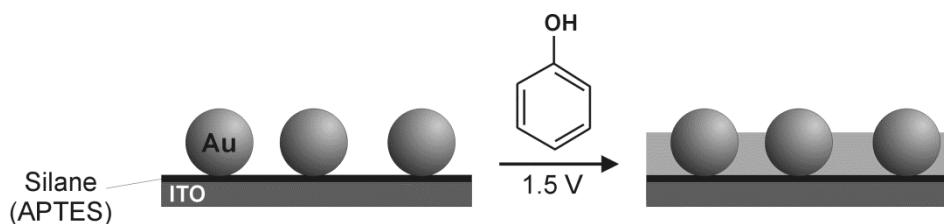


Figure 47. Schematic representation of the 2D composite of AuNPs and the electrochemically generated PPh film.

The expected advantage of phenol and phenol derivatives for forming the NIP matrix is their self-limiting film growth during electropolymerization.^[270] Because the films grow until the complete passivation of the electrode, they are uniformly distributed over the entire electrode area, show a constant film thickness and are almost free of defects. However, they can show selective permeability for different molecules and have found application in the field of biosensors as selectively permeable membranes, for instance for H_2O_2 .^[271, 272] Their robustness has been used for immobilization of enzymes such as glucose oxidase,^[270] and for the protection against unwanted adsorption on or reaction with interfering substances.^[273] Electropolymerized MIPs based on phenol derivatives were used as receptor layers in capacitive chemical sensors.^[274] Therefore, it was expected that this polymer would also be suitable to form NIPs.

Electropolymerization of phenol can be carried out in organic^[275-277] as well as in aqueous^[267, 278, 279] solutions. The polymerization mechanism is well described in literature.^[267, 280, 281] Anodic oxidation of the phenolate ion yields to the phenolate radical as initiation step. The propagation occurs by a head-to-tail coupling of two phenolate ions, deprotonation and again anodic oxidation. The monomers can be coupled in the ortho- or para-position to each other, from which the para-attack is preferred.

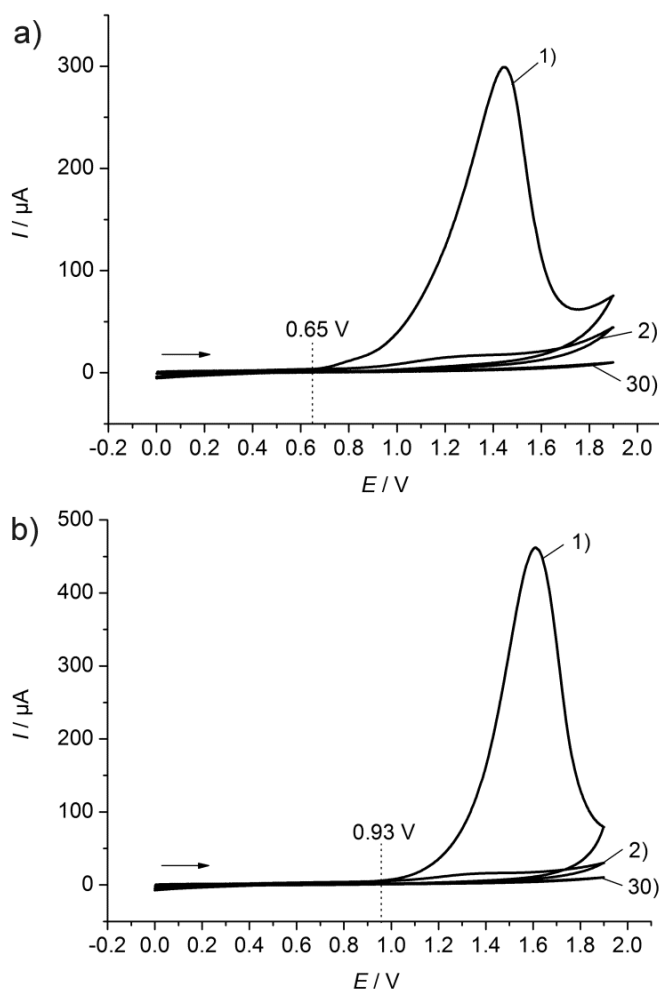


Figure 48. CV for the electropolymerization of phenol at a) AuNP/ITO_{APTES} and b) ITO_{APTES} during the 1st, 2nd and 30th cycle, in an aqueous solution containing 50 mM phenol + 0.1 M NaH₂PO₄ at $v = 50 \text{ mV s}^{-1}$.

Figure 48a shows the 1st, 2nd and 30th CV during PPh deposition from an aqueous solution containing 50 mM phenol + 0.1 M NaH₂PO₄ at AuNP/ITO_{APTES}. There is a distinct phenol oxidation peak around 1.4 V in the 1st cycle. A decrease in the anodic current during progressive potential cycling indicates the formation of an insulating PPh layer.

SFM topography images of PPh films on bare ITO showed a smooth surface morphology. There were no differences to PPh films on ITO_{APTES} electrodes in roughness and thickness (Appendix, Fig. C1). The estimated RMS surface roughness ranged between 3.0-3.5 nm over a $5 \mu\text{m} \times 5 \mu\text{m}$ area and actually reflected the roughness of an untreated ITO surface (Fig. 16a). SFM thickness measurements at ITO_{APTES} revealed

reproducible film thicknesses of 16 to 19 nm as a result of the self-limiting film growth (Appendix, Fig. C1a). The estimated thickness was consistent with observations made by Kang et al.^[189] at similar conditions among a wide range of tested scan rates, cycles and phenol concentrations.

The character of phenol oxidation CVs recorded on ITO_{APTES} (Fig. 48b) is the same as of those observed on AuNP/ITO_{APTES} samples (Fig. 48a). However, there is a difference in the onset and peak potentials. The current response at ITO_{APTES} samples starts to increase at a potential positive of 0.93 V (Fig. 48b), while the oxidation peak is located at around 1.6 V. In the presence of AuNP templates the anodic current rises already at 0.65 V. By recording a CV in phenol-free 0.1 M NaH₂PO₄-electrolyte it could be confirmed that this signal is not due to gold oxidation. In this electrolyte gold oxidation starts only at 0.8 V with a peak at 1.1 V (Fig. 49), while the currents are caused by the formation of auric hydroxide or oxide (detailed discussion in Chapter 6.1). The dissolution of gold at similar potentials in Fig. 41 was only possible due to the presence of complexing chloride ions. Prolonged cycling in the range between 0 V and 1.4 V leads to successive decrease of both, the oxidation and reduction peaks. Chloride promotes the oxidation of gold, while the absence of Cl⁻ causes the redox potential of AuNPs to shift to a higher potential.

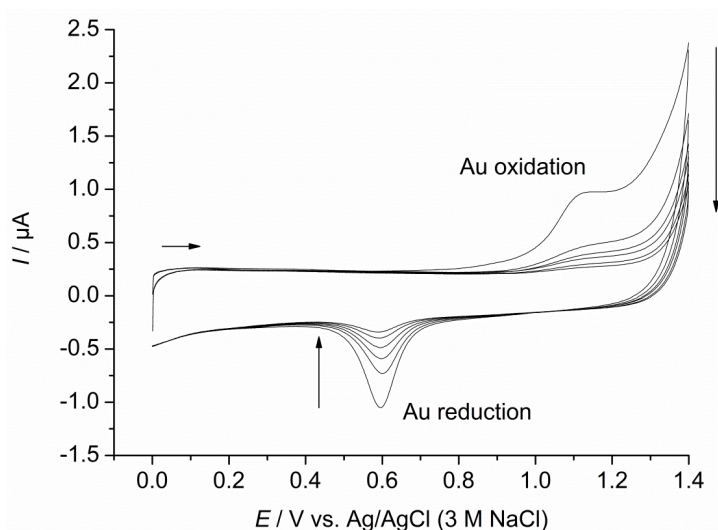


Figure 49. CV recorded at AuNP/ITO_{APTES} in an aqueous solution containing 0.1 M NaH₂PO₄ with a scan rate of $\nu = 0.05 \text{ V s}^{-1}$ indicating the oxidation and reduction of gold.

Complementary studies on massive Au electrodes showed that the deposition of PPh occurs at lower potentials (0.5-1.1 V vs. Ag/AgCl, Fig. 50) than it does at ITO_{APTES} under the same conditions (0.9-1.9 V vs. Ag/AgCl, Fig. 48b). This suggests that the AuNP might be coated with an insulating PPh film even before the ITO substrate is coated. The film formation of PPh on bare Au electrodes is comparable to that on ITO as the oxidation current substantially decreases in the second scan due to the formation of an insulating layer.

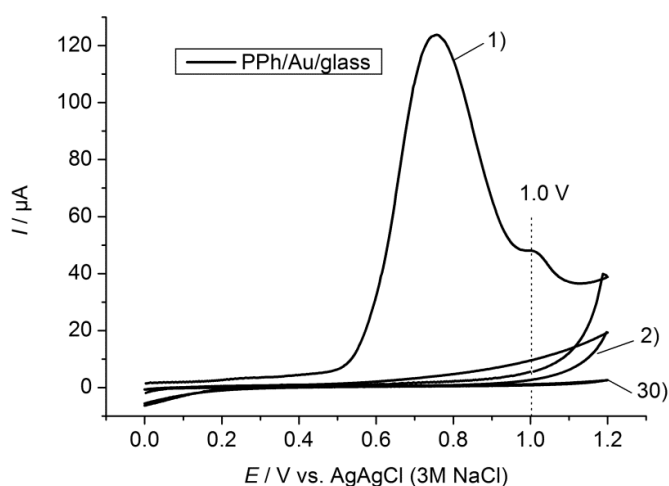


Figure 50. The 1st, 2nd and 30th CV during the electropolymerization of phenol in an neutral (pH 6.5-7.0) aqueous solution containing 50 mM phenol + 0.1 M NaH₂PO₄ at $v = 50 \text{ mV s}^{-1}$ at a bare Au/glass electrode.

The blocking behavior of PPh on Au/glass electrodes was confirmed in permeability test experiments using [Ru(NH₃)₆]Cl₃ as redox probe (Fig. 51a).

SFM investigations reveal a smooth polymer surface (RMS = 1.8 nm), which actually represents the roughness of the bare Au surface (Fig. 51b). The thickness is determined as 1-2 nm using SFM in contact mode. In some CVs as shown in Fig. 50a, an additional peak was observed at 1.0 V during electropolymerization of phenol at bare Au/glass electrodes. Considering the gold oxidation response demonstrated in the CV of the blank NaH₂PO₄-electrolyte at AuNP/ITO_{APTES}, this peak can be attributed to the formation of gold oxide or hydroxide, which appears since the film formed during the first CV scan of phenol polymerization is not completely insulating and thus not preventing this reaction. A vanishing weak peak at 0.6 V in the back scan of the first two

cycles might indicate the electrochemical reduction of oxidized gold species (demonstrated in an enlarged scale in the Appendix, Fig. C2a, b). Usually, this signal disappears in the second polymerization cycle. Even if a clear signature of the Au-oxidation peak is missing, the reduction response is barely visible.

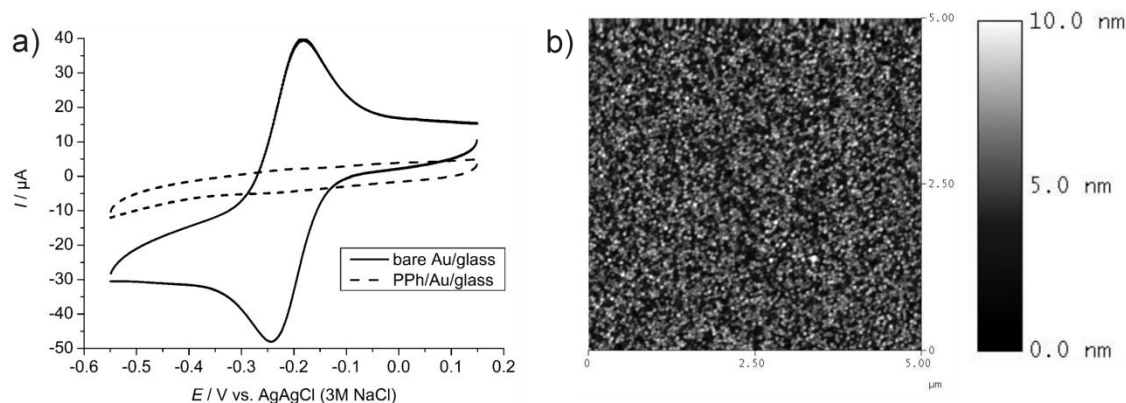


Figure 51. CVs recorded at Au/glass (black curve) and PPh/Au/glass (dashed curve) in 1 mM $[\text{Ru}(\text{NH}_3)_6]\text{Cl}_3$ + 0.1 M KCl at a scan rate of 0.1 V s^{-1} show the permeability before and after the formation of an insulating poly(phenol) film and b) SFM topography images recorded in contact mode within a scan area of $5 \mu\text{m} \times 5 \mu\text{m}$ using a MSCT SFM tip ($k = 0.6 \text{ N m}^{-1}$) at a scan rate of 2.0 Hz and with a resolution of 256×256 pixels.

The deposition of PPh at Au/glass in neutral NaH_2PO_4 -medium occurs at a lower potential causing a passivation of the electrode surface before the potential has reached a value high enough to start the oxidation of gold. Hence, only a small amount of gold can be oxidized, which is the most important reason for suppression of the gold reduction peak in Fig. 50b. Another peak at 0.2-0.3 V in Fig. 50b, which could not be assigned so far, appears only in the first half cycle during the electropolymerization on Au/glass substrates. There is no indication that this peak interferes the application for NIPs.

No evidence of gold dissolution was found in CVs of phenol polymerization in an aqueous neutral NaH_2PO_4 -solution at $\text{AuNP}/\text{ITO}_{\text{APTES}}$ (Fig. 50a). Indeed, the expected Au-oxidation peak ranging between 1.0 V to 1.1 V could be overlapped by the phenol oxidation response, but the reduction process at 0.6 V is missing (Fig. 50b).

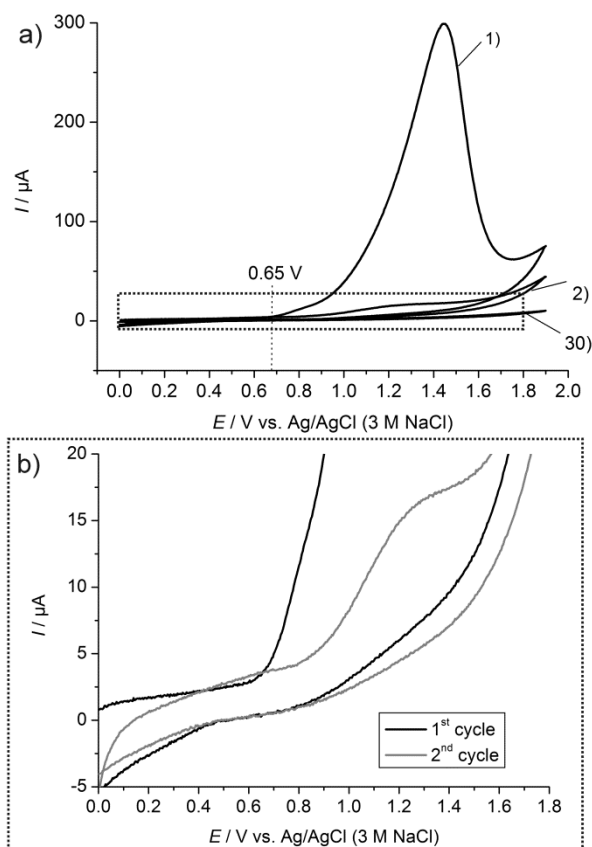


Figure 52. a) The 1st, 2nd and 30th CV for the electropolymerization of phenol at AuNPs/ITO_{APTES} conducted in aqueous solution containing 50 mM phenol + 0.1 M NaH₂PO₄. b) Enlarged view of the 1st (black curve) and 2nd (grey curve) scan.

The studies by SEM and SFM after formation of the PPh matrix confirm the presence of AuNP templates (Fig. 53a, b). Due to the non-conducting nature of the PPh film, SEM observation at a high acceleration voltage led to charge accumulations in the scanned area. Measurements at lower acceleration voltages were not beneficial for structure determination at high spatial resolution (Fig. 53a). Hence, the application of SFM on the polymeric surface is especially favorable to overcome the conductivity limitations of SEM. Characterizations by SFM confirm the dispersion of template AuNP within the polymeric matrix. The layer thickness of the polymer matrix was determined by SFM to be 17-21 nm (Fig. C1b), which is comparable to the thickness obtained at ITO_{APTES}. In the presence of NPs the roughness increases from 3.17 (PPh/ITO) to 3.68-4.17 nm (PPh/AuNP/ITO_{APTES}).

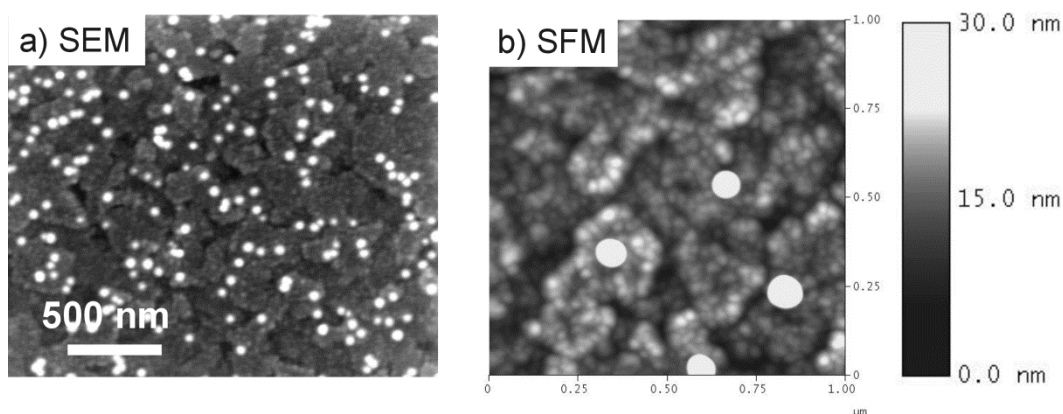


Figure 53. a) SEM image recorded at 15 kV and b) SFM topography image ($1\ \mu\text{m} \times 1\ \mu\text{m}$) measured in the contact mode using a MSCT SFM tip ($k = 0.6\ \text{N m}^{-1}$) at a scan rate of 1.0 Hz with 265×265 pixels of PPh/AuNPs/ $\text{ITO}_{\text{APTES}}$. AuNPs are identified as white dots.

Cyclic voltammograms of a redoxactive probe $[\text{Ru}(\text{NH}_3)_6]^{3+}$ were recorded to obtain information on the permeability in the presence and absence of the PPh film. Figure 54a shows the CVs of $\text{AuNP}/\text{ITO}_{\text{APTES}}$, $\text{PPh}/\text{AuNP}/\text{ITO}_{\text{APTES}}$, and PPh/ITO in 1.0 mM $[\text{Ru}(\text{NH}_3)_6]\text{Cl}_3 + 0.1\ \text{M KCl}$. In analogy to $\text{ITO}_{\text{APTES}}$, bare ITO was used for all control experiments with the bare substrate since the untreated samples showed no significant differences in voltammetric response. The response of $\text{AuNP}/\text{ITO}_{\text{APTES}}$ shows a well-developed quasi-reversible CV for $[\text{Ru}(\text{NH}_3)_6]^{3+/2+}$ (Fig. 54a, dashed curve). The CVs after electrochemical deposition of the insulating PPh film are typical for a blocking layer that permits small residual currents only (Fig. 54 a, black curve for $\text{PPh}/\text{AuNP}/\text{ITO}_{\text{APTES}}$ and grey for PPh/ITO). These residual currents are shown in an enlarged scale in Fig. 54 b for PPh/ITO and $\text{PPh}/\text{AuNP}/\text{ITO}_{\text{APTES}}$. The current response of $[\text{Ru}(\text{NH}_3)_6]^{3+/2+}$ is not completely inhibited. The shape of both CV curves changes towards a sigmoidal shape. Selected samples in Fig. 55a-c represent typical CVs observed from such layers. This may indicate that the reduction of $[\text{Ru}(\text{NH}_3)_6]^{3+}$ occurs at an array of independent microelectrodes. This could be defects in the PPh film and/or, in case of $\text{PPh}/\text{AuNPs}/\text{ITO}_{\text{APTES}}$, AuNPs extending across the PPh film thickness.

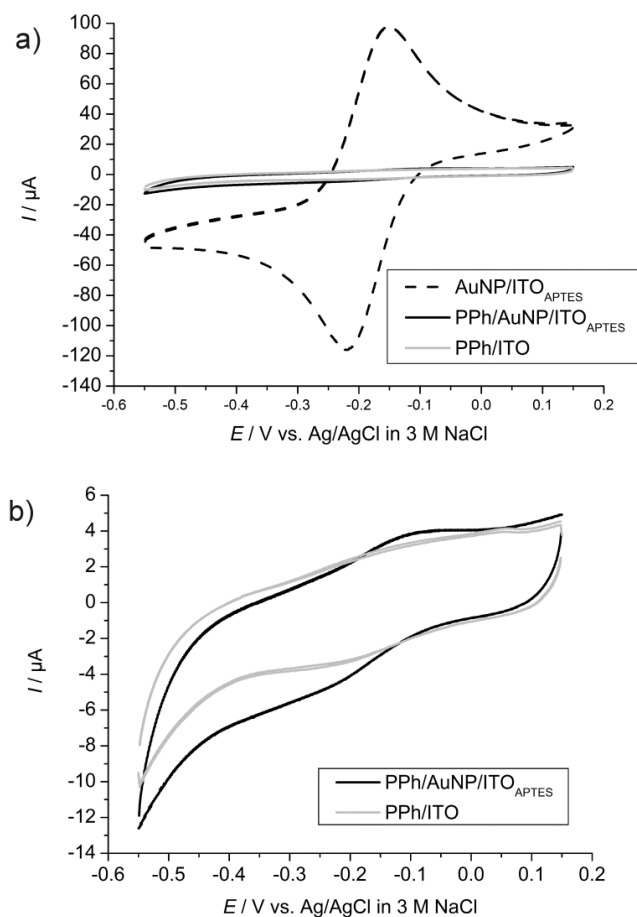


Figure 54. a) CVs recorded at $\text{AuNP}/\text{ITO}_{\text{APTES}}$, $\text{PPh}/\text{AuNP}/\text{ITO}_{\text{APTES}}$ and PPh/ITO in 1 mM $[\text{Ru}(\text{NH}_3)_6]\text{Cl}_3 + 0.1 \text{ M KCl}$ at a scan rate of 0.1 V s^{-1} show the permeability before and after the formation of an insulating PPh film, b) enlarged scale of CVs at $\text{PPh}/\text{AuNP}/\text{ITO}_{\text{APTES}}$ and PPh/ITO .

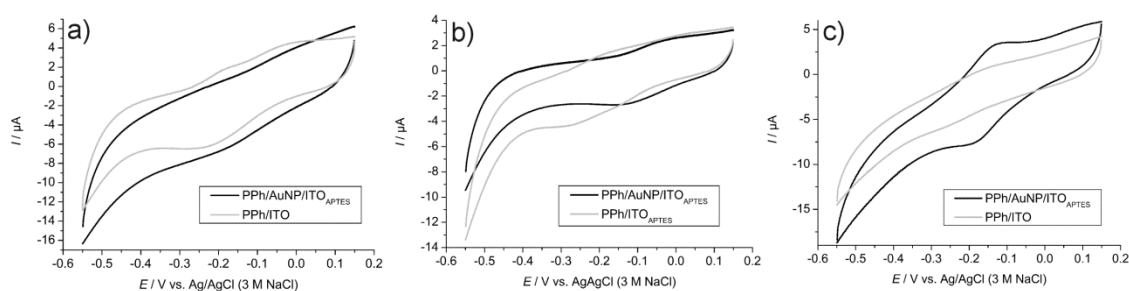


Figure 55. Three examples a), b) and c) of CVs recorded in 1 mM $[\text{Ru}(\text{NH}_3)_6]\text{Cl}_3 + 0.1 \text{ M KCl}$ at a scan rate of $v = 0.1 \text{ V s}^{-1}$ show the permeability at $\text{PPh}/\text{AuNP}/\text{ITO}_{\text{APTES}}$ (black curve) and PPh/ITO (grey curve).

In order to support the findings described above, a further attempt was made to discriminate between the overlapping electrochemical signals for the phenol electrodeposition obtained at AuNP/ITO_{APTES}. The deposition of PPh was carried out in two steps, first in the potential range of 0-0.9 V in which the deposition of PPh is expected on AuNPs and, subsequently, in the potential range of 0-1.8 V in which the deposition of PPh occurs at ITO_{APTES} (Fig. 56).

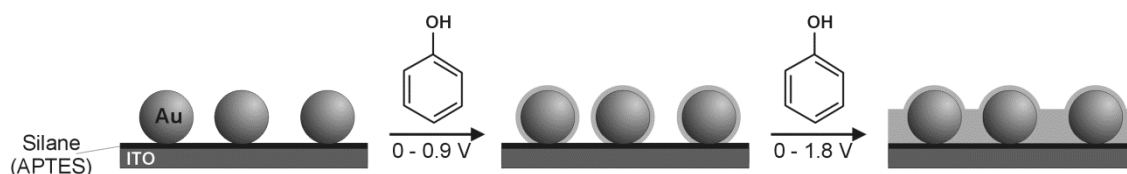


Figure 56. Schematic illustration of the electropolymerization process of phenol at AuNP/ITO_{APTES}: a) PPh deposition at AuNPs within the potential range of 0 V to 0.9 V and b) electropolymerization of phenol at the ITO_{APTES} surface within the potential range of 0 V to 1.8 V.

Figures 57 and 59 show the CVs for two different events measured on AuNP/ITO_{APTES} samples. The first CV in Fig. 57 was prepared by 30 cycles within the potential range of 0-0.9 V in an aqueous solution containing 50 mM phenol + 0.1 M NaH₂PO₄. The first cycle shows an irreversible anodic peak at 0.75 V, which disappears almost completely in the second cycle (Fig. 57). Such behavior is reminiscent of that typically observed during the electropolymerization of phenol, while an onset potential of 0.60 V points towards the formation of an insulating PPh layer at AuNPs.

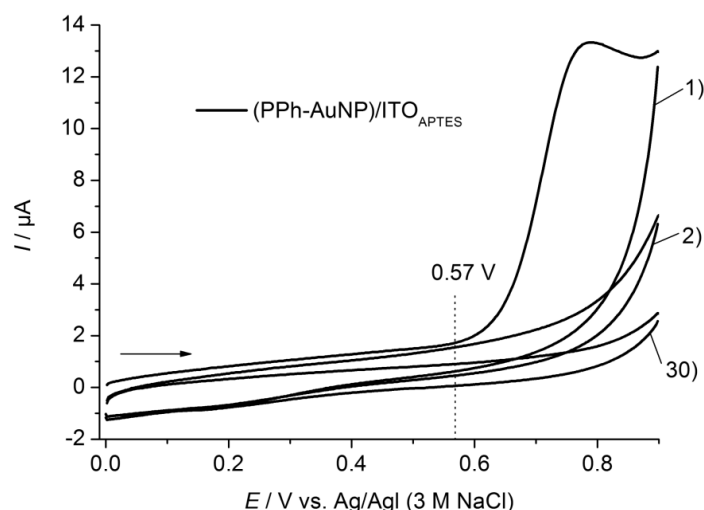


Figure 57. The 1st, 2nd and 30th CV for the electropolymerization of phenol in an aqueous solution containing 50 mM phenol + 0.1 M NaH₂PO₄ at $v = 50 \text{ mV s}^{-1}$ with a scan rate of 0.05 V s^{-1} at AuNPs within the potential range of 0.0 V to 0.9 V.

CVs of $[\text{Ru}(\text{NH}_3)_6]^{3+}$ show still a well-developed quasi-reversible CV for the redoxactive probe (Fig. 58a, black curve) comparable to that obtained at bare AuNP/ITO_{APTES}. This indicates that the polymer does not block the ITO surface. This result was also supported by SFM thickness measurements. There was no characteristic pattern after scratching the sample surface with an SFM tip at high loading forces, which would remove a soft polymer covering the ITO surface (comparable to Fig. 13).

The dissolution of AuNPs in 3 M KCl was not observed at all or barely detectable in LSV (Fig. 58b). This indicates the PPh deposition occurred on the AuNP but not on the ITO surface within a potential range of 0 V to 0.9 V. This situation is shown schematically in Fig. 56. SFM images represent a surface topography consisting of spherical structures with a diameter of 20 to 30 nm. Obviously, the particle sizes remain almost unchanged after the deposition of the polymer. This result is not unexpected, since previous thickness measurements by SFM of PPh films on bare Au/glass electrodes revealed that polymer film stopped growing on gold at thicknesses of 1-2 nm. Such small changes in size cannot be verified by SFM on strongly curved surfaces and due to the broad size distribution of the used AuNPs.

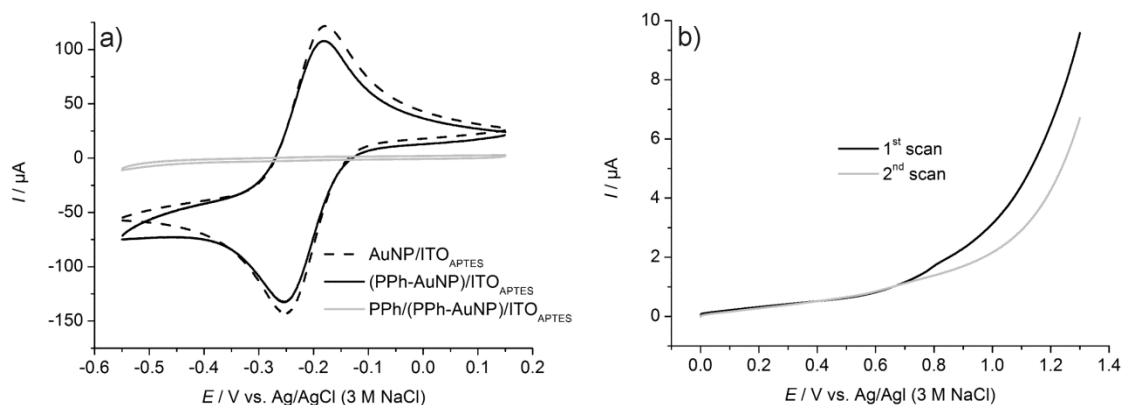


Figure 58. CVs recorded in 1 mM $[\text{Ru}(\text{NH}_3)_6]\text{Cl}_3 + 0.1 \text{ M KCl}$ at a scan rate of 0.1 V s^{-1} show the a) permeability before ($\text{AuNPs}/\text{ITO}_{\text{APTES}}$) and after both events namely the deposition of PPh at AuNPs ($(\text{PPh-AuNPs})/\text{ITO}_{\text{APTES}}$) and the ITO surface ($\text{PPh}/(\text{PPh-AuNPs})/\text{ITO}_{\text{APTES}}$) and b) LSV for the electrochemical release of templates in 3 M KCl solution with a scan rate of 10 mV s^{-1} after AuNP encapsulation.

After the formation of polymer-encapsulated AuNPs at $\text{ITO}_{\text{APTES}}$, further 30 voltammetric cycles were performed at the same electrode area but within a broader potential range of 0 V to 1.8 V (scheme in Fig. 56). There is a distinct oxidation peak in the first CV reaching its maximum at 1.5 V (Fig. 59), which disappears almost entirely in the second scan.

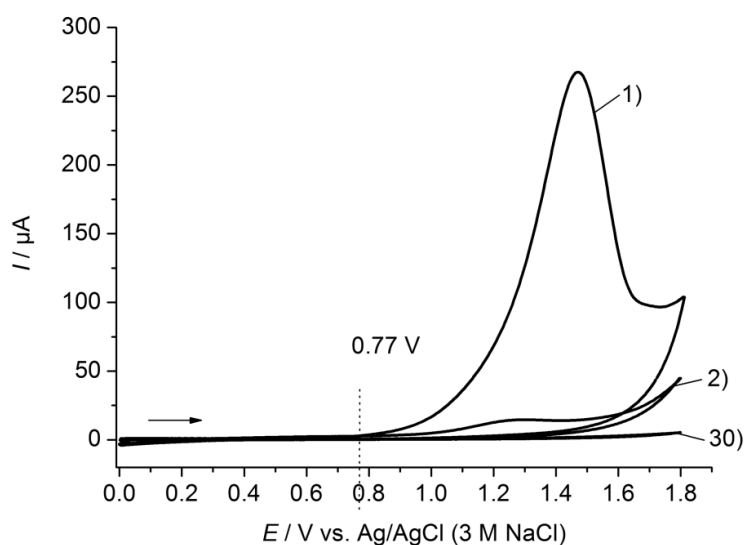


Figure 59. The 1st, 2nd and 30th CV for the electropolymerization of phenol in an aqueous solution containing 50 mM phenol + 0.1 M NaH_2PO_4 at $v = 50 \text{ mV s}^{-1}$ at the $\text{AuNP}/\text{ITO}_{\text{APTES}}$ surface within the potential range of 0.0 V to 1.8 V.

This rapid and drastic decrease in current density results from the deposition of a PPh film at ITO_{APTES} blocking the ITO surface in agreement with CV characteristics previously observed during the formation of an insulating PPh film on ITO_{APTES} electrodes (Fig. 48b); just the onset potential is slightly different (0.77 V, Fig. 59). The insulating properties of these samples were verified by the absence of current response in CVs obtained in [Ru(NH₃)₆]^{3+/2+} (Fig. 58a, grey curve). Accordingly, SFM thickness measurements in the contact mode revealed the presence of a 20 nm thick polymer film on the ITO_{APTES} support.

The topographical images in the SFM contact mode of the surface confirm the presence of AuNPs inside the PPh matrix (Fig. 60). The amplitude and the phase response in Fig. 60 are reminiscent of the model presented in Fig. 56b.

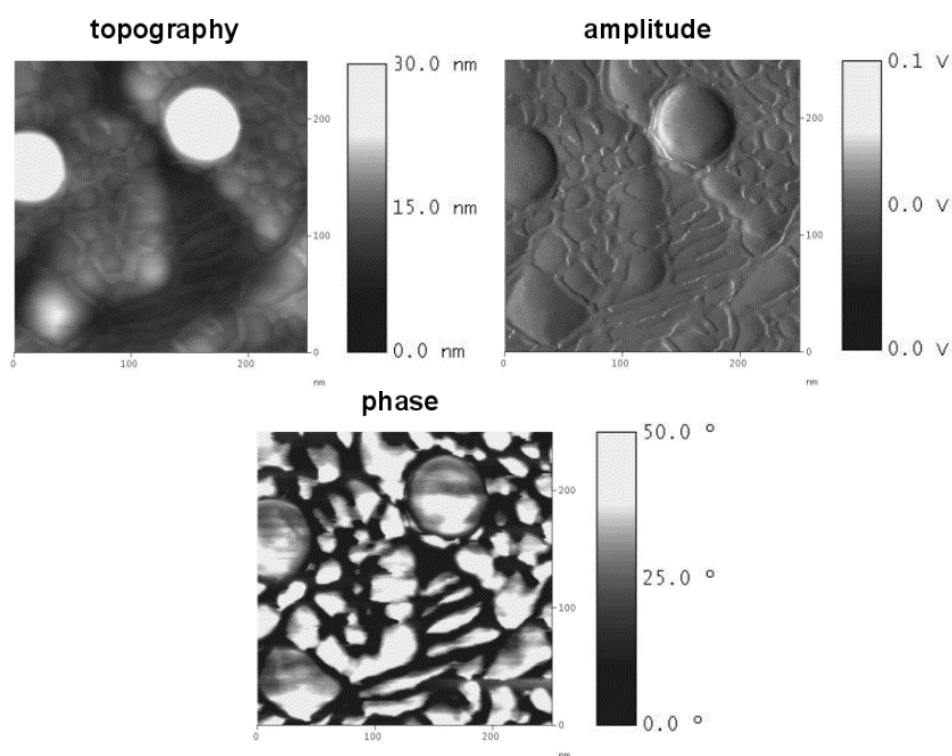


Figure 60. SFM contact mode images (scan area: 250 nm × 250 nm) recorded with the MSCT SFM tip ($k = 0.6 \text{ M m}^{-1}$) at a scan rate of 1.0 Hz and with a resolution of 256 × 256 pixels of samples after PPh layer formation on AuNPs and subsequently on the surrounding ITO surface show the topography as well as the amplitude and phase response (256 × 256 pixels).

In an attempt to remove metal AuNPs from the polymeric PPh matrix by LSV in 3 M KCl stripping solution, the gold oxidation peak was occasionally observed in the potential range of 0.8 to 1.1 V (Fig. 61a). Scans were performed until no further metal oxidation was detected. SEM and SFM images after the electrochemical treatment showed an unchanged composite film. The templates were still located within the PPh matrix. This is probably observed because the insulating PPh film covering the AuNPs prevents the chloride access to the AuNPs, and thus the dissolution of gold cannot proceed. Often, only an increase of the background charging current can be measured (Fig 61b, 1st scan), while an Au-oxidation peak is completely absent. In the second scan the charging currents are strongly diminished and remain at a consistent baseline in further scans.

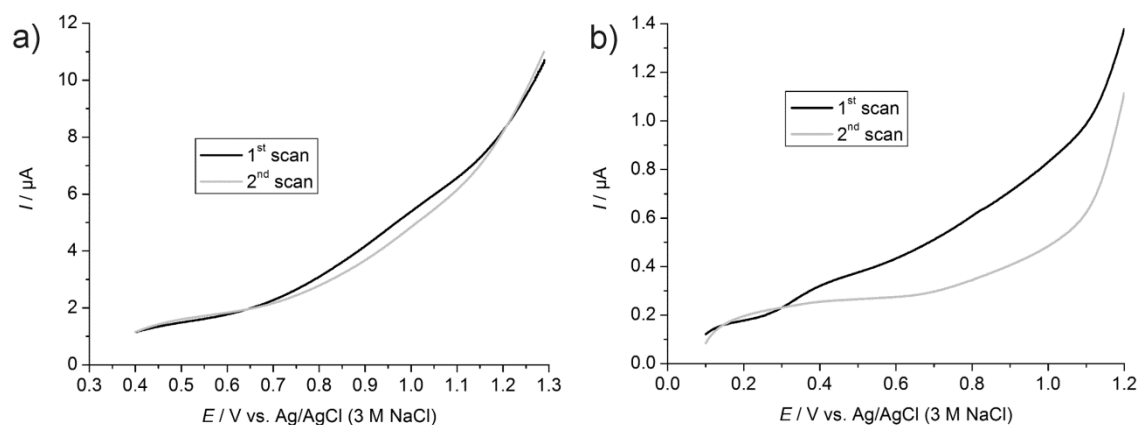


Figure 61. LSVs for the electrochemical release of template AuNPs from PPh/AuNP/ITO_{APTES} samples in 3 M KCl solution with a scan rate of 10 mV s⁻¹. Panels a) and b) show two different examples.

As an alternative route, the chemical oxidation of AuNPs was attempted by a treatment of NIPs in aerated 6 mM KCN based on the assumption that the thin layer covering the AuNPs might be permeable to cyanide ions and oxygen and that the Au cores can be dissolved^[282] according to Eq. (27) while maintaining a stable matrix.



As evidenced by SEM images in Fig. 62, template AuNPs were indeed completely removed, leaving their shape and size imprinted in the polymer. The size of the nanovoids is similar to the diameter of the template AuNP (~30 nm). Due to the broad size

distribution of the used AuNPs (compare Fig. 37), larger nanovoids with diameters of 46.6-55.1 nm could be observed in Fig. 62a.

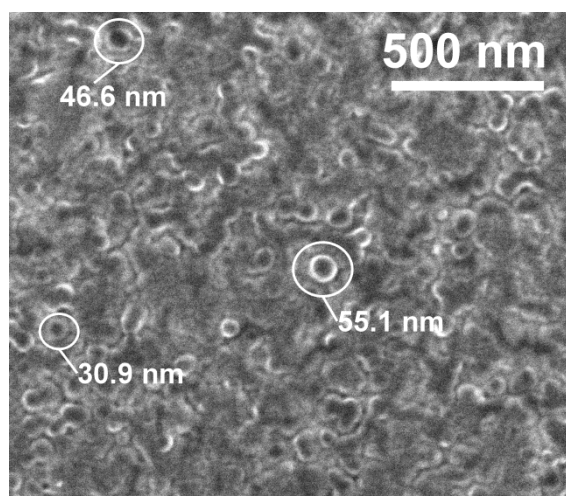


Figure 62. SEM image of the PPh matrix (PPh/ITO_{APTES}) after the chemical removal of AuNP templates over 3 h in aqueous 6 mM KCN solution (white arrows indicate a selection of the imprinted nanovoids).

XPS spectra confirm the complete removal of template AuNPs (Fig. 63). Figure 63 shows the Au 4f spectra measured before (AuNP/ITO_{APTES}) and after (PPh/AuNP/ITO_{APTES}) the formation of a PPh matrix, as well as after the chemical removal of gold templates in 6 mM KCN solution (PPh/ITO_{APTES}). The Au 4f_{7/2} signal is observed at a binding energy of $E_B = 83.35$ eV. After PPh deposition, the overall intensity of the Au 4f signal was greatly diminished to about 19%. The appearance of a signal shift to higher binding energy $E_B = 85.23$ eV indicated the presence of gold in higher oxidation states often described as mixed oxides of Au^I and Au^{III} species.^[243] This signal completely disappears after treating the sample in KCN solution.

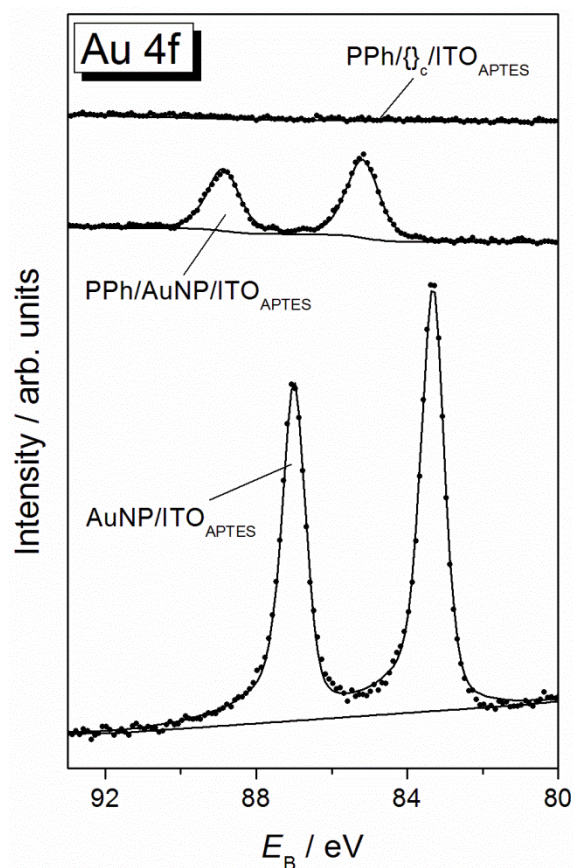


Figure 63. XPS spectra measured at $\text{AuNP}/\text{ITO}_{\text{APTES}}$ before and after $(\text{PPh}/\text{AuNP}/\text{ITO}_{\text{APTES}})$ the formation of a PPh matrix, as well as after the chemical removal of gold templates in 6 mM KCN solution $(\text{PPh}/\{\}c/\text{ITO}_{\text{APTES}})$.

After the removal, the thickness of the polymer film was determined by SFM to be 22 nm (Appendix, Table C1c), which is similar to the thickness before template removal. The film morphology is preserved which is a prerequisite for a stable matrix. Additional information about the morphology after the template removal was obtained by pulsed-force microscopy (PFM). Topographical measurements allow comparison of the height profiles inside and outside the cavities (Fig. 64a). Indeed, a depth profile shows cavities with a depth of approximately 5 nm and less. This observation does not necessarily suggest open cavities, since the polymer around the particles has a thickness of about 20 nm. It could rather mean that the polymer layer surrounding the AuNP became a closed nanovoid that collapsed after template removal as shown schematically in Fig. 65a. Alternatively, the SFM tip may not have reached the ITO surface due to its much larger tip curvature radius compared to the AuNPs-formed cavities (Fig. 65b). In

this case the depth of recessed features on the surface cannot be reproduced faithfully. Kékicheff et al.^[283] reported the same problem when trying to investigate the cyanide-induced dissolution of AuNPs contained in polyelectrolyte multilayers by SFM and TEM.

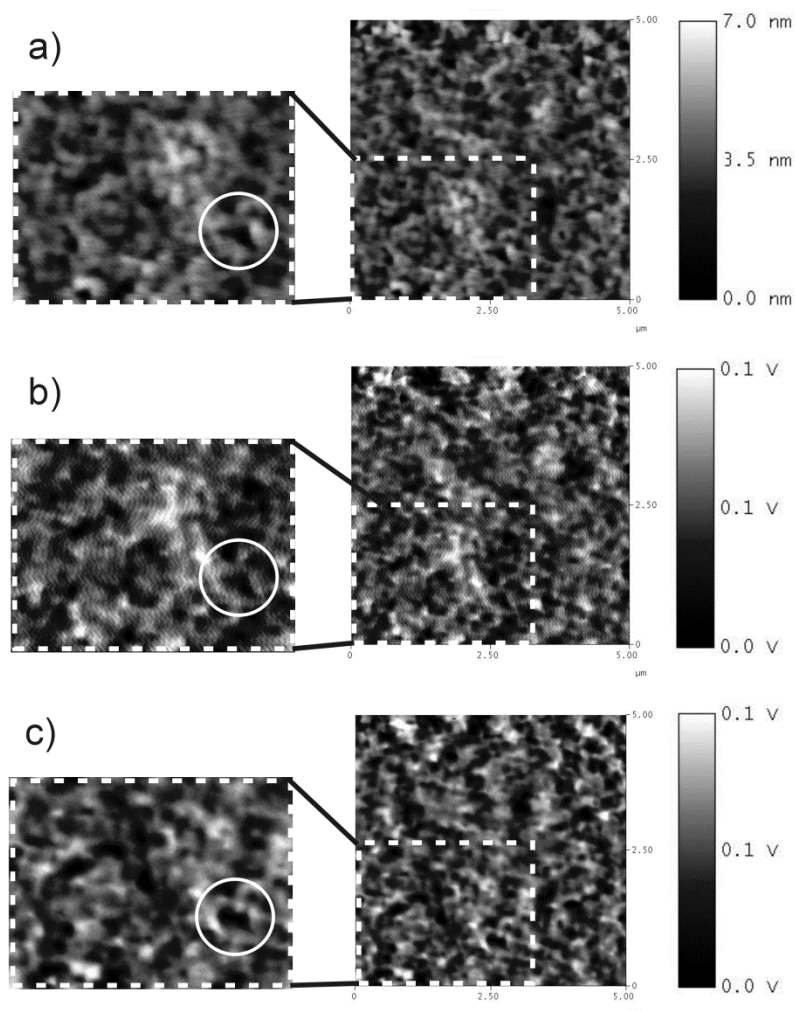


Figure 64. SFM images ($5\ \mu\text{m} \times 5\ \mu\text{m}$ and enlarged subsections of $2.5\ \mu\text{m} \times 3.5\ \mu\text{m}$) recorded in the pulsed-force mode show a) the topography of the NIP after chemical removal of the template AuNP and the corresponding adhesion b) and stiffness c) images. In contrast to a) and b), the template-formed features in the polymer are clearly recognizable in c) as black, well defined spots (marked by a white circle).

Additionally, Fig. 65 suggests using a redox active probe to obtain further information about the architecture of the matrix. In case of closed nanovoids no electron transfer is expected (Fig. 65a), while open cavities need an active area to enable the electron transfer (Fig. 65b for electron transfer enabled and 65c for electron transfer disabled). This issue is discussed in detail below (see Fig. 66).

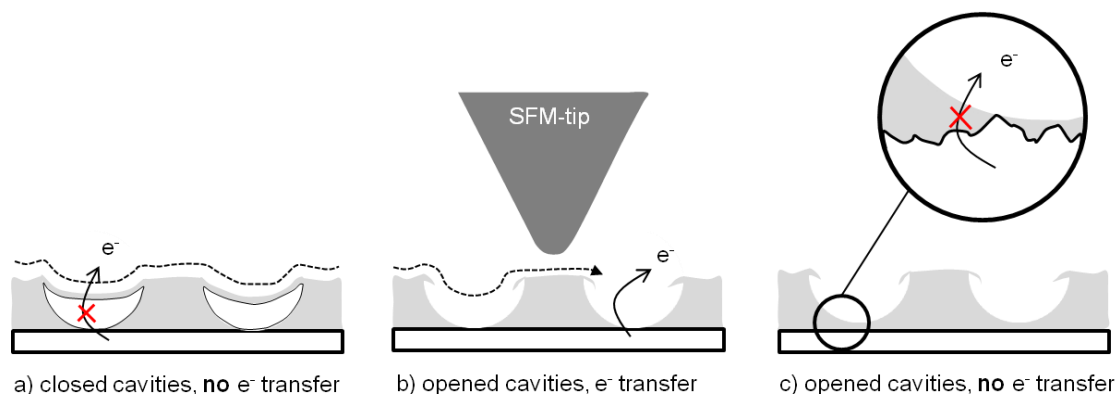


Figure 65. Schematic illustration of three different architectures a), b) and c) suggested for template-formed features after exposing NIPs to KCN etching solution: a) represent a close nanovoid preventing an electron transfer, b) and c) represent open cavities either enabling the electron transfer or preventing it due to the formation of an insulating polymer layer between template NPs and the ITO electrode. The SFM tip section profiles point out that open and closed holes are difficult to distinguish.

However, the PFM measurements did not only provide topographical images but also spatially correlated information about the material properties such as the local adhesion and stiffness of the surface. These features have rendered PFM useful for the investigation of self-assembled silane monolayers on SiO_2 ,^[44] for characterization of polymers,^[284, 285] surfaces with different charges^[286] as well as biological cells.^[287] It was expected that the oscillation parameters of the cantilever are greatly affected by the slight differences of adhesion and stiffness between nanovoids and the polyphenol matrix. Since several factors influence the adhesion between SFM tip and surface (attractive and repulsive interactions, electrostatic charges, capillary forces), there is no ubiquitous measure for adhesion. Hence, it is very difficult to interpret the resulting image contrast in Fig. 64b and assign it to the corresponding cavities. The definition of the contrast obtained in the stiffness images is much easier since it is given by the relative tendency of the materials to deform reversibly under applied loading. The template-formed features in the polymer are clearly recognizable as black, well defined spots in Fig. 64c, quite different from the topography and adhesion images (compare surface feature marked with the white circle).

Better insight was possible by monitoring changes in the electrode response of $[\text{Ru}(\text{NH}_3)_6]^{3+}$ ions as redox probe before and after the template removal. The detection of

reversible $[\text{Ru}(\text{NH}_3)_6]^{3+/2+}$ redox couples is required to confirm the formation of open cavities (Fig. 65b). This would allow the redox probe to be transported directly to the electrically conductive ITO surface. The voltammetric response may result in peak-shaped or in sigmoidal CVs with a diffusion-limited current. The latter behavior will be in agreement with the reaction at a microelectrode array in which the diffusion layers at each element does not overlap within the recording time of the CV.^[219] If the array elements are more closely spaced, the individual diffusion layers from each redox-active point overlap to a macroscopic diffusion layer within the recording time of the CV. The response would be that of a quasi-reversible system of a macroscopic electrode. Following the electrochemical route to remove gold templates from the polymeric matrix, small changes in voltammetric response are observed compared to the untreated PPh/AuNP/ITO_{APTES} samples. After exposing NIPs to KCN solution over 3 h the current is slightly enhanced and show a clear signature of redox reactions of $[\text{Ru}(\text{NH}_3)_6]^{3+/2+}$ at PPh/{}_c/ITO_{APTES} in Fig. 66, grey curve. This result points towards the formation of only a few open nanocavities after template removal (mixture of Fig. 65b and c). This creates unfavorable conditions for the electrochemical detection of NPs after reuptake. Based on the steady-state diffusion-limited current j_D (Fig. 66, grey curve), it is possible to estimate the number of open cavities at the electrode surface. This approach has been also used for PDMS based NIPs in Chapter 5.2 [Eq. (17-19)]. NIPs were considered as randomly arranged microelectrodes that behave like independent recessed microelectrodes. Equation (Eq. 17) gives the total current density, which is expected if all nanocavities are open and can be considered as recessed nanoelectrodes. The number of NPs $\Gamma_{\text{NP}} = 4.23 \cdot 10^9 \text{ NP cm}^{-2}$ was determined from counting NP densities in SFM images (Fig. 53b). Due to the spherical shape of the template (30 nm in diameter), the active area is expected to be much smaller than the diameter of one NP, e.g. only 1.5 nm. Under this assumption about 5% of the cavities are open. This calculation is considerably simplified, but it provides the order of magnitude. The calculated removal efficiency value is associated with an uncertainty originating from limited precision in counting the NP surface concentration from microscopic images (inhomogeneity of NP surface concentration over t extended sample areas outside the analyzed field of view) and the estimation of the average area of the recessed nanoelectrode.

As SEM images indicate open holes, another critical situation might exist in which the lack of the redox-response for $[\text{Ru}(\text{NH}_3)_6]\text{Cl}_3$ is caused by the formation of an insulating polymer layer at the interface between template AuNPs and the relatively rough ITO electrode surface schematically shown in Fig. 65c. Even if analyte NPs can be captured in opened nanocavities, the electrochemical detection and discrimination between NPs in imprinted cavities and non-specifically adhering NPs would be a problematic task due to the lack of an ohmic contact between analytes and the electrode surface.

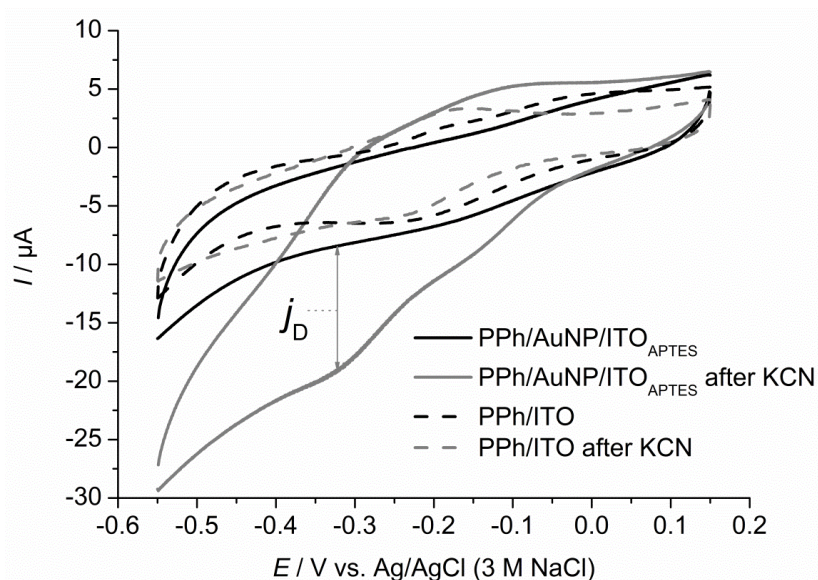


Figure 66. CVs recorded in 1 mM $[\text{Ru}(\text{NH}_3)_6]\text{Cl}_3$ + 0.1 M KCl at a scan rate of 0.1 V s^{-1} showing the permeability at PPh/AuNP/ITO_{APTES} (black line) and b) PPh/ITO before (black dashed line) and after (grey line for PPh/AuNP/ITO_{APTES}, grey dashed line for PPh/ITO) exposing samples to aqueous 6 mM KCN solution over 3 h.

As a control experiment, a PPh/ITO sample was exposed for 3 h to 6 mM KCN etching solution and a CV in the probe solution was recorded (Fig. 66, grey dashed curve). Small cathodic and anodic peak currents are clearly observed in CVs obtained after sample treatment. Most likely this behavior is associated with a swelling of the PPh film and an enhancement of its permeability. Further permeability tests at PPh/AuNP/ITO_{APTES} and PPh/ITO before and after KCN treatment show reproducible results (Appendix, Fig. C3).

It is important to ensure that no gold residues remain in the polymeric matrix. This could potentially distort the recognition ability of NIPs. To this end, LSV experiments were conducted at PPh/{}_c/ITO_{APTES} and PPh/ITO in 3 M KCl gold stripping solution (Fig. 67).

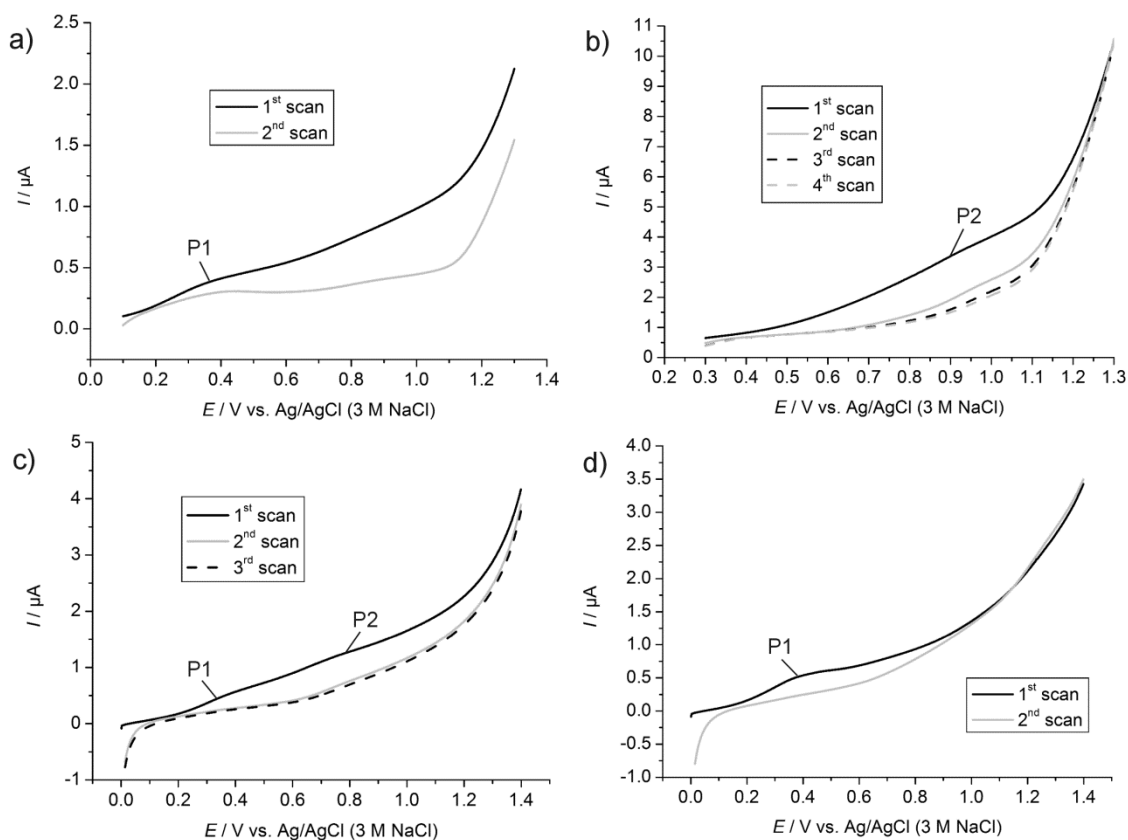


Figure 67. LSVs recorded in 3 M KCl solution at a scan rate of 10 mV s^{-1} at a) - c) PPh/{}_c/ITO_{APTES} and d) PPh/ITO after exposure to 6 mM KCN over 3 h.

The first voltammetric scan typically shows an increase of the background charging current and the appearance of two weak peaks. One is located between 0.2 V and 0.4 V (Fig. 67a, 1st and 2nd scan, P1) and the other between 0.6 V and 1.1 V (Fig. 67a, 1st scan, P1). Both peaks occur independently and without any regularity. Sometimes a broad peak between 0.2 V and 1.1 V may result from the overlap of both signals (Fig. 67c, 1st scan, P1/P2). The peak P1 was occasionally observed in LSV control experiments in 3 M KCl stripping solution at KCN-treated PPh/ITO samples (Fig. 67d, 1st scan P1). This proves that this signal is not due to gold oxidation. However, the assignment of this

peak remains open. The peak P2 was only observed on samples that originally contained AuNP, but not at PPh/ITO. It is therefore assigned to the gold dissolution.

In order to prove the stability of ITO layers in KCN solution, clean samples were exposed to the etching solution for 3 h while electroactivity was tested before and afterwards by cyclic voltammetry of $[\text{Ru}(\text{NH}_3)_6]^{3+}$. An unchanged quasi-reversible CV with current densities comparable to that obtained for untreated ITO samples indicates an intact ITO surface after KCN treatment (Fig. 68).

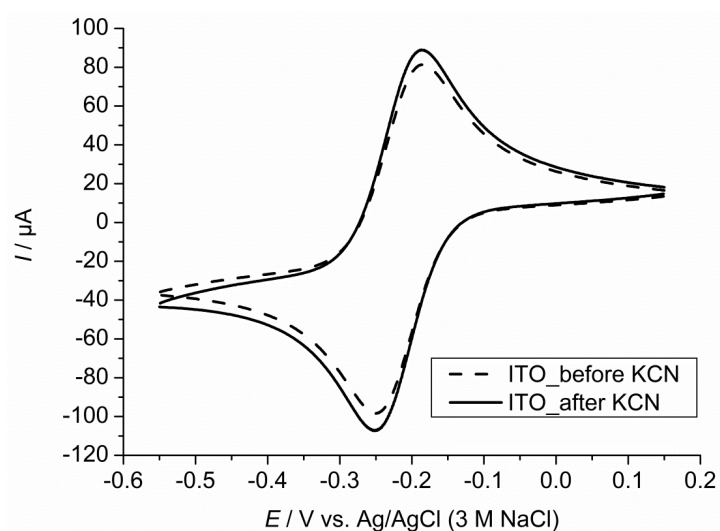


Figure 68. CVs recorded in 1 mM $[\text{Ru}(\text{NH}_3)_6]\text{Cl}_3$ + 0.1 M KCl at a scan rate of 0.1 V s^{-1} at a bare ITO electrode before (black dashed line) and after (black line) exposing it to 6 mM KCN etching solution over 3 h.

Different to the previous approach (Chapter 5.4), the recognition ability and size selectivity of PPh-based NIPs was analyzed by a competitive uptake of 20 nm AgNPs via 50-nm AuNPs (Fig. 69). Since the templates leave imprinted cavities of 30 nm, it was expected that a AgNP can find its way more easily into the cavity as the larger AuNP. The presence of electrochemically addressable analyte NPs was verified by LSV in aqueous 0.1 M NaNO_3 solution for AgNPs and in 3 M KCl solution for AuNPs.

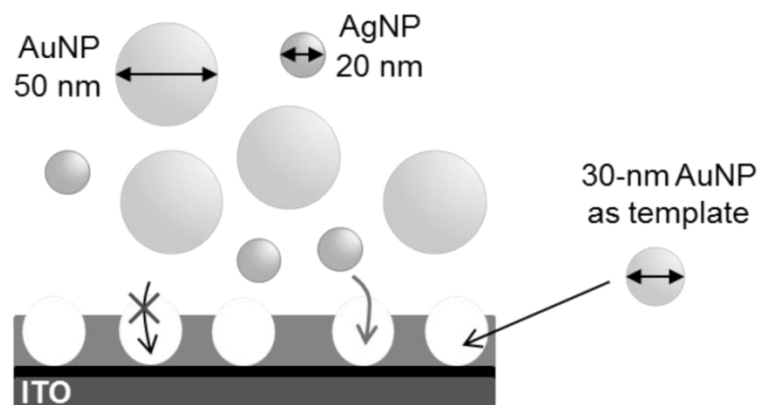


Figure 69. Schematic representation of the competitive reuptake of 20 nm AgNPs via 50 nm AuNPs using the PPh-based NIP with cavities of 30 nm.

The recognition ability and size selectivity of NIPs $\text{PPh}/\{\}\text{c}/\text{ITO}_{\text{APTES}}$ was investigated by immersing it for 15 h in aqueous solutions containing citrate-capped analyte AgNPs of 20 nm and AuNPs of 50 nm in diameter. These two NP populations were mixed with a ratio between the number of NPs of 1:1. In case of open cavities, a significantly higher uptake capability towards 20-nm particles was expected since they are more similar in size to the templates than the 50-nm AuNPs. The presence of electrochemically addressable analyte AgNPs was verified by LSV in aqueous 0.1 M NaNO_3 solution (Fig. 70a). The oxidation of silver using 0.1 M NaNO_3 as the silver stripping solution^[191] follows the reaction given in Eq. (28).



In two of the samples, a well-developed peak at +0.23 V is detected in the first scan, while in the following scans the peak shifts to lower values (+0.2 V). These peaks are clearly assigned to the electrochemical dissolution of AgNPs. The redox potential is sufficiently different from the oxidation peak potential of template AuNP (+0.8 V in Fig. 41). Similar to AuNPs, the analyte AgNPs are not completely oxidized in one LSV scan. After successive LSV scans, no remaining addressable AgNP was detected. Two other examples did not show an uptake and/or detection of analyte NPs. The detection of analyte AuNPs was performed in aqueous 3 M KCl solution (Fig. 70b). The characteristic gold oxidation signal was not observed. But in some examples the increase of the background charging current in the first scan is accompanied by a broad peak located in

the potential range between 0.5 to 1.1 V. This signal was associated with the dissolution of residual gold within the matrix after KCN-etching as shown above (Fig. 67b). But even if the matrix was previously electrochemically treated to remove gold residues, this peak is still detectable after the analyte uptake process. No current response was detected in the 3rd sweep (Fig. 70b).

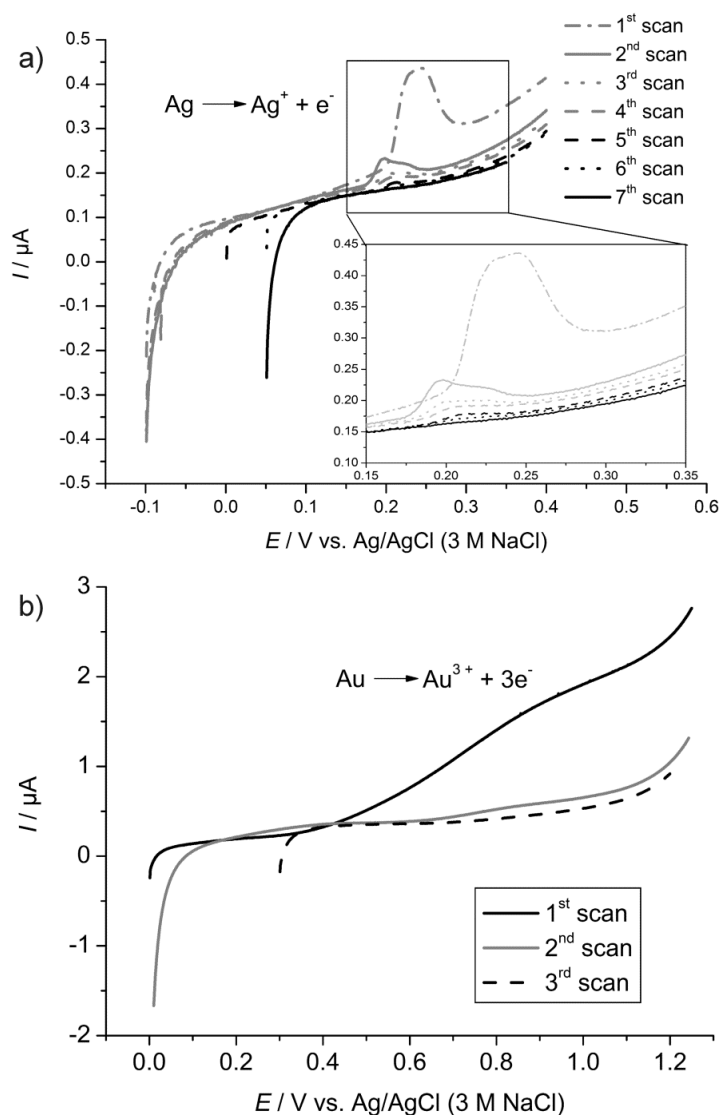


Figure 70. LSVs recorded in a) 0.1 M NaNO₃ and in b) 3 M KCl solution at PPh/ITO_{APTES} after exposing samples to an aqueous solutions containing citrate-capped analyte AgNPs and AuNPs (20 nm and 50 nm in diameter) for 15 h.

For control experiments, non-imprinted PPh layers were initially exposed to the analyte NP solution in the same manner as NIPs, and subsequently tested in stripping solutions. Surprisingly, LSV experiments in 0.1 M NaNO₃ reveal electrooxidation signals

corresponding to the dissolution of AgNP as well (Fig. 71a). A distinct Ag-oxidation peak appears at +0.21 V in the first scan and shifts to lower values (+0.15 V) in the following. Similar to NIP-covered samples, this result was reproduced in two out of four samples.

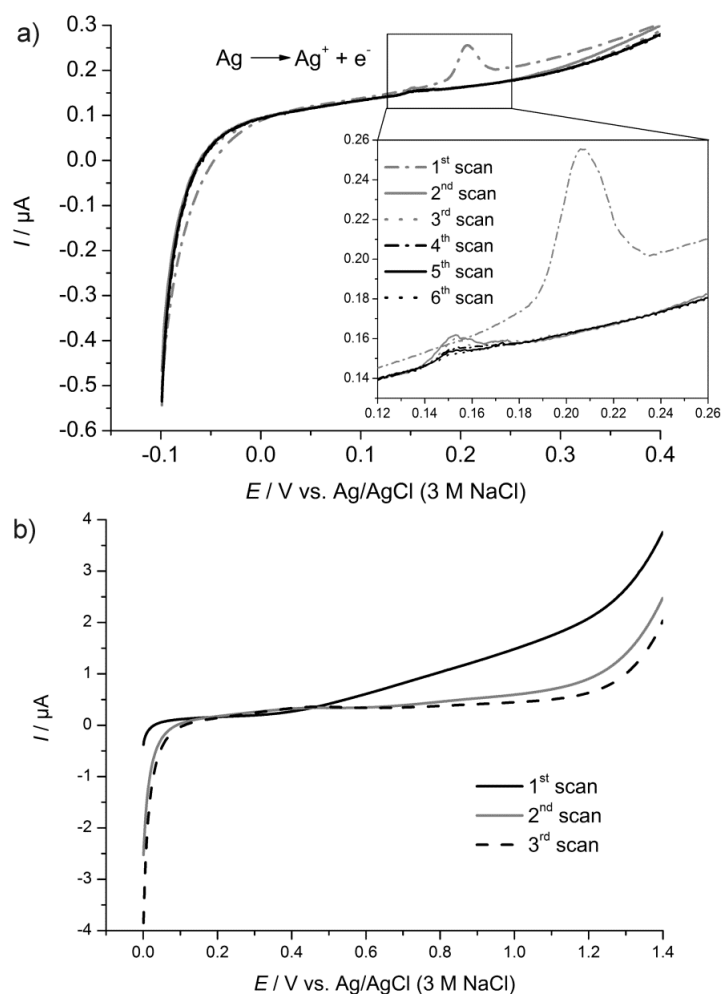


Figure 71. LSVs recorded in a) 0.1 M NaNO_3 and in b) 3 M KCl solution at PPh/ITO after exposing samples to an aqueous solutions containing citrate-capped analyte AgNPs and AuNPs (20nm and 50 nm in diameter) for 15 h.

The process for the oxidation of AuNPs has not been found by LSV measurements in 3 M KCl solution, but the increase of the background charging current is still visible in some experiments (Fig, 71b). A further control experiment, in which a bare ITO sample was exposed to the uptake solution and subsequently tested in stripping solutions, showed that no interaction occurred between analyte NPs and the untreated ITO surface.

Characterization of the uptake process using SEM and SFM show a similar outcome. All samples with a detectable electrochemical dissolution of the AgNPs indicate a strong attachment of analyte NPs to the PPh film, while the amount of 20-nm AgNPs (Fig. 72a, labelled with 20.4 nm) is clearly higher than that of 50-nm AuNP (Fig. 72a, labelled with 56.5 nm).

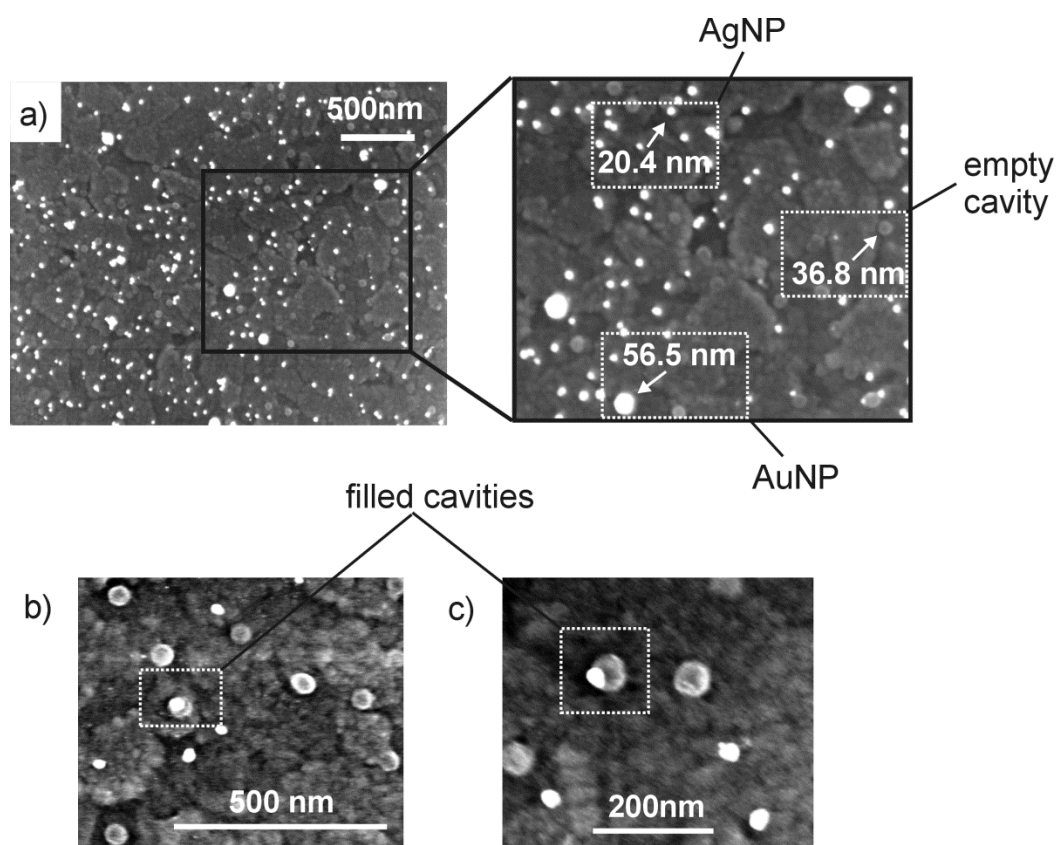


Figure 72. a) SEM image recorded at 20 kV of PPh/ITO_{APTES} after immersing it in aqueous solutions containing citrate-capped analyte AgNPs and AuNPs (1:1) for 15 h. The enlarged view of selected area shows AgNPs (20.4 nm), AuNPs (56.5 nm) and template-formed features (36.8 nm). SEM images recorded at 15 kV show analyte AgNP in the center b) of template-formed feature and at its edge c).

The main difference between imprinted and non-imprinted layers is that the imprinted layers additionally consist of the template-formed features (Fig. 72a, labelled with 36.8 nm). Most of the AgNPs were randomly arranged on the NIP surface. They are rarely found in the center of features supposed to be nano voids (Fig. 72b). Some AgNPs show a tendency to be attached to the edges of these features (Fig. 72c). SEM investigations show a lower amount of analyte NPs on the NIP surface after the

electrochemical detection of AgNPs and AuNPs (Fig. 73). Almost all of the remaining particles are reduced in size, yet some retain their original size.

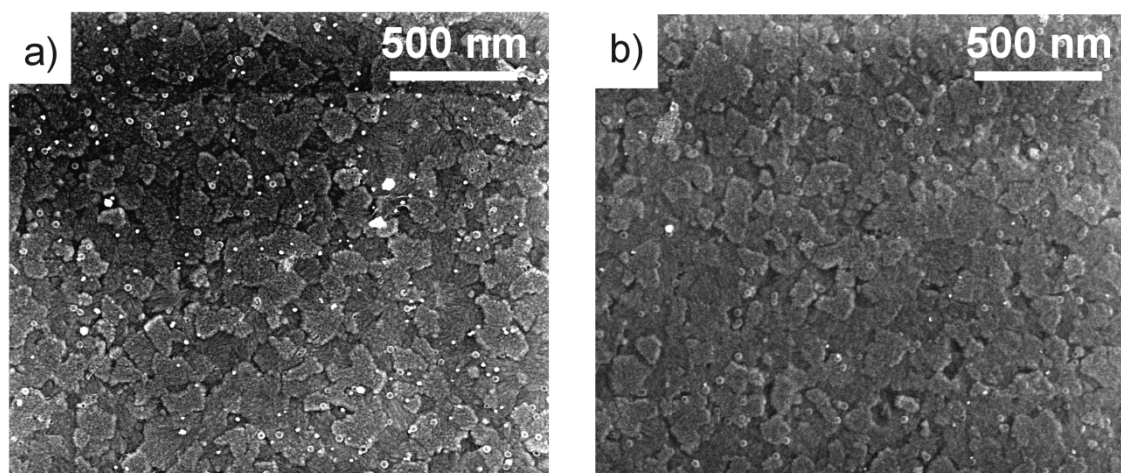


Figure 73. SEM image recorded at 15 kV of PPh/ITO_{APTES} a) before and b) after electrochemical detection of analyte AuNPs and AgNPs.

In Fig. 74 a SFM image of the surface shows the various features, which are also observed during previous SEM measurements. The template-formed features could be best visualized when choosing a height range of 5 nm (Fig. 74a), while the ring-shaped structure is not always well pronounced. The values obtained for the size and the depth are in agreement with values obtained by SEM (Fig. 62, size: 40-55 nm) and PF-SFM (Fig. 64, height: ≤ 5 nm) measurements. Using a scale-bar of 20 nm gives a better view of larger structures (Fig. 74b). The size of NPs ranges between 3.6-37.6 nm, with a clear tendency to be decreased to sizes between 8.8-15.2 nm after electrooxidation. The high magnification SFM image represents more detailed surface features than SEM (Fig. 74c). So far, the reason for the incomplete stripping is unknown. But it is assumed that the NPs might lose the electrical contact to the electrode surface during the oxidation and thus remains undissolved.

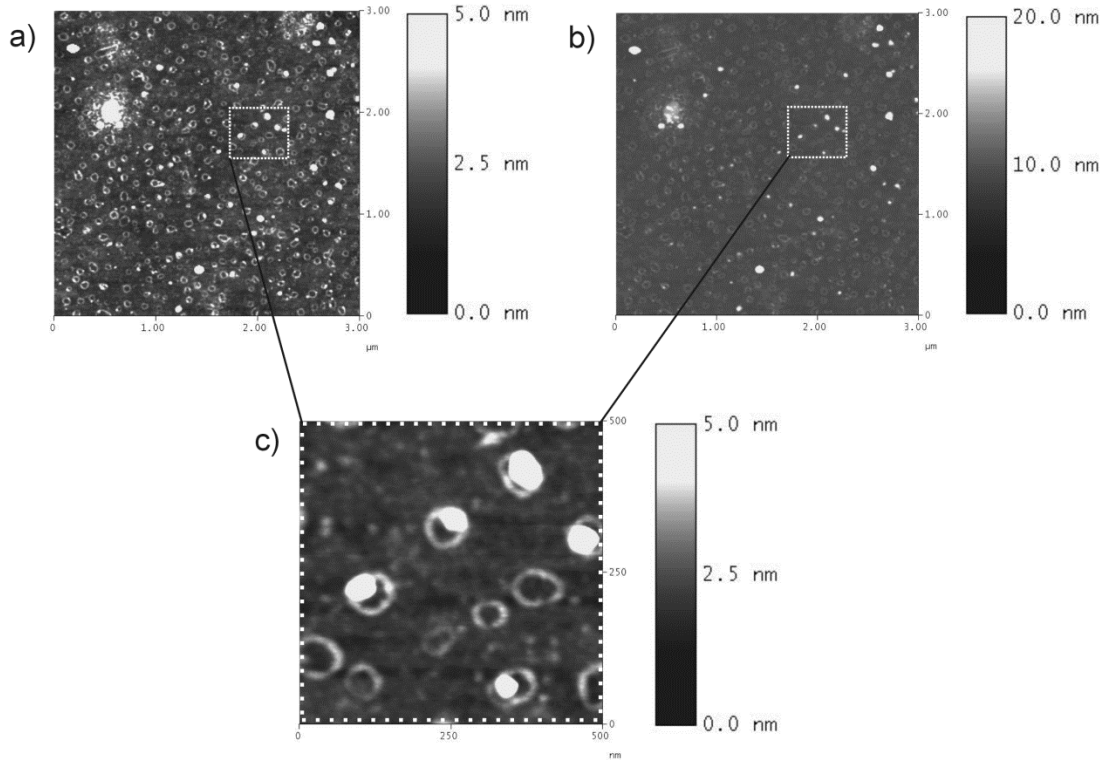


Figure 74. SFM images recorded in the intermittent mode at a scan rate of 1.0 Hz show the topography of the NIP after electrochemical detection of analyte NPs at a scale bar of a) 5 nm and b) 20 nm in a scan area of 3 $\mu\text{m} \times 3 \mu\text{m}$. An enlarged view of a selected (0.5 $\mu\text{m} \times 0.5 \mu\text{m}$) area of a) and b) is shown in c) at scale bar of 5 nm.

Another possibility would be that the AgNPs have a larger diffusion coefficient than the AuNPs, $D_{\text{AgNP}} > D_{\text{AuNP}}$. This effect can be estimated from the Einstein relation [Eq. (29-30)]:

$$D_{\text{AuNP}} = \frac{k_B \cdot T}{6 \pi \eta r_{\text{AuNP}}} \quad (29)$$

$$D_{\text{AgNP}} = \frac{k_B \cdot T}{6 \pi \eta r_{\text{AgNP}}} \quad (30)$$

where k_B is the Boltzmann constant, η is the dynamic viscosity of the dispersion medium, $r_{\text{AuNP}} = 25 \text{ nm}$ is the radius of AuNP, $r_{\text{AgNP}} = 10 \text{ nm}$ is the radius of AgNP.

The ratio of the diffusion coefficient is therefore:

$$\frac{D_{\text{AgNP}}}{D_{\text{AuNP}}} = \frac{r_{\text{AuNP}}}{r_{\text{AgNP}}} = \frac{25}{10} = 2.5 \quad (31)$$

The diffusion coefficient influences the flux $J(t)$ of NPs to a surface. Assuming a diffusion-controlled process, where AgNPs would be most strongly favored over AuNPs, the amount N_{NP} of particles colliding with the NIP surface within the exposure time t is given by the integrated Cottrell equation, where c_{NP}^* is the particle concentration in the bulk:

$$N_{\text{NP}} = \int J(t) dt \quad (32)$$

$$= \int \sqrt{\frac{D_{\text{NP}}}{\pi}} c_{\text{NP}}^* \cdot \frac{1}{\sqrt{t}} dt \quad (33)$$

$$= \int \sqrt{\frac{D_{\text{NP}}}{\pi}} c_{\text{NP}}^* \cdot \sqrt{t} \quad (34)$$

The ratio of the total amount of AgNPs and AuNPs impacting the surface under diffusion-controlled condition is thus

$$\frac{N_{\text{AgNP}}}{N_{\text{AuNP}}} = \sqrt{\frac{D_{\text{AgNP}}}{D_{\text{AuNP}}}} \cdot \frac{c_{\text{AgNP}}^*}{c_{\text{AuNP}}^*} = \sqrt{2.5} \cdot \frac{c_{\text{AgNP}}^*}{c_{\text{AuNP}}^*} = 1.58 \cdot \frac{c_{\text{AgNP}}^*}{c_{\text{AuNP}}^*} \quad (35)$$

As the object concentration of AgNPs and AuNPs in the dispersion is approximately equal, the AgNPs collide with the film only 1.6 times more often. Figure 74 shows that the ratio of bounded AgNPs is much larger than expected from the different diffusion properties of both particle types.

In this part of the work it was successfully demonstrated that electrochemical observation of the release of metal NPs is a very convenient method enabled by matrices of a precisely controlled thickness. As an alternative way for the electrochemical removal of AuNPs, the chemical oxidation using KCN solution was introduced. Furthermore, PPh deposition at AuNP/ITO_{APTES} offers a new way of selective NP coating.

Finally, the reuptake process was expanded to a competitive recognition concept, in which the recognition ability of target NPs was examined from a mixture of two populations of NPs of different size and of different elements, namely AuNPs and AgNPs. The size selectivity of the films was demonstrated as a significantly higher uptake capability was observed towards the 20-nm particles, since they are more similar in size to the templates (~ 30 nm) than the larger 50-nm AuNPs.

7. Summary

The aim of this project was the development of nanoparticle imprinted polymers or matrices for investigating the interaction of NPs with interfaces in analogy to the well-known concept of molecularly imprinted polymers. The matrices were obtained by imprinting organic thin films with NPs that vary in the core material and ligand shell. Upon an extraction of template NPs, complementary cavities were formed, which were used for a selective recognition of analyte NPs. This Chapter summarizes the developed NIP systems and gives a conclusion with suggested direction for future investigations.

7.1 Investigated systems and conclusion

The initial approach for NIP fabrication was focused on the generation of a PDMS-matrix imprinted by OA-stabilized Fe_3O_4 -NPs with a mean diameter of 10 nm (Chapter 5.2). Spin coating was used to form thin layers from a mixture of NPs and PDMS on flat glass and ITO substrates. This technique allowed the formation of Fe_3O_4 -NP thin film composites with thicknesses of 5-8 nm. However, PDMS hardly offers any possibilities to introduce specific interactions for NPs. Furthermore, there was no suitable characterization method available to detect analyte NPs in the film. Therefore, no reuptake studies have been undertaken and this particular system was not further considered.

In the second approach (Chapter 5.3) it was shown that 2D nanocomposites consisting of magnetic Fe_3O_4 -NPs and OA can be successfully transferred to TSG substrates using the Langmuir-Blodgett technique. This sub-monolayer of Fe_3O_4 -NPs could be released from the substrate surface in an external magnetic field of a permanent magnet opening the route for the controlled, local and directed release of specified small quantities of magnetic nanoparticles. The detection of iron oxide NPs in monolayer amounts turned out to be more difficult than expected at least with simple instrumentation. XPS was not promising for particle detection as it was not possible to distinguish between NPs inside cavities and on the surface of the films. Nevertheless, PM IRRAS measurement provides evidence of the presence of the OA monolayer on the TSG substrate after template removal. As the attempts for analyte reuptake failed, it was

assumed that the lateral mobility and flexibility of oleic acid molecules in the matrix reduces the specificity of imprinted cavities and that this system suffers from the lack of a stable matrix after template removal.

In cooperation with the group of Professor Daniel Mandler the first nanoparticle imprinted polymer combined with electrochemical detection was realized (Chapter 5.4). The new sensor principle was successfully demonstrated with a poly(aniline) film transferred simultaneously with template AuNPs by the Langmuir-Blodgett technique onto an indium doped tin oxide substrate. Electron microscopic images after the transfer showed randomly distributed NPs with insignificant agglomeration. As evident by SFM measurements, films consisting of 3 LB layers of PANI and embedded AuNPs have a thickness of 3 nm. The release of the AuNPs could be easily controlled and observed by electrooxidation. In this system, SEM investigations after electrooxidation confirm the formation of open cavities in the film. The recognition ability of the NIPs was examined by inserting the template matrix in an AuNP containing alkaline solution, since the PANI film is neutral at this pH and non-specific electrostatic attractions between the polymer matrix and the negatively charged AuNPs are eliminated. It was possible to show that the cavities are capable to re-capture analyte NPs with size-exclusion behavior. This was accomplished by an electrochemical approach in the same way as used for the release of the template NPs.

The last approach to obtain nanoparticle imprinted matrices was realized by sequential deposition of template and matrix. First, electrostatic self-assembly enabled the organization of randomly arranged AuNPs (30 nm in diameter) on APTES-modified ITO substrates (Chapter 6.1). Subsequently, a thin polymer matrix with a thickness of 19 nm, approximately the size of the used AuNPs, was produced by electropolymerization of phenol (Chapter 6.3). Attempts to remove the AuNPs electrochemically failed, since the insulating poly(phenol) layer passivates the particle and substrate surfaces. As an alternative way to the electrochemical removal of AuNPs, the chemical oxidation using KCN solution was successfully introduced. As evidenced by SEM images, template AuNPs could be completely removed, leaving their shape and size imprinted in the polymer. Finally, the reuptake was processed using a competitive recognition concept in which the recognition ability of target NPs was examined from a mixture of two

populations of NPs of different size and of different elements, namely AuNPs and AgNPs. The size selectivity of the films was demonstrated by a significantly higher uptake capability for the 20-nm particles, since they are more similar in size to the templates (~ 30 nm) than the larger 50-nm AuNPs.

7.2 Conclusion and outlook

In conclusion, this thesis demonstrates two different routes for NIP formation. One can arrange the matrix from small molecular building blocks together with the template NPs in an LB trough or assemble the matrix from polymeric building blocks in between the NPs by electropolymerization. Based on results of this thesis, the sequential deposition of template and matrix is proposed as an ideal way to prepare thin NIPs. This approach allows a controlled release and reuptake of NPs by taking advantage of the interfacial detection scheme. However, a breakthrough in selective recognizing of NPs requires improvements in several interdependent aspects of the system.

The selection of the matrix material and the procedures for their formation are by far the most critical components determining the success of selective recognition of NPs. It is particularly important that the NIP-matrix has a smaller thickness than the diameter of the NPs because thicker films would prevent the access to the solution phase. At the same time, the formed cavity should also be thick enough to enable size exclusion and to provide sufficient area for specific interaction. It was found that polymeric matrices are much more robust than molecular matrices and preserve the shape and size of the cavities after template removal. Electropolymerization of polymers with controllable thicknesses offers an appealing approach to avoid a full coverage of template NPs by the polymeric matrix. Two optional polymers, namely poly(phenol) and poly(plumbagin), were studied in terms of thickness, rigidity and permeability. These experiments showed that plumbagin-based films have the advantage of providing a free adjustment of the film thickness and apparently enable a limited ionic conductivity. However, controlling the thickness was only possible on plumbagin-grafted GC electrodes. A requirement to realize NIP systems in combination with plumbagin-based matrices would be finding a satisfying way to assemble template NPs on grafted plumbagin layers. From the

experience made during the investigations of phenol-based matrices, it is evident that the simultaneous deposition of polymers might occur on the substrate and on the template NPs. This could be prevented if electropolymerization can be guided towards the electrode surface rather than to the NPs by using an appropriate stabilizing shell or a non-conductive core of the template NPs. A preliminary study on assembling SiO₂-coated AuNPs at hydroxyl-terminated GC electrodes was shown in the Master thesis of Anne Staggenborg. Embedding such NPs into poly(plumbagin) films represents an interesting future extension of the NIP concept. However, in case of SiO₂-particles the choice of appropriate substrates is limited because their removal by hydrofluoric acid will also affect substrates if it is made of SiO₂.

In this thesis, two NIP systems are demonstrated with size-exclusion properties. However the assessment of selectivity remained largely open due to limited tuning possibilities in these systems. The next step in developing NIP systems will include recognizing NPs based on their shell. For this purpose, matrix materials should enable the introduction of functional groups or manipulation of the surface charge by control of the pH. Both allow tuning the selectivity towards particular NP shells. For example, molecular layers grafted by the reduction of aryldiazonium layers may contain a variety of functional groups such as nitro, hydroxyl or carboxyl.^[288] Poly(ethylenimine) offers another attractive opportunity to introduce certain chemical groups capable of forming selective polymer-mediated interactions. However, all polymers need to be characterized in terms of the layer thickness or morphology before they can be classified as suitable for the preparation of thin NIPs.

All studies show that the characterization of NIPs is not trivial, providing one of the most challenging tasks of this thesis. Imaging of small cavities via SFM turns out to be rather difficult due to the appearance of convolution effects. Furthermore, the blocking properties of the composites cause charge accumulations during SEM measurements. XPS was not promising for the detection of particles in monolayer amounts and it was not possible to distinguish between NPs inside cavities and on the surface of the films. However, electrochemical observation of the NP release turns out to be a very convenient tool enabled by matrices of a precisely controlled thickness. The lack of an ohmic contact between embedded particles and the substrate would prevent the dissolution of NPs.

Thus, the current during dissolution of metal NPs gives an immediate and quantitative indication about the success of the removal step. This is shown to be highly effective at discriminating between those NPs that are inside the cavities in an ohmic contact to the electrode surface and the non-specifically adhering NPs at the matrix surface. Other analytical methods besides those based on electrochemistry should be tested for observing the NPs captured in cavities because not all interesting NPs are electrochemically active in the accessible potential range. Single nanoparticle spectroscopy^[289] is another appealing approach to detect NPs. It could be used to characterize transport properties in solution and motion on NIP surfaces at a single particle level.

NIP materials can also be used to form systems capable of a controlled or even switchable release of small amounts of NPs. This could be another interesting approach for further development of NIP systems. A controlled release could be for instance valuable for microanalytical or nanoanalytical procedures.

8. Appendix

A1 SFM thickness determination (Chapter 5.1)

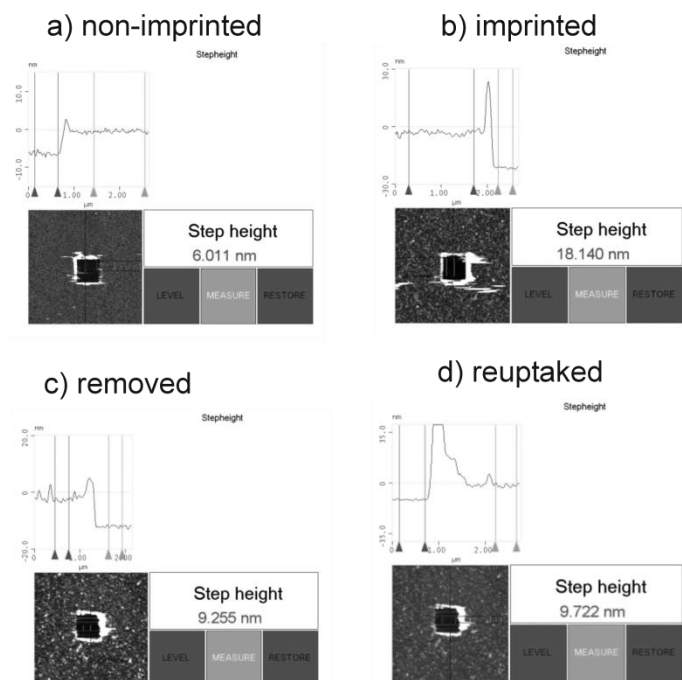


Figure A1. Primary data for thickness determination by SFM after local mechanical removal of the polymer film; a) non-imprinted poly(scopoletin), b) poly(scopoletin) imprinted with ferritin, c) imprinted poly(scopoletin) after removal of ferritin with 5 mM NaOH for 20 min; d) sample c) after template rebinding from 500 nM ferritin solution for 30 min.

A2 SFM section profile determination (Chapter 5.1)

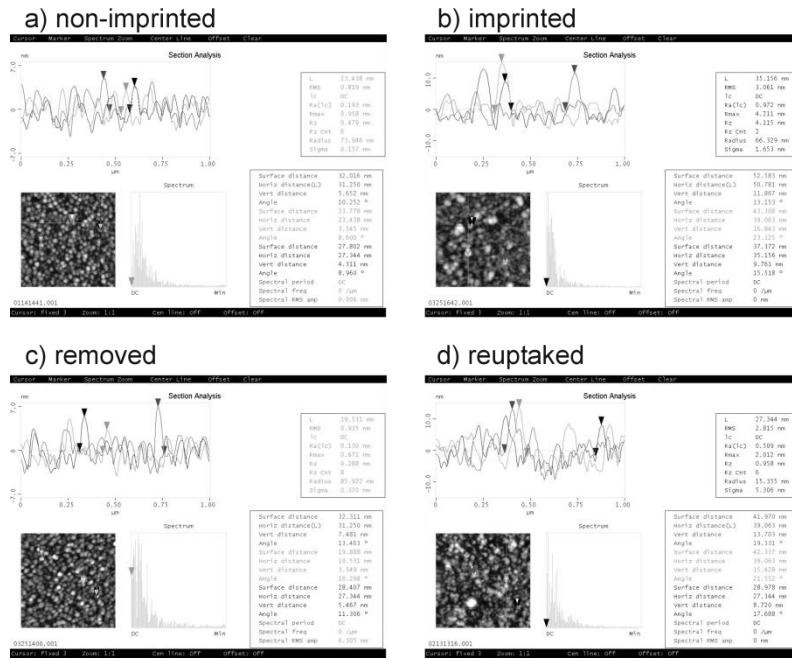


Figure A2. SFM determination of typical object heights in the poly(scopoletin) films; a) non-imprinted poly(scopoletin), b) poly(scopoletin) imprinted with ferritin, c) imprinted poly(scopoletin) after removal of ferritin by 5 mM NaOH for 20 min; d) sample of c) after rebinding from 500 nM ferritin solution for 30 min.

B1 SFM thickness determination of poly(plumbagin) (Chapter 6.2)

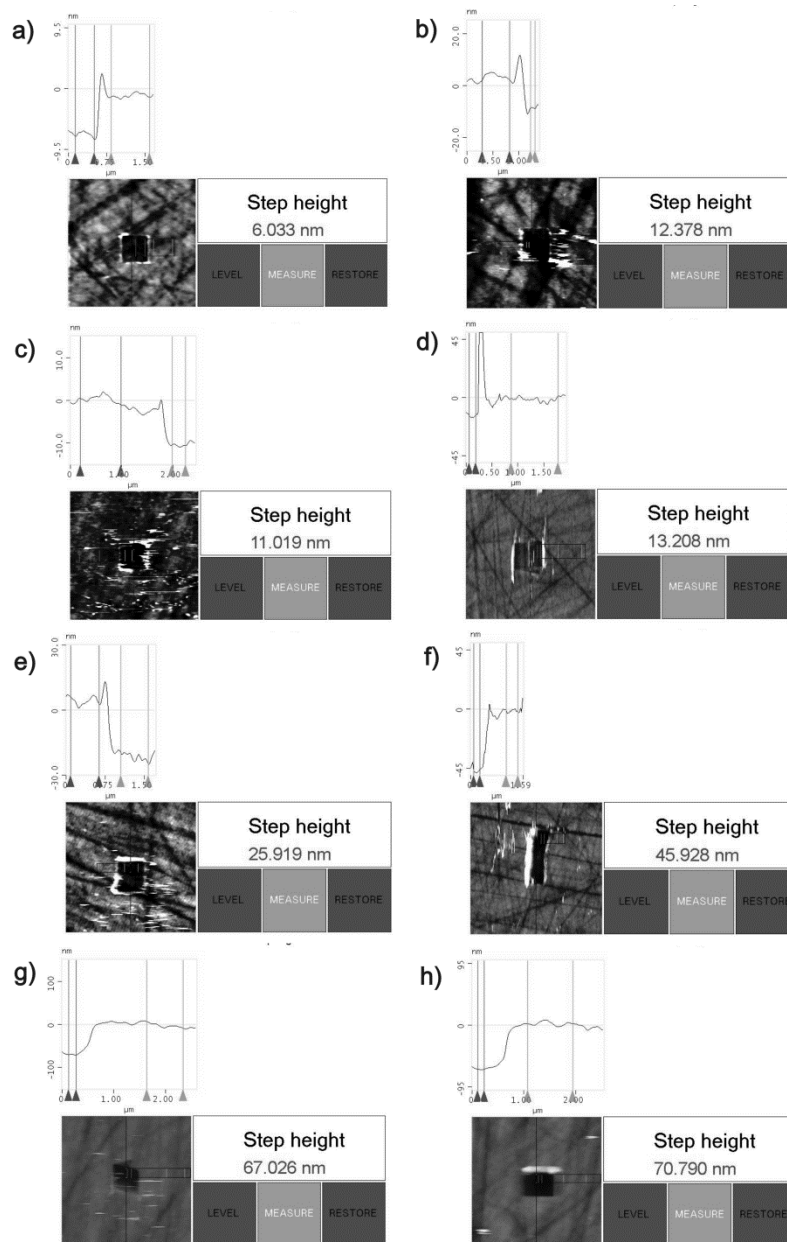


Figure B1: Thickness determination by SFM using a MSCT SFM tip ($k = 0.6 \text{ N m}^{-1}$). a) polyPLG/GC (from 5 deposition cycles, b) polyPLG/GC from 25 deposition cycles, c) polyPLG/GC from 50 deposition cycles, d) polyPLG/PLG/GC from 10 deposition cycles, e) polyPLG/PLG/GC from 25 deposition cycles, f) polyPLG/PLG/GC from 50 deposition cycles, g) polyPLG/PLG/GC from 100 deposition cycles; h) polyPLG/PLG/GC from 10 deposition cycles.

B2 SEM images of bare GC and polyPLG/GC (Chapter 6.2)

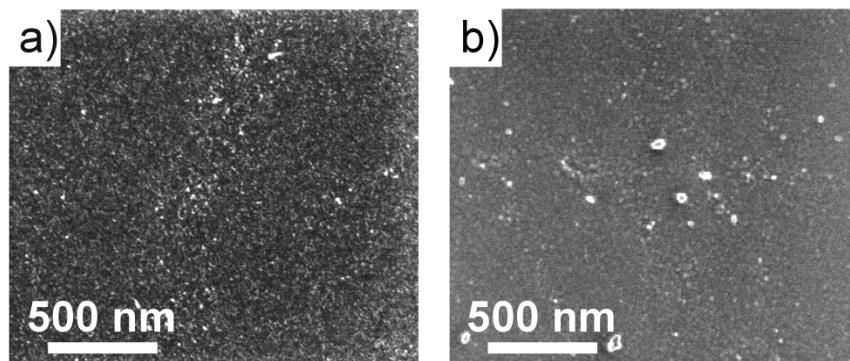
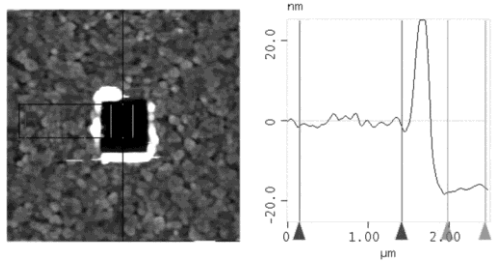
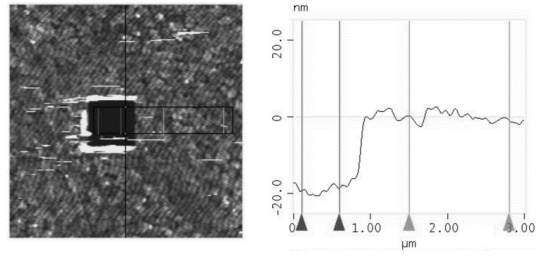
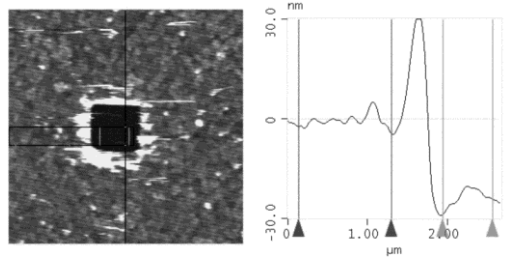


Figure B2. SEM images recorded at 15-25 kV of a) bare GC and b) polyPLG/GC film thickness 12 nm (from SFM) after 25 potential cycles in 0.2 mM plumbagin in deaerated phosphate solution pH 7.

C1 SFM thickness determination of poly(phenol) films (Chapter 6.3)

Table C1. Experimental details and results for SFM thickness and roughness determination of PPh films and NIP films. Thickness determination were performed in contact mode, with a MSCT tip, $k = 0.6 \text{ N m}^{-1}$ and roughness determination in intermittent mode, with a NCHV-A tip, $k = 42 \text{ N m}^{-1}$ of electrochemically deposited polyphenol on a) PPh/ITO, b) PPh/AuNP/ITO_{APTES} and of c) NIPs after template removal in KCN (PPh/{}_c/ITO_{APTES}), while polymer layers at bare ITO electrodes show a similar surface roughness and film thicknesses as observed at ITO_{APTES} (not shown). Hence, untreated ITO samples were used for all control experiments in analogy to ITO_{APTES}.

Scan rate		RMS roughness [nm]	Thickness [nm]
a) 2.4 Hz		3.17	16.6-17.8
b) 6.1 Hz		3.68	19.3-23.3
c) 3.9 Hz		1.00	19.0-23.4

C2 Complementary investigations of phenol electropolymerization at a bare Au/glass electrode by cyclic voltammetry and scanning force microscopy (Chapter 6.3)

Electropolymerization of phenol on Au/glass electrodes (Fig. C2a) was conducted in aqueous solution containing 50 mM phenol + 0.1 M NaH_2PO_4 . The enlarged scale of the first two backward scans of the CV is shown in Fig. C indicating a barely visible gold reduction signal at 0.64 V (Fig. C2b).

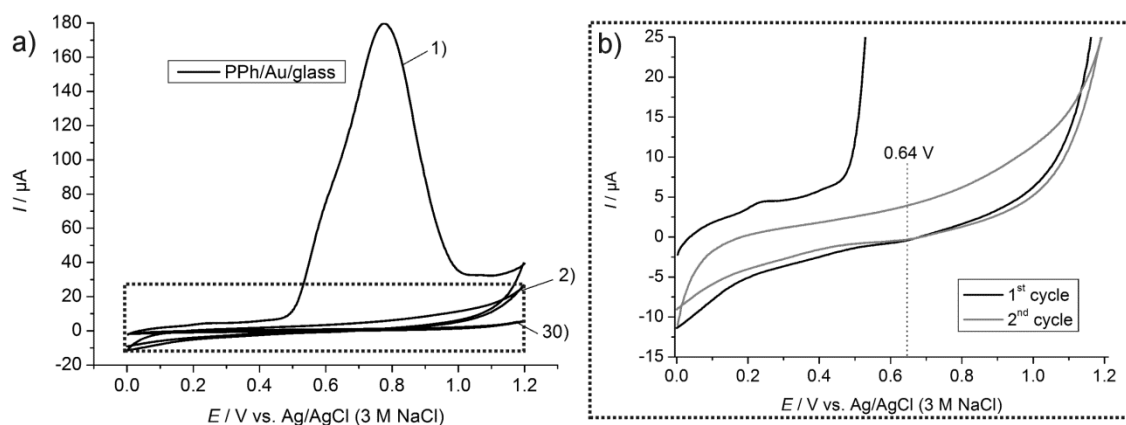


Figure C2. a) The 1st, 2nd and 30th CV during the electropolymerization of phenol in an aqueous solution containing 50 mM phenol + 0.1 M NaH_2PO_4 at $v = 50 \text{ mV s}^{-1}$ at a bare Au/glass electrode. b) Enlarged view of the first two cycles indicating the gold oxide/hydroxide reduction process at 0.6 V.

C3 Permeability test of KCN treated samples (Chapter 6.3)

Additional examples of CVs in Fig. C3 representing the change in permeability at a) PPh/AuNP/ITO_{APTES} and b) PPh/ITO before (black curve) and after (grey curve) exposing samples to aqueous 6 mM KCN etching solution. The electrode area was defined by mounting the samples as the bottom of the cylindrical liquid reservoir of a Teflon cell with an exposed area of 0.502 cm². Selected samples in Fig. C3 represent typically observed CV characters.

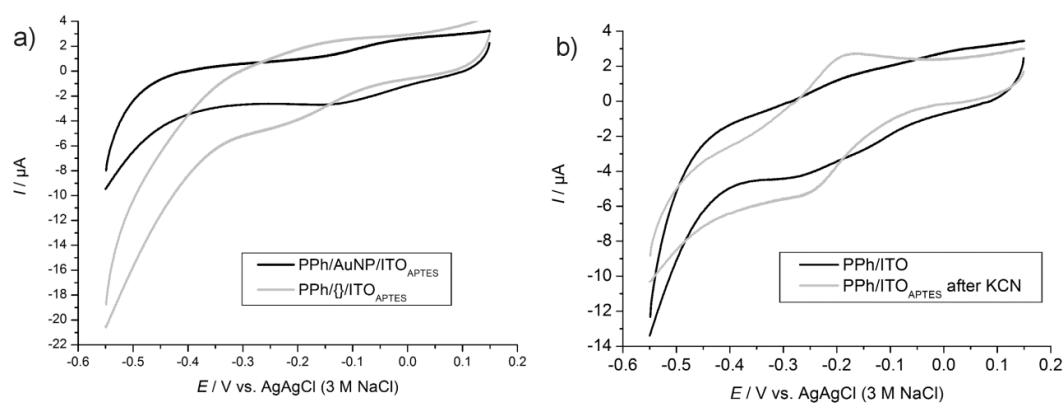


Figure C3. CVs recorded in 1 mM $[\text{Ru}(\text{NH}_3)_6]\text{Cl}_3 + 0.1 \text{ M KCl}$ at a scan rate of 0.1 V s^{-1} at a) PPh/AuNPs/ITO_{APTES} and b) PPh/ITO before (black curve) and after (grey curve) KCN treatment.

8.1 Abbreviation

AFM	atomic force microscopy
Au/glass	glass slides covered with a thin gold layer and used as WE
AgNP	silver nanoparticle
AuNP	gold nanoparticle
AuNP/ITO _{APTES}	samples after immobilization of AuNPs onto APTES-modified ITO substrates
APTES	3-(aminopropyl)triethoxysilane
BSE	backscattered electrons
C5, C25, C50, C100/ITO	NIP named depending on the amount of NPs added to the spin-coting solution and the nature of the substrate (C = composite, number = particle amount in μl , substrate = glass or ITO)
CE	counter electrode
CFM	chemical force microscopy
CNT	carbon nano tubes
CV	cyclic voltammogram
DLVO theory	Deyagin-Landau and Verwey-Overbeek theory
EDX	energy dispersive X-ray spectroscopy
ESEM	enviromental scanning electron microscopy
et al.	from latin et (and) alii (others)
GC	glassy carbon
HEPES	4-(2-hydroxyethyl)-1-piperazineethanesulfonic acid
ITO	idium tin oxide
LB	Langmuir-Blodgett
LFM	lateral force microscopy
LSV	linear sweep voltammetry
MIP	molecularly imprinted polymer
MWCNT	multi-walled carbon nanotubes
NIP	nanoparticle imprinted polymer
NP	nanoparticle
NSL	nanosphere lithography
OA	oleic acid
PANI	poly(aniline)
PDMS	poly(dimethylsiloxane)
PEDOT	poly(3,4-ethylenedioxythiophene)
PFM	pulsed-force mode
PLG	plumbagin

polyPLG/GC	sample after electropolymerization of plumbagin on bare GC
polyPLG/PLG/GC	sample after electropolymerization of plumbagin on a grafted monolayer of plumbagin on GC
PMIRRAS	polarization modulation infrared reflection adsorption spectroscopy
PPh	poly(phenol)
PPh/AuNP/ITO _{APTES}	NIPs prepared by electropolymerization of PPh on AuNP/ITO _{APTES} substrates
PPh/ITO	samples after electropolymerization of PPh on ITO
PPh/{ _{ec} }/ITO _{APTES}	NIP after electrochemical removal of AuNPs from a PPh matrix on APTES-coated ITO
PPh/{ _c }/ITO _{APTES}	NIP after chemical removal of AuNPs from a PPh matrix on APTES-coated ITO
PPh/{AgNP}/ITO _{APTES}	NIP after reuptake of analyte AgNP
PPh/{AuNP}/ITO _{APTES}	NIP after reuptake of analyte AuNP
RAM	randomly arranged microelectrodes
RE	reference electrode
RMS roughness	root mean square roughness
SE	secondary electrons
SEM	scanning electron microscopy
SFM	scanning force microscopy
SMFS	single molecule force spectroscopy
STM	scanning tunneling microscopy
SWCNT	single-walled carbon nanotubes
TLD	through lens detector
TSG	template stripped gold
UHV	ultra high vacuum
UV	ultra violet
WE	working electrode
XPS	X-ray photoelectron spectroscopy
2D	two-dimensional
3D	three-dimensional

8.2 Symbols

A	area
a	stoichiometric number of Cl^- ions
β'	conditional brutto stability constant
c°	standard concentration

$c(\text{Au}^{3+})$	concentration of gold ions
$c(\text{Cl}^-)$	concentration of chloride ions
$c(\text{AuCl}_4^-)$	concentration of the tetrachloroaurate(III) complex
c^*	bulk concentration of $[\text{Ru}(\text{NH}_3)_6]^{2+/3+}$
c_{NP}^*	bulk concentration of NPs
c_{AuNP}^*	bulk concentration of AuNPs
c_{AgNP}^*	bulk concentration of AgNPs
c_t	total concentration of metal ions
d	thickness of the cantilever
D	diffusion coefficient
D_{NP}	diffusion coefficient of NPs
D_{AuNP}	diffusion coefficient of AuNPs
D_{AgNP}	diffusion coefficient of AgNPs
E	potential
E_1	start potential of the AuNP oxidation peak
E_2	end potential of the AuNP oxidation peak
ΔE	shift of the gold oxidation potential
$E_{(\text{Au}/\text{Au}^{3+})}^{\circ'}$	standard potential of gold in water
$E_{(\text{Au}/\text{Au}^{3+})}^{\circ'}$	standard potential of gold in aqueous potassium chloride solution
F	Faraday constant
f_0	frequency
ΔF	force acting between SFM tip and specimen
Γ_{NP}	number of NPs determined from counting NP density in SFM images
Γ_{NPec}	number of electrochemically dissolved NPs
i_d	diffusion-limited currents at an inlaid nanoelectrode
i_{RAM}	diffusion-limited currents at a recessed nanoelectrode
J	flux of NPs
j_D	experimentally measured current
$j_{\text{RAMexpected}}$	expected current
I	current
k	spring constant
k_B	Boltzmann constant
l	length of the cantilever
τ	polymer film thickness
m	mass of the cantilever
m_{AuNP}	mass of one AuNP with a diameter of 30 nm
N_{NP}	amount of NPs
N_{AuNP}	amount of AuNPs

N_{AgNP}	amount of AgNPs
n_z	number of transferred electrons
n_{Au}	amount of gold atoms in one NP
η	dynamic viscosity
Π	surface pressure
ρ	density
Q/A	charge density
Q_{total}	integrated charge
Q_{AuNP}	required charge to remove one AuNP with a diameter of 30 nm
R	gas constant
r	NP radius
r_{RAM}	radius of the active area of an individual inlaid nanoelectrode
r_{AuNP}	radius of AuNP
r_{AgNP}	radius of AgNP
T	temperature
t	time
V_{AuNP}	volume of one AuNP with a diameter of 30 nm
w	width of the cantilever
χ	recess factor
x	extension and retraction of the piezoelectric scanner in x -direction
Y	Young's modulus (coefficient of elasticity)
y	extension and retraction of the piezoelectric scanner along the y -axis
z	extension and retraction of the piezoelectric scanner along the z -axis
Δz	deflection of the cantilever

9. References

- [1] <http://www.nano.gov/nanotech-101/special>, accessed 23 November, **2015**.
- [2] A. Dhakshinamoorthy, H. Garcia, *Chem. Soc. Rev.* **2012**, *41*, 5262.
- [3] E. H. Sargent, *Nature Photonics* **2012**, *6*, 133.
- [4] V. Myroshnychenko, J. Rodriguez-Fernandez, I. Pastoriza-Santos, A. M. Funston, C. Novo, P. Mulvaney, L. M. Liz-Marzan, F. J. Garcia de Abajo, *Chem. Soc. Rev.* **2008**, *37*, 1792.
- [5] L. Lu, Z. Luo, T. Xu, L. Yu, *Nano Lett.* **2013**, *13*, 59.
- [6] S. Chernousova, M. Epple, *Angew. Chem., Int. Ed.* **2013**, *52*, 1636.
- [7] J.-P. Dery, E. F. Borra, A. M. Ritcey, *Chem. Mater.* **2008**, *20*, 6420.
- [8] J. S. Beveridge, J. R. Stephens, M. E. Williams, *Annu. Rev. Anal. Chem.* **2011**, *4*, 251.
- [9] H. B. Na, I. C. Song, T. Hyeon, *Adv. Mater. (Weinheim, Ger.)* **2009**, *21*, 2133.
- [10] B. L. Cushing, V. L. Kolesnichenko, C. J. O'Connor, *Chem. Rev.* **2004**, *104*, 3893.
- [11] S. Sun, *Adv. Mater. (Weinheim, Ger.)* **2006**, *18*, 393.
- [12] M.-P. Pileni, *Nat. Mater.* **2003**, *2*, 145.
- [13] M. L. Personick, C. A. Mirkin, *J. Am. Chem. Soc.* **2013**, *135*, 18238.
- [14] G. H. Woehrle, L. O. Brown, J. E. Hutchison, *J. Am. Chem. Soc.* **2005**, *127*, 2172.
- [15] A. Desireddy, B. E. Conn, J. Guo, B. Yoon, R. N. Barnett, B. M. Monahan, K. Kirschbaum, W. P. Griffith, R. L. Whetten, U. Landman, T. P. Bigioni, *Nature (London, U. K.)* **2013**, *501*, 399.
- [16] www.nanotechproject.org/news/archive/8277/, accessed 26 November, **2015**.
- [17] V. L. Colvin, *Nat. Biotechnol.* **2003**, *21*, 1166.
- [18] A. Nel, T. Xia, L. Mädler, N. Li, *Science* **2006**, *311*, 622.
- [19] S. J. Stohs, D. Bagchi, *Free Radical Biol. Med.* **1995**, *18*, 321.
- [20] M. Valko, H. Morris, M. T. D. Cronin, *Current Medicinal Chemistry* **2005**, *12*, 1161.
- [21] M.-C. Daniel, D. Astruc, *Chem. Rev.* **2004**, *104*, 293.
- [22] S. Kango, S. Kalia, A. Celli, J. Njuguna, Y. Habibi, R. Kumar, *Prog. Polym. Sci.* **2013**, *38*, 1232.
- [23] C. Batchelor-McAuley, K. Tschulik, C. C. M. Neumann, E. Laborda, R. G. Compton, *Int. J. Electrochem. Sci.* **2014**, *9*, 1132.
- [24] <http://www.nanopartikel.info/projekte/abgeschlossene-projekte>, accessed 2 December, **2015**.
- [25] V. Stone, S. Pozzi-Mucelli, L. Tran, K. Aschberger, S. Sabella, U. Vogel, C. Poland, D. Balharry, T. Fernandes, S. Gottardo, S. Hankin, G. J. Hartl Mark, N. Hartmann, D. Hristozov, K. Hund-Rinke, H. Johnston, A. Marcomini, O. Panzer, D. Roncato, T. Saber Anne, H. Wallin, J. Scott-Fordsmand Janeck, *Particle and fibre toxicology* **2014**, *11*, 9.
- [26] K. Haupt, *Analyst* **2001**, *126*, 747.
- [27] S. A. Piletsky, A. P. F. Turner, *Electroanal.* **2002**, *14*, 317.
- [28] K. Haupt, K. Mosbach, *Chem. Rev. (Washington, D. C.)* **2000**, *100*, 2495.
- [29] S. Koenig, V. Chechik, *Chem. Commun.* **2005**, 4110.
- [30] G. Binnig, C. F. Quate, *Phys. Rev. Lett.* **1986**, *56*, 930.
- [31] G. Binnig, H. Rohrer, *Angewandte Chemie International Edition English* **1987**, *26*, 606.
- [32] G. Binnig, H. Rohrer, *Helv. Phys. Acta* **1982**, *55*, 726.

- [33] J. A. Dagata, J. Schneir, H. H. Harary, C. J. Evans, M. T. Postek, J. Bennett, *Appl. Phys. Lett.* **1990**, *56*, 2001.
- [34] T. Tansel, O. M. Magnussen, *Phys. Rev. Lett.* **2006**, *96*, 026101/1.
- [35] S. Szunerits, S. E. Pust, G. Wittstock, *Anal. Bioanal. Chem.* **2007**, *389*, 1103.
- [36] E. Pensa, A. A. Rubert, G. Benitez, P. Carro, A. G. Orive, A. H. Creus, R. C. Salvarezza, C. Vericat, *J. Phys. Chem. C* **2012**, *116*, 25765.
- [37] H. Lu, G. Meng, Y. Li, F. Wang, *Journal of Materials Science & Technology (Shenyang, China)* **2005**, *21*, 311.
- [38] X. K. Zhao, L. McCormick, J. H. Fendler, *Chem. Mater.* **1991**, *3*, 922.
- [39] J. Y. Park, S. Maier, B. Hendriksen, M. Salmeron, *Mater. Today* **2010**, *13*, 38.
- [40] K. D. Jandt, *Surf. Sci.* **2001**, *491*, 303.
- [41] A. F. Raigoza, J. W. Dugger, L. J. Webb, *ACS Appl. Mater. Interfaces* **2013**, *5*, 9249.
- [42] U. Mohideen, A. Roy, *Phys. Rev. Lett.* **1998**, *81*, 4549.
- [43] Q. Zhang, L. A. Archer, *J. Phys. Chem. B* **2003**, *107*, 13123.
- [44] D. A. Ramrus, J. C. Berg, *J. Adhes. Sci. Technol.* **2004**, *18*, 1395.
- [45] S. B. Velegol, B. E. Logan, *Langmuir* **2002**, *18*, 5256.
- [46] I. M. Nnebe, J. W. Schneider, *Macromolecules* **2006**, *39*, 3616.
- [47] A. N. Campbell, E. I. Cole, B. A. Dodd, R. E. Anderson, *Microelectron. Eng.* **1994**, *24*, 11.
- [48] X. Hong, Y. Gan, Y. Wang, *Surf. Interface Anal.* **2010**, *43*, 1299.
- [49] F. Anariba, S. H. DuVall, R. L. McCreery, *Anal. Chem.* **2003**, *75*, 3837.
- [50] S. L. Pyshkin, J. Ballato, I. Luzinov, B. Zdyrko, *J. Nanopart. Res.* **2011**, *13*, 5565.
- [51] S. R. Kane, P. D. Ashby, L. A. Pruitt, *J. Mater. Sci.: Mater. Med.* **2010**, *21*, 1037.
- [52] C. Ton-That, A. G. Shard, R. H. Bradley, *Langmuir* **2000**, *16*, 2281.
- [53] K. Seo, E. Borguet, *Langmuir* **2006**, *22*, 1388.
- [54] M. Hirtz, M. K. Brinks, S. Miele, A. Studer, H. Fuchs, L. Chi, *Small* **2009**, *5*, 919.
- [55] T. Tian, B. Singhana, L. E. Englade-Franklin, X. Zhai, T. R. Lee, J. C. Garno, *Beilstein J. Nanotechnol.* **2014**, *5*, 26.
- [56] S. Szunerits, R. Boukherroub, *Langmuir* **2006**, *22*, 1660.
- [57] F. Billi, E. Onofre, E. Ebramzadeh, T. Palacios, M. L. Escudero, M. C. Garcia-Alonso, *Surf. Coat. Technol.* **2012**, *212*, 134.
- [58] D. P. Allison, N. P. Mortensen, C. J. Sullivan, M. J. Doktycz, *Wiley Interdiscip. Rev. Nanomed. Nanobiotechnol.* **2010**, *2*, 618.
- [59] F. Meiners, M. Ahlers, I. Brand, G. Wittstock, *Surf. Sci.* **2015**, *631*, 220.
- [60] P. Samori, M. Surin, V. Palermo, R. Lazzaroni, P. Leclere, *Phys. Chem. Chem. Phys.* **2006**, *8*, 3927.
- [61] M. Radmacher, M. Fritz, P. K. Hansma, *Biophys. J.* **1995**, *69*, 264.
- [62] J. A. Gallego-Juarez, *J. Phys. E: Sci. Instrum.* **1989**, *22*, 804.
- [63] N. S. Tambe, B. Bhushan, *J. Phys. D: Appl. Phys.* **2005**, *38*, 764.
- [64] F. L. Leite, C. C. Bueno, A. L. Da Roz, E. C. Ziemath, O. N. Oliveira, Jr., *Int. J. Mol. Sci.* **2012**, *13*, 12773.
- [65] R. Ledesma-Alonso, D. Legendre, P. Tordjeman, *Langmuir* **2013**, *29*, 7749.
- [66] A. L. Weisenhorn, P. K. Hansma, T. R. Albrecht, C. F. Quate, *Appl. Phys. Lett.* **1989**, *54*, 2651.
- [67] T. R. Albrecht, C. F. Quate, *J. Vac. Sci. Technol., A* **1988**, *6*, 271.
- [68] S. S. Wong, E. Joselevich, A. T. Woolley, C. L. Cheung, C. M. Lieber, *Nature* **1998**, *394*, 52.

- [69] D. Keller, *Nature* **1996**, 384, 111.
- [70] H. Dai, J. H. Hafner, A. G. Rinzler, D. T. Colbert, R. E. Smalley, *Nature* **1996**, 384, 147.
- [71] C. Yang, J. Mamouni, Y. Tang, L. Yang, *Langmuir* **2010**, 26, 16013.
- [72] R. Wilson Neil, V. Macpherson Julie, *Nat. Nanotechnol.* **2009**, 4, 483.
- [73] J. Martinez, T. D. Yuzvinsky, A. M. Fennimore, A. Zettl, R. Garcia, C. Bustamante, *Nanotechnology* **2005**, 16, 2493.
- [74] E. Meyer, *Prog. Surf. Sci.* **1992**, 41, 3.
- [75] H.-J. Butt, B. Cappella, M. Kappl, *Surf. Sci. Rep.* **2005**, 59, 1.
- [76] E. Fantner Georg, G. Schitter, H. Kindt Johannes, T. Ivanov, K. Ivanova, R. Patel, N. Holten-Andersen, J. Adams, J. Thurner Philipp, W. Rangelow Ivo, K. Hansma Paul, *Ultramicroscopy* **2006**, 106, 881.
- [77] J. D. Adams, A. Nievergelt, B. W. Erickson, C. Yang, M. Dukic, G. E. Fantner, *Rev. Sci. Instrum.* **2014**, 85, 093702/1.
- [78] M. B. Viani, T. E. Schaffer, A. Chand, M. Rief, H. E. Gaub, P. K. Hansma, *J. Appl. Phys.* **1999**, 86, 2258.
- [79] Y. Song, B. Bhushan, *J. Phys.: Condens. Matter* **2008**, 20, 225012/1.
- [80] F. L. Leite, L. G. Paterno, C. E. Borato, P. S. P. Herrmann, O. N. Oliveira, L. H. C. Mattoso, *Polymer* **2005**, 46, 12503.
- [81] Y. Sugimoto, P. Pou, M. Abe, P. Jelinek, R. Perez, S. Morita, O. Custance, *Nature* **2007**, 446, 64.
- [82] J.-B. D. Green, M. T. McDermott, M. D. Porter, L. M. Siperko, *J. Phys. Chem.* **1995**, 99, 10960.
- [83] M. Textor, L. Ruiz, R. Hofer, A. Rossi, K. Feldman, G. Haehner, N. D. Spencer, *Langmuir* **2000**, 16, 3257.
- [84] K. C. Wagner, Y. Wang, S. L. Regen, D. V. Vezenov, *Phys. Chem. Chem. Phys.* **2013**, 15, 14037.
- [85] R. Bennewitz, K. Broermann, P. Egberts, N. N. Gosvami, F. Hausen, C. Held, *Adv. Eng. Mater.* **2010**, 12, 362.
- [86] A. Noy, D. V. Vezenov, C. M. Lieber, *Annu. Rev. Mater. Sci.* **1997**, 27, 381.
- [87] A. Wawkuszewski, K. Craemer, H. J. Cantow, S. N. Magonov, *Ultramicroscopy* **1995**, 58, 185.
- [88] A. San Paulo, R. Garcia, *Phys. Rev. B Condens. Matter Mater. Phys.* **2001**, 64, 193411/1.
- [89] I. Schmitz, M. Schreiner, G. Friedbacher, M. Grasserbauer, *Appl. Surf. Sci.* **1997**, 115, 190.
- [90] S. Morita, S. Fujisawa, E. Kishi, M. Ohta, H. Ueyama, Y. Sugawara, *Thin Solid Films* **1996**, 273, 138.
- [91] F. M. Ohnesorge, *Surf. Interface Anal.* **1999**, 27, 379.
- [92] H. Hosoi, K. Sueoka, K. Hayakawa, K. Mukasa, *Appl. Surf. Sci.* **2000**, 157, 218.
- [93] B. Cappella, G. Dietler, *Surf. Sci. Rep.* **1999**, 34, 1.
- [94] D. Wang, X.-B. Liang, Y.-H. Liu, S. Fujinami, T. Nishi, K. Nakajima, *Macromolecules (Washington, DC, United States)* **2011**, 44, 8693.
- [95] Y. Seo, W. Jhe, *Rep. Prog. Phys.* **2008**, 71, 016101/1.
- [96] B. Anczykowski, B. Gotsmann, H. Fuchs, J. P. Cleveland, V. B. Elings, *Appl. Surf. Sci.* **1999**, 140, 376.
- [97] R. Garcia, C. J. Gomez, N. F. Martinez, S. Patil, C. Dietz, R. Magerle, *Phys. Rev. Lett.* **2006**, 97, 016103/1.

- [98] C. J. Gomez, R. Garcia, *Ultramicroscopy* **2010**, *110*, 626.
- [99] T. Utzig, S. Raman, M. Valtiner, *Langmuir* **2015**, *31*, 2722.
- [100] F. Kienberger, V. P. Pastushenko, G. Kada, H. J. Gruber, C. Riener, H. Schindler, P. Hinterdorfer, *Single Molecules* **2000**, *1*, 123.
- [101] J. Zlatanova, S. M. Lindsay, S. H. Leuba, *Prog. Biophys. Mol. Biol.* **2000**, *74*, 37.
- [102] M. Rief, H. Grubmuller, *ChemPhysChem* **2002**, *3*, 255.
- [103] A. F. Oberhauser, C. Badilla-Fernandez, M. Carrion-Vazquez, J. M. Fernandez, *J. Mol. Biol.* **2002**, *319*, 433.
- [104] D. T. Edwards, J. K. Faulk, A. W. Sanders, M. S. Bull, R. Walder, M.-A. LeBlanc, M. C. Sousa, T. T. Perkins, *Nano Lett.* **2015**, *15*, 7091.
- [105] J. Orozco, C. Jimenez-Jorquera, C. Fernandez-Sanchez, *Electroanal.* **2012**, *24*, 635.
- [106] T. Puntheeranurak, I. Neundlinger, R. K. H. Kinne, P. Hinterdorfer, *Nature Protocols* **2011**, *6*, 1443.
- [107] N. W. Moore, T. L. Kuhl, *Biophys. J.* **2006**, *91*, 1675.
- [108] D. Leckband, W. Mueller, F. J. Schmitt, H. Ringsdorf, *Biophys. J.* **1995**, *69*, 1162.
- [109] D. N. Leonard, G. W. Chandler, S. Seraphin, *Characterization of Materials (2nd Edition)* **2012**, *3*, 1721.
- [110] A. M. Donald, *Nat. Mater.* **2003**, *2*, 511.
- [111] N. B. Magee, A. Miller, M. Amaral, A. Cumiskey, *Atmospheric Chemistry and Physics* **2014**, *14*, 12357.
- [112] M. J. Garcia-Salinas, A. M. Donald, *J. Colloid Interface Sci.* **2010**, *342*, 629.
- [113] S. E. Kirk, J. N. Skepper, A. M. Donald, *J. Microsc. (Oxford, U. K.)* **2009**, *233*, 205.
- [114] P. Meredith, A. M. Donald, *Journal of Microscopy (Oxford)* **1996**, *181*, 23.
- [115] S. Chen, R. W. Murray, S. W. Feldberg, *J. Phys. Chem. B* **1998**, *102*, 9898.
- [116] J. F. Hicks, A. C. Templeton, S. Chen, K. M. Sheran, R. Jasti, R. W. Murray, *Anal. Chem.* **1999**, *71*, 3703.
- [117] Y. Bae, N. Myung, A. J. Bard, *Nano Lett.* **2004**, *4*, 1153.
- [118] Y.-G. Zhou, N. V. Rees, R. G. Compton, *Chem. Commun. (Cambridge, U. K.)* **2012**, *48*, 2510.
- [119] A. J. Bard, H. Zhou, S. J. Kwon, *Isr. J. Chem.* **2011**, *50*, 267.
- [120] X. Xiao, A. J. Bard, *J. Am. Chem. Soc.* **2007**, *129*, 9610.
- [121] X. Xiao, F. Fan Fu-Ren, J. Zhou, J. Bard Allen, *J. Am. Chem. Soc.* **2008**, *130*, 16669.
- [122] H. S. Ahn, A. J. Bard, *Angew. Chem., Int. Ed.* **2015**, *54*, 13753.
- [123] P. W. Atkins, *Physikalische Chemie*, VCH, Weinheim, **1996**.
- [124] E.-G. Jäger, K. Schöne, *Electrolytgleichgewichte und Elektrochemie*, Dt. Verl. f. Grundstoffindustrie, Leipzig, **1984**.
- [125] C.-H. Chen, E. R. Ravenhill, D. Momotenko, Y.-R. Kim, S. C. S. Lai, P. R. Unwin, *Langmuir* **2015**, *31*, 11932.
- [126] A. N. Shipway, E. Katz, I. Willner, *ChemPhysChem* **2000**, *1*, 18.
- [127] B. A. Korgel, S. Fullam, S. Connolly, D. Fitzmaurice, *J. Phys. Chem. B* **1998**, *102*, 8379.
- [128] M. Nagel, S. G. Hickey, A. Froemsdorf, A. Kornowski, H. Weller, *Z. Phys. Chem. (Muenchen, Ger.)* **2007**, *221*, 427.
- [129] J. Henzie, M. Gruenwald, A. Widmer-Cooper, P. L. Geissler, P. Yang, *Nat. Mater.* **2012**, *11*, 131.

- [130] S. Srivastava, D. Nykypanchuk, M. Fukuto, O. Gang, *ACS Nano* **2014**, *8*, 9857.
- [131] R. Thiruvengadathan, V. Korampally, A. Ghosh, N. Chanda, K. Gangopadhyay, S. Gangopadhyay, *Rep. Prog. Phys.* **2013**, *76*, 066501/1.
- [132] S. E. Williams, P. R. Davies, J. L. Bowen, C. J. Allender, *Nanomaterials* **2013**, *3*, 192.
- [133] E. S. Kooij, E. A. M. Brouwer, H. Wormeester, B. Poelsema, *Langmuir* **2002**, *18*, 7677.
- [134] E. J. W. Verwey, J. T. G. Overbeek, *Theory of the Stability of Lyophobic Colloids*, **1948**.
- [135] B. Deryagin, L. Landau, *Acta Physicochimica URSS* **1941**, *14*, 633.
- [136] B. S. Flavel, M. R. Nussio, J. S. Quinton, J. G. Shapter, *J. Nanopart. Res.* **2009**, *11*, 2013.
- [137] Rajesh, V. Sharma, S. K. Mishra, A. M. Biradar, *Mater. Chem. Phys.* **2012**, *132*, 22.
- [138] S. Q. Li, L. Liu, J. B. Hu, *Sci. China: Chem.* **2012**, *55*, 1940.
- [139] M. Pauly, B. P. Pichon, A. Demortiere, J. Delahaye, C. Leuvrey, G. Pourroy, S. Begin-Colin, *Superlattices Microstruct.* **2009**, *46*, 195.
- [140] Q. Guo, X. Teng, S. Rahman, H. Yang, *J. Am. Chem. Soc.* **2003**, *125*, 630.
- [141] V. Aleksandrovic, D. Greshnykh, I. Randjelovic, A. Froemsdorf, A. Kornowski, S. V. Roth, C. Klinke, H. Weller, *arXiv.org, e-Print Archive, Condensed Matter* **2009**, 1.
- [142] S. Paul, C. Pearson, A. Molloy, M. A. Cousins, M. Green, S. Kolliopoulou, P. Dimitrakakis, P. Normand, D. Tsoukalas, M. C. Petty, *Nano Lett.* **2003**, *3*, 533.
- [143] L. Romanszki, J. Telegdi, E. Kalman, *Colloids Surf., A* **2008**, *321*, 20.
- [144] S. Chen, *Langmuir* **2001**, *17*, 2878.
- [145] R. Capan, A. K. Hassan, A. V. Nabol, A. K. Ray, T. H. Richardson, M. C. Simmonds, C. Sammon, *IEE Proc.-Circuits Devices Syst.* **2003**, *150*, 367.
- [146] L. Zhang, Y. Li, Y. Shen, A. Xie, *Mater. Chem. Phys.* **2011**, *125*, 522.
- [147] H. Ding, P. Bertocello, M. Kumar Ram, C. Nicolini, *Electrochem. Commun.* **2002**, *4*, 503.
- [148] V. Vidya, N. Prasanth Kumar, S. N. Narang, S. Major, S. Vitta, S. S. Talwar, P. Dubcek, H. Amenitsch, S. Bernstorff, *Colloids Surf., A* **2002**, *198-200*, 67.
- [149] D. K. Lee, Y. S. Kang, C. S. Lee, P. Stroeve, *J. Phys. Chem. B* **2002**, *106*, 7267.
- [150] G. Tanami, V. Gutkin, D. Mandler, *Langmuir* **2010**, *26*, 4239.
- [151] K. L. Prime, G. M. Whitesides, *Science* **1991**, *252*, 1164.
- [152] S. Herrwerth, W. Eck, S. Reinhardt, M. Grunze, *J. Am. Chem. Soc.* **2003**, *125*, 9359.
- [153] C. Zhao, I. Witte, G. Wittstock, *Angew. Chem. Int. Ed.* **2006**, *118*, 5595.
- [154] G. Wulff, A. Sarhan, *Angew. Chem., Int. Ed. Engl.* **1972**, *11*, 341.
- [155] B. Sellergren, *J. Chromatogr. A* **2001**, *906*, 227.
- [156] R. Arshady, K. Mosbach, *Macromol. Chem. Phys.* **1981**, *182*, 687.
- [157] O. Norrloew, M. Glad, K. Mosbach, *J. Chromatogr.* **1984**, *299*, 29.
- [158] B. Sellergren, B. Ekberg, K. Mosbach, *J. Chromatogr.* **1985**, *347*, 1.
- [159] B. Sellergren, M. Lepistoe, K. Mosbach, *J. Am. Chem. Soc.* **1988**, *110*, 5853.
- [160] P. Curcio, C. Zandanel, A. Wagner, C. Mioskowski, R. Baati, *Macromol. Biosci.* **2009**, *9*, 596.
- [161] C. Alexander, H. S. Andersson, L. I. Andersson, R. J. Ansell, N. Kirsch, I. A. Nicholls, J. O'Mahony, M. J. Whitcombe, *J. Mol. Recognit.* **2006**, *19*, 106.

- [162] A. Poma, A. P. F. Turner, S. A. Piletsky, *Trends Biotechnol.* **2010**, 28, 629.
- [163] G. Vasapollo, R. Del Sole, L. Mergola, M. R. Lazzoi, A. Scardino, S. Scorrano, G. Mele, *Int. J. Mol. Sci.* **2011**, 12, 5908.
- [164] A. Flores, D. Cunliffe, M. J. Whitcombe, E. N. Vulfson, *J. Appl. Polym. Sci.* **2000**, 77, 1841.
- [165] P. Lenain, J. Diana Di Mavungu, P. Dubruel, J. Robbens, S. De Saeger, *Anal. Chem. (Washington, DC, U. S.)* **2012**, 84, 10411.
- [166] A. G. Mayes, K. Mosbach, *Anal. Chem.* **1996**, 68, 3769.
- [167] M. Mirzaei, S. A. H. Najafabadi, M. Abdouss, S. Azodi-Deilami, E. Asadi, M. R. M. Hosseini, M. Piramoon, *J. Appl. Polym. Sci.* **2013**, 128, 1557.
- [168] J. Mathew-Krotz, K. J. Shea, *J. Am. Chem. Soc.* **1996**, 118, 8154.
- [169] B. Jakoby, G. M. Ismail, M. P. Byfield, M. J. Vellekoop, *Sens. Actuators, A* **1999**, 76, 93.
- [170] I. A. Nicholls, J. P. Rosengren, *Bioseparation* **2002**, 10, 301.
- [171] G. Lautner, J. Kaev, J. Reut, A. Oepik, J. Rappich, V. Syritski, R. E. Gyurcsanyi, *Adv. Funct. Mater.* **2011**, 21, 591.
- [172] H. Shi, W.-B. Tsai, M. D. Garrison, S. Ferrari, B. D. Ratner, *Nature* **1999**, 398, 593.
- [173] M. Kempe, M. Glad, K. Mosbach, *J. Mol. Recognit.* **1995**, 8, 35.
- [174] N. M. Bergmann, N. A. Peppas, *Prog. Polym. Sci.* **2008**, 33, 271.
- [175] S. M. D'Souza, C. Alexander, S. W. Carr, A. M. Waller, M. J. Whitcombe, E. N. Vulfson, *Nature* **1999**, 398, 312.
- [176] E. Verheyen, J. P. Schillemans, M. van Wijk, M.-A. Demeniex, W. E. Hennink, C. F. van Nostrum, *Biomaterials* **2011**, 32, 3008.
- [177] G. Ceolin, Á. Orbán, V. Kocsis, R. Gyurcsányi, I. Kézsmárki, V. Horváth, *J. Mater. Sci.* **2013**, 48, 5209.
- [178] J. Bognar, J. Szucs, Z. Dorko, V. Horvath, R. E. Gyurcsanyi, *Adv. Funct. Mater.* **2013**, 23, 4703.
- [179] B. Liedberg, C. Nylander, I. Lundstroem, *Sens. Actuators* **1983**, 4, 299.
- [180] C. L. Haynes, R. P. Van Duyne, *J. Phys. Chem. B* **2001**, 105, 5599.
- [181] X. Zhang, A. V. Whitney, J. Zhao, E. M. Hicks, R. P. Van Duyne, *J. Nanosci. Nanotechnol.* **2006**, 6, 1920.
- [182] N. Bruchiel-Spanier, D. Mandler, in *ChemElectroChem*, **2015**.
- [183] M. Nullmeier, PhD thesis, Carl-von-Ossietzky-Universität, **2011**.
- [184] H. P. Boehm, *Carbon* **2002**, 40, 145.
- [185] M. Röefzaad, Diploma thesis, Carl von Ossietzky Universität, **2006**.
- [186] D. Roy, N. M. Das, P. S. Gupta, *Appl. Surf. Sci.* **2013**, 271, 394.
- [187] G. Oncins, J. Torrent-Burgues, F. Sanz, *J. Phys. Chem. C* **2008**, 112, 1967.
- [188] Z. Chen, Y. Zu, *Langmuir* **2007**, 23, 11387.
- [189] J. Kang, H. Li, S. K. Cushing, J. Wang, N. Wu, *ECS Trans.* **2009**, 19, 159.
- [190] S. Lee, J. Voeroes, *Langmuir* **2005**, 21, 11957.
- [191] H. S. Toh, C. Batchelor-McAuley, K. Tschulik, M. Uhlemann, A. Crossley, R. G. Compton, *Nanoscale* **2013**, 5, 4884.
- [192] S. Sitaula, M. R. Mackiewicz, S. M. Reed, *Chem. Commun.* **2008**, 3013.
- [193] O. Larsen, D. Postma, R. Jakobsen, *Geochim. Cosmochim. Acta* **2006**, 70, 4827.
- [194] S. Kraus-Ophir, J. Witt, G. Wittstock, D. Mandler, *Angew. Chem. Int. Ed.* **2014**, 53, 294.
- [195] J. Witt, D. Mandler, G. Wittstock, *ECS Trans.* **2015**, 66, 1.

- [196] M. Bosserdt, J. Erdossy, G. Lautner, J. Witt, K. Koehler, N. Gajovic-Eichelmann, A. Yarman, G. Wittstock, F. W. Scheller, R. E. Gyurcsanyi, *Biosens. Bioelectron.* **2015**, *73*, 123.
- [197] D. Dechtrirat, K. J. Jetzschmann, W. F. M. Stoecklein, F. W. Scheller, N. Gajovic-Eichelmann, *Adv. Funct. Mater.* **2012**, *22*, 5231.
- [198] L. E. Scriven, *Mater. Res. Soc. Symp. Proc.* **1988**, *121*, 717.
- [199] K. Norrman, A. Ghanbari-Siahkali, N. B. Larsen, *Annu. Rep. Prog. Chem. Sect. C: Phys. Chem.* **2005**, *101*, 174.
- [200] D. Meyerhofer, *J. Appl. Phys.* **1978**, *49*, 3993.
- [201] C. G. Sip, A. Folch, *Biomicrofluidics* **2014**, *8*, 036504/1.
- [202] J. Puigmarti-Luis, M. Rubio-Martinez, I. Imaz, B. Z. Cvetkovic, L. Abad, A. Perez del Pino, D. Maspoch, D. B. Amabilino, *ACS Nano* **2014**, *8*, 818.
- [203] M. Amberg, S. Stoebenau, S. Sinzinger, *Appl. Opt.* **2010**, *49*, 4326.
- [204] A. L. Thangawng, R. S. Ruoff, M. A. Swartz, M. R. Glucksberg, *Biomed. Microdev.* **2007**, *9*, 587.
- [205] A. E. Niotis, C. Mastichiadis, P. S. Petrou, A. Sifaka-Kapadai, I. Christofidis, K. Misiakos, S. E. Kakabakos, *Microelectron. Eng.* **2009**, *86*, 1491.
- [206] H. T. Zhang, N. N. Bao, D. Yuan, J. Ding, *Phys. Chem. Chem. Phys.* **2013**, *15*, 14689.
- [207] B. Weidenfeller, M. Hofer, F. Schilling, *Composites, Part A* **2002**, *33A*, 1041.
- [208] R. P. Tandon, M. R. Tripathy, A. K. Arora, S. Hotchandani, *Sensors and Actuators, B Chemical* **2006**, *114*, 768.
- [209] F. Walz, *Journal of Physics Condensed Matter* **2002**, *14*, R285.
- [210] E. J. W. Verwey, P. W. Haayman, *Physica (The Hague)* **1941**, *8*, 979.
- [211] S. Soeya, J. Hayakawa, H. Takahashi, K. Ito, C. Yamamoto, A. Kida, H. Asano, M. Matsui, *Appl. Phys. Lett.* **2002**, *80*, 823.
- [212] A. Verdager, S. Santos, G. Sauthier, J. J. Segura, M. Chiesa, J. Fraxedas, *Phys. Chem. Chem. Phys.* **2012**, *14*, 16080.
- [213] H.-J. Butt, J. Wang, R. Stark, M. Kappl, B. A. Wolf, J. Eckelt, A. Knopf, *Soft Mater.* **2007**, *5*, 49.
- [214] G. Sun, M. Kappl, T. Pakula, K. Kremer, H.-J. Butt, *Langmuir* **2004**, *20*, 8030.
- [215] S. Belaidi, P. Girard, G. Leveque, *J. Appl. Phys.* **1997**, *81*, 1023.
- [216] T. Echigo, D. M. Aruguete, M. Murayama, M. F. Hochella, Jr., *Geochim. Cosmochim. Acta* **2012**, *90*, 149.
- [217] L. L. Stookey, *Anal. Chem.* **1970**, *42*, 779.
- [218] T. B. To, D. K. Nordstrom, K. M. Cunningham, J. W. Ball, R. B. McCleskey, *Environ. Sci. Technol.* **1999**, *33*, 807.
- [219] G. Wittstock, B. Gründig, B. Strehnitz, K. Zimmer, *Electroanal.* **1998**, *10*, 526.
- [220] C. E. Banks, R. G. Compton, A. C. Fisher, I. E. Henley, *Phys. Chem. Chem. Phys.* **2004**, *6*, 3147.
- [221] M. Fleischer, C. Schmuck, *Chem. Commun. (Cambridge, U. K.)* **2014**, *50*, 10464.
- [222] K. Ryu, K. Kim, T.-i. Kim, *Macromolecular Research* **2014**, *22*, 264.
- [223] Y. Lu, L. Liu, W. Foo, S. Magdassi, D. Mandler, P. S. Lee, *Journal of Materials Chemistry C: Materials for Optical and Electronic Devices* **2013**, *1*, 3651.
- [224] M. M. Rhead, G. Eglinton, G. H. Draffan, P. J. England, *Nature* **1971**, *232*, 327.
- [225] S. C. Tsang, C. H. Yu, X. Gao, K. Tam, *J. Phys. Chem. B* **2006**, *110*, 16914.
- [226] J. Gao, H. Gu, B. Xu, *Acc. Chem. Res.* **2009**, *42*, 1097.

- [227] T. K. Jain, J. Richey, M. Strand, D. L. Leslie-Pelecky, C. A. Flask, V. Labhasetwar, *Biomaterials* **2008**, *29*, 4012.
- [228] L.-H. Chen, A. Dudek, Y.-L. Lee, C.-H. Chang, *Langmuir* **2007**, *23*, 3123.
- [229] Z. Matharu, A. J. Bandodkar, V. Gupta, B. D. Malhotra, *Chem. Soc. Rev.* **2012**, *41*, 1363.
- [230] H.-J. Tsai, Y.-L. Lee, *Soft Matter* **2009**, *5*, 2962.
- [231] T. H. Ha, D. K. Kim, M.-U. Choi, K. Kim, *J. Colloid Interface Sci.* **2000**, *226*, 98.
- [232] A. B. Moghaddam, T. Nazari, J. Badraghi, M. Kazemzad, *Int. J. Electrochem. Sci.* **2009**, *4*, 247.
- [233] R. N. Singh, B. Lal, M. Malviya, *Electrochim. Acta* **2004**, *49*, 4605.
- [234] J. Wouters, O. I. Lebedev, G. Van Tendeloo, H. Yamada, N. Sato, J. Vanacken, V. V. Moshchalkov, T. Verbiest, V. K. Valev, *J. Appl. Phys.* **2011**, *109*, 076105.
- [235] A. Chevreau, B. Phillips, B. G. Higgins, S. H. Risbud, *J. Mater. Chem.* **1996**, *6*, 1643.
- [236] F. Iskandar, M. Abdullah, H. Yoden, K. Okuyama, *J. Sol-Gel Sci. Technol.* **2004**, *29*, 41.
- [237] H. Ai, S. A. Jones, Y. M. Lvov, *Cell Biochemistry and Biophysics* **2003**, *39*, 23.
- [238] T. Cassagneau, T. E. Mallouk, J. H. Fendler, *J. Am. Chem. Soc.* **1998**, *120*, 7848.
- [239] D. V. Novikov, *Russ. J. Appl. Chem.* **2008**, *81*, 153.
- [240] D. K. Lee, Y. H. Kim, C. W. Kim, H. G. Cha, Y. S. Kang, *J. Phys. Chem. B* **2007**, *111*, 9288.
- [241] D. Li, X. Yu, Y. Dong, L. Zhang, Z. Li, Z. Zhao, *Appl. Surf. Sci.* **2010**, *256*, 4288.
- [242] M. Hesse, H. Meier, B. Zeeh, *Spektroskopische Methoden in der organischen Chemie*, Georg Thieme Verlag, Stuttgart, New York, **1991**.
- [243] Y.-G. Zhou, N. V. Rees, J. Pillay, R. Tshikhudo, S. Vilakazi, R. G. Compton, *Chem. Commun.* **2012**, *48*, 224.
- [244] S. Dongmo, J. Witt, G. Wittstock, *Electrochim. Acta* **2015**, *155*, 474.
- [245] S. Gilles, C. Kaulen, M. Pabst, U. Simon, A. Offenhaeusser, D. Mayer, *Nanotechnology* **2011**, *22*, 295301.
- [246] B. Ballarin, M. C. Cassani, E. Scavetta, D. Tonelli, *Electrochim. Acta* **2008**, *53*, 8034.
- [247] L. Guo, G. Chen, D.-H. Kim, *Anal. Chem.* **2010**, *82*, 5147.
- [248] T. Nakanishi, B. Ohtani, K. Shimazu, K. Uosaki, *Chem. Phys. Lett.* **1997**, *278*, 233.
- [249] Y. Wang, M. Lieberman, *Langmuir* **2003**, *19*, 1159.
- [250] O. P. Khatri, K. Murase, H. Sugimura, *Langmuir* **2008**, *24*, 3787.
- [251] C. Donley, D. Dunphy, D. Paine, C. Carter, K. Nebesny, P. Lee, D. Alloway, N. R. Armstrong, *Langmuir* **2002**, *18*, 450.
- [252] Y. Koide, M. W. Such, R. Basu, G. Evmenenko, J. Cui, P. Dutta, M. C. Hersam, T. J. Marks, *Langmuir* **2003**, *19*, 86.
- [253] C. O. Kim, S.-Y. Hong, M. Kim, S.-M. Park, J. W. Park, *J. Colloid Interface Sci.* **2004**, *277*, 499.
- [254] M. Chockalingam, N. Darwish, G. Le Saux, J. J. Gooding, *Langmuir* **2011**, *27*, 2545.
- [255] J. Zhang, Y. Liu, Y. Ke, H. Yan, *Nano Lett.* **2006**, *6*, 248.
- [256] M. Pourbaix, *Atlas of Electrochemical Equilibria in Aqueous Solutions*, Pergamon Press, Oxford, London, Edinburgh, New York, Toronto, Paris, Frankfurt, **1966**.
- [257] N. P. Finkelstein, R. D. Hancock, *Gold Bull.* **1974**, *7*, 72.

- [258] L. D. Burke, D. T. Buckley, J. A. Morrissey, *Analyst (Cambridge, U. K.)* **1994**, *119*, 841.
- [259] K. Juodkazis, J. Juodkazyte, V. Jasulaitiene, A. Lukinskas, B. Sebek, *Electrochem. Commun.* **2000**, *2*, 503.
- [260] L. Liu, S. Yellinek, I. Valding, A. Donval, D. Mandler, *Electrochim. Acta* **2015**, *176*, 1374.
- [261] E. Matveeva, *J. Electrochem. Soc.* **2005**, *152*, H138.
- [262] M. Senthilkumar, J. Mathiyarasu, J. Joseph, K. L. N. Phani, V. Yegnaraman, *Mater. Chem. Phys.* **2008**, *108*, 403.
- [263] J. D. Benck, B. A. Pinaud, Y. Gorlin, T. F. Jaramillo, *PLoS One* **2014**, *9*, e107942/1.
- [264] K. Tammeveski, K. Kontturi, R. J. Nichols, R. J. Potter, D. J. Schiffrin, *J. Electroanal. Chem.* **2001**, *515*, 101.
- [265] F. Mirkhalaf, K. Tammeveski, D. J. Schiffrin, *Phys. Chem. Chem. Phys.* **2004**, *6*, 1321.
- [266] B. Piro, S. Reisberg, G. Anquetin, H.-T. Duc, M.-C. Pham, *Biosensors* **2013**, *3*, 58.
- [267] F. Bruno, M. C. Pham, J. E. Dubois, *Electrochim. Acta* **1977**, *22*, 451.
- [268] M. Ferreira, H. Varela, R. M. Torresi, G. Tremiliosi-Filho, *Electrochim. Acta* **2006**, *52*, 434.
- [269] M. Gattrell, D. W. Kirk, *J. Electrochem. Soc.* **1993**, *140*, 903.
- [270] P. N. Bartlett, J. M. Cooper, *J. Electroanal. Chem.* **1993**, *362*, 1.
- [271] J. D. Craig, R. D. O'Neill, *Anal. Chim. Acta* **2003**, *495*, 33.
- [272] X. Chen, N. Matsumoto, Y. Hu, S. Wilson George, *Anal. Chem.* **2002**, *74*, 368.
- [273] R. J. Geise, J. M. Adams, N. J. Barone, A. M. Yacynych, *Biosens. Bioelectron.* **1991**, *6*, 151.
- [274] T. L. Panasyuk, V. M. Mirsky, S. A. Piletsky, O. S. Wolfbeis, *Anal. Chem.* **1999**, *71*, 4609.
- [275] C. A. Goss, J. C. Brumfield, E. A. Irene, R. W. Murray, *Langmuir* **1992**, *8*, 1459.
- [276] R. L. McCarley, E. A. Irene, R. W. Murray, *J. Phys. Chem.* **1991**, *95*, 2492.
- [277] R. L. McCarley, R. E. Thomas, E. A. Irene, R. W. Murray, *J. Electroanal. Chem. Interfacial Electrochem.* **1990**, *290*, 79.
- [278] H. O. Finklea, D. A. Snider, J. Fedyk, *Langmuir* **1990**, *6*, 371.
- [279] J. Wang, L.-H. Wu, R. Li, *J. Electroanal. Chem.* **1989**, *272*, 285.
- [280] L. Bao, R. Xiong, G. Wei, *Electrochim. Acta* **2010**, *55*, 4030.
- [281] W. Zhang, L. Bao, X. Zhang, J. He, G. Wei, *Water Environ. Res* **2012**, *84*, 2028.
- [282] G. Schneider, G. Decher, *Nano Lett.* **2004**, *4*, 1833.
- [283] P. Kekicheff, G. F. Schneider, G. Decher, *Langmuir* **2013**, *29*, 10713.
- [284] C. A. Rezende, L.-T. Lee, F. Galembeck, *Langmuir* **2009**, *25*, 9938.
- [285] H.-U. Krottil, T. Stifter, H. Waschipky, K. Weishaupt, S. Hild, O. Marti, *Surf. Interface Anal.* **1999**, *27*, 336.
- [286] T. Miyatani, S. Okamoto, A. Rosa, O. Marti, M. Fujihira, *Appl. Phys. A: Mater. Sci. Process.* **1998**, *A66*, S349.
- [287] O. Marti, M. Holzwarth, M. Beil, *Nanotechnology* **2008**, *19*, 384015.
- [288] J. Pinson, F. Podvorica, *Chem. Soc. Rev.* **2005**, *34*, 429.
- [289] D. S. Sebba, D. A. Watson, J. P. Nolan, *ACS Nano* **2009**, *3*, 1477.

10. Own publications and conference contributions

10.1 Publications

- [X1] F. Meiners, I. Plettenberg, J. Witt, B. Vaske, A. Lesch, I. Brand, G. Wittstock; "Local control of protein binding and cell adhesion by patterned organic thin films", *Anal. Bioanal. Chem.* **2013**, *405*, 3673.
- [X2] S. Kraus-Ophir, J. Witt, G. Wittstock, D. Mandler; "Nanoparticle-imprinted polymers for size-selective recognition of nanoparticles", *Angew. Chem. Int. Ed.* **2014**, *53*, 294.
S. Kraus-Ophir, J. Witt, G. Wittstock, D. Mandler; "Nanopartikelär geprägte Polymere für die gröÙenselektive Erkennung von Nanopartikeln", *Angew. Chem.* **2014**, *126*, 300.
- [X3] S. Dongmo, J. Witt and G. Wittstock; "Electropolymerization of quinone-polymers onto grafted quinone monolayers: A route towards non-passivating, catalytically active film", *Electrochim. Acta.* **2015**, *155*, 474.
- [X4] M. Bossert, J. Erdossy, G. Lautner, J. Witt, K. Köhler, N. Gajovic-Eichelmann, A. Yarman, G. Wittstock, F. W. Scheller, R. E. Gyurcsanyi, "Microelectrospotting as a new method for electrosynthesis of surface-imprinted polymer microarray for protein recognition", *Biosens. Bioelectron.* **2015**, *73*, 123.
- [X5] J. Witt, D. Mandler, G. Wittstock; "Magnetically controlled release of dispersed iron oxide nanoparticles from imprinted organic thin films", *ECS Trans.* **2015**, *66*, 1.

10.2 Oral presentations in national and international conferences

- [Y1] J. Witt, D. Mandler, G. Wittstock; "Nanoparticle (NP) imprinted matrices", From the witches cauldrons in material science, Goslar, Germany, 29 Apr - 1 May 2012. (in English)

- [Y2] J. Witt, D. Mandler, G. Wittstock; „Nanoparticles (NPs) imprinted matrices: Assembling interfaces with high selectivity towards functionalized NPs”, 8th Electrochemistry (EChemS), Bertinoro, Italy, 28 Jun - 01 Jul 2012. (in English)
- [Y3] J. Witt, D. Mandler, G. Wittstock; "Langmuir-Blodgett monolayers of iron oxide nanoparticles and oleic acid", Electrochemistry 2012, München, Germany, 17 - 19 Sep 2012. (in English)
- [Y4] J. Witt, D. Mandler, G. Wittstock; "Nanoparticle imprinted polymers (NIPs) used as sensing tools", Electrochemical Society (ECS), Chicago, USA, 24 - 28 May 2015. (in English)

10.3 Posters in national and international conferences

- [Z1] J. Witt, D. Mandler, G. Wittstock; "Langmuir-Blodgett monolayers of iron oxide nanoparticles and oleic acid", Bunsentagung 2012, Leipzig, 17 May - 19 May 2012.
- [Z2] J. Witt, D. Mandler, G. Wittstock; "Langmuir-Blodgett monolayers of iron oxide nanoparticles and oleic acid" , 63rd Annual Meeting of the International Society of Electrochemistry, Prague, Czech Republic, 26-29 Aug 2012.
- [Z3] J. Witt, D. Mandler, G. Wittstock; "Electrochemical manipulation of gold nanoparticles (AuNPs) embedded in thin polymer-based matrices", Electrochemistry 2014, Mainz, Germany, 22 - 24 Sep 2014.

11. Curriculum vitae

Personal data:

First and last name	Julia Witt
Date of birth	7.01.1984
Place of birth	Belye Vody in Kazakhstan
Nationality	German
Languages	German (mother tongue), English, Russian

Education:

04/2011 - 12/2015	PhD student at the Carl von Ossietzky University Oldenburg, Institute for Chemistry, Germany. Joint GIF-project with principal investigators Gunther Wittstock and Daniel Mandler (Jerusalem, Israel). "Nanoparticle Imprinted Matrices: Assembling Interfaces with High Selectivity towards Functionalized Nanoparticles" Graduate School "Science and Technology", PhD program
2011 - 2015	"Interface Science", University of Oldenburg, Germany
04/2009 - 04/2011	Carl von Ossietzky University Oldenburg, Master of Science, Master thesis "Electrochemical Deposition of Gallium for CIGS thin Film Solar-Cells" (translated title) in a joint project between the University and BOSCH Company in Stuttgart
10/2005 - 3/2009	Carl von Ossietzky University Oldenburg, Bachelor of Science, Bachelor thesis "Substantiation of the Chemistry of 8-(Amion-aryl-methylene)-1, 2, 3, 4, 5, 6, 7-heptathiocane (translated title)
1998 - 2005	Albertus-Magnus Gymnasium Friesoythe, Abitur
1992 – 1998	Primary and middle school in Friesoythe. I started with 8 years in the first class of primary school after relocation to Germany in 1992
1991-1992	Primary school in Belye Vody, Kazakhstan

Instruction and guidance of the following theses in the group of Prof. Wittstock

- 2015 MEd. thesis of Anne Staggenborg "Elektrochemische Abscheidung von Kompositen aus Metallnanopartikeln und Polymeren"
- 2013 MSc. thesis of Antje-Gabriele Wessel "Elektrochemische Abscheidung von organischen Funktionsmaterialien".
- 2013 BSc. thesis of Björn Janßen "Synthese funktionalisierter Nanopartikel"
- 2012 BSc. thesis of Claudia Kolb "Nanopartikelsynthesen für das Prägen von Matrizen"

Own participation in teaching

- 12/2011 - 2/2014 Instructor for "Cyclic Voltammetry" (basic electrochemical lab course for B.Sc. students)
- 2012 - 2013 Instructor for "Combination of Biocatalysts and Electrodes" (advanced lab course for M.Sc. students)
- 3 - 7/2010 Student assistant for the basic organic lab course (Prof. Dr. Doye)
- 4 - 5/2009 Student assistant for the basic organic lab course (Prof. Dr. Doye)

Offices in academic self-administration within the university

- 2011 - 2014 Appointment commission for the Division of Physical Chemistry as panel member representing scientific co-workers
- 2008 - 2011 Student member of M.Sc. admission committee of the Department of Chemistry
- 2008 - 2011 Student council

Grants

- 2015 Arbeitsgemeinschaft Elektrochemischer Forschungsinstitutionen e.V. (AGEF) and Gesellschaft Deutscher Chemiker e.V. (GDCh) travel grants to attend the 227th Meeting of the Electrochemical Society (ECS), Chicago, USA, 24 - 28 May 2015.
- 2014 Arbeitsgemeinschaft Elektrochemischer Forschungsinstitutionen e.V. (AGEF) travel grant to attend the conference Electrochemistry, Mainz, Germany, 22 - 24 September 2014.
- 2012 Gesellschaft Deutscher Chemiker e.V. (GDCh) travel grant to attend the 63rd Annual Meeting of the International Society of Electrochemistry, Prague, Czech Republik, 19 - 24 August 2012.
- 2012 Gesellschaft Deutscher Chemiker e.V. (GDCh) travel grant to attend the conference Electrochemistry, München, Germany, 17 - 19 Sep 2012.
- 2012 Travel grant from Graduate School "Science and Technology" to attend the 8th Meeting of Electrochemistry (ECHEMS), Bertinoro, Italy, 28 June - 1 July 2012.

Ich versichere hiermit, dass ich diese Arbeit selbständig verfasst und nur die angegebene Quellen und Hilfsmittel benutzt habe. Während der Dissertation sind die unter „Publications“ aufgelisteten Veröffentlichungen entstanden. Die Dissertation hat weder zu Teilen noch in Gänze einer anderen wissenschaftlichen Hochschule zur Begutachtung in einem Promotionsverfahren vorgelegen.

Oldenburg, den 10.12.2015

A handwritten signature in black ink, appearing to read 'Julia Witt', with a stylized flourish at the end.

Julia Witt